ISTANBUL TECHNICAL UNIVERSITY ★ GRADUATE SCHOOL

DEVELOPMENT OF N-HETEROCYCLIC CARBENE CATALYSTS FOR ATOM TRANSFER RADICAL POLYMERIZATION

Ph.D. Thesis

Mustafa Semih YILDIRIM

Department of Chemistry

Chemistry Programme

DECEMBER 2025

ISTANBUL TECHNICAL UNIVERSITY ★ GRADUATE SCHOOL

DEVELOPMENT OF N-HETEROCYCLIC CARBENE CATALYSTS FOR ATOM TRANSFER RADICAL POLYMERIZATION

Ph.D. Thesis

Mustafa Semih YILDIRIM
(509202207)

Department of Chemistry

Chemistry Programme

Thesis Advisor: Assoc. Prof. Cüneyt Hüseyin ÜNLÜ

DECEMBER 2025

İSTANBUL TEKNİK ÜNİVERSİTESİ ★ LİSANSÜSTÜ EĞİTİM ENSTİTÜSÜ

ATOM TRANSFER RADİKAL POLİMERİZASYONU İÇİN N-HETEROSİKLİK TABANLI KATALİZÖR GELİŞTİRİLMESİ

DOKTORA TEZİ

Mustafa Semih YILDIRIM
(509202207)

Kimya Anabilim Dalı

Kimya Programı

Tez Danışmanı: Doç. Dr. Cüneyt Hüseyin ÜNLÜ

ARALIK 2025

Mustafa Semih YILDIRIM, a Ph.D. student of ITU Graduate School student ID 509202207, successfully defended the thesis/dissertation entitled "DEVELOPMENT OF N-HETEROCYCLIC CARBENE CATALYSTS FOR ATOM TRANSFER RADICAL POLYMERIZATION", which he prepared after fulfilling the requirements specified in the associated legislations, before the jury whose signatures are below.

Thesis Advisor :	**Assoc. Prof. Cüneyt Hüseyin ÜNLÜ** İstanbul Technical University	.....
Jury Members:	**Prof. Dr. Abdullah AYDOĞAN** İstanbul Technical University	.....
	Prof. Dr. Dolunay ŞAKAR DAŞDAN Yildiz Technical University	.....
	Prof. Dr. Hakan DURMAZ İstanbul Technical University	.....
	Prof. Dr. Emrah ÇAKMAKÇI Marmara University	.....

Date of Submission : 6 November 2025
Date of Defense : 3 December 2025

To my family,

FOREWORD

The completion of this thesis marks the end of a significant chapter in my life, one spent between Istanbul Technical University and San Diego State University. It's a journey I could never have completed alone, and I want to thank the many people who stood by me.

My deepest professional gratitude goes to my thesis advisor, Assoc. Professor Cüneyt Hüseyin ÜNLÜ. Your unwavering belief in this project and your guidance kept me on track even when the results were slow to come.

I am also filled with remembrance for the late Professor Douglas B. GROTJAHN. His mastery of synthetic and organometallic chemistry was incredible, and I will always cherish the time he spent schooling me in his lab. His passing was a devastating blow, and I deeply miss his energetic discussions in the lab.

I thank my thesis jury members, Professor Prof. Dr. Abdullah AYDOĞAN and Prof. Dr. Dolunay ŞAKAR DAŞDAN, for their excellent advice, which truly pushed this work to a higher level.

My days in the lab were brightened by my colleagues. Hüseyin Cem KILIÇLAR and Emirhan GENÇOSMAN were my rock—thank you for the collaboration and the morale boosts, especially for the long nights we spent optimizing the experiments.

Professor Jing GU deserves special thanks for her incredible support and kindness during my time at San Diego State University. She is a truly great personality.

I also cannot thank Dr. Gregory I. ELLIOTT enough; his expertise in mass analysis and our insightful discussions were pivotal for the synthetic part of this study.

I am also grateful to my friends and colleagues, Yusuf ALÇAY, Özgür YAVUZ, Emre ÖZDEMIR, Hülya ARIBUĞA, and Utku ERTUĞRAL with whom I have had the privilege of sharing my academic journey. Growing alongside them through these formative years has been a source of great camaraderie and strength.

On a personal note, my family is my foundation. To my wife, Cennet YILDIRIM: you endured the long hours and my stress with endless grace and love. This thesis is as much yours as it is mine.

To my parents, Mehmet YILDIRIM and Zehra YILDIRIM: thank you for a lifetime of sacrifice and for teaching me the value of hard work.

And to my brothers, Ahmet Zahid YILDIRIM, Muhammed Esad YILDIRIM and Halil Bayram YILDIRIM, and my sister, Makbule Beyza AVCAN—thank you for always being there with constant support and motivation.

Finally, I accept full responsibility for any shortcomings in this manuscript and hope that its findings will contribute meaningfully to the scientific community.

Aralık 2025

Mustafa Semih YILDIRIM
(MSc.Chemist)

TABLE OF CONTENTS

Page

ABBREVIATIONS

DCM	**:** Dichloromethane
PS	**:** Polystyrene
NHC	**:** N-heterocyclic carbene
ATRP	**:** Atom Transfer Radical Polymerization
MMA	**:** Methyl Methacrylate
NMR	**:** Nuclear Magnetic Resonance
PMMA	**:** Poly(Methyl Methacrylate)
THF	**:** Tetrahydrofuran
UV	**:** Ultraviolet
DFT	**:** Density Functional Theory
DMF	**:** Dimethyl Formamide
EtOH	**:** Ethanol
FTIR	**:** Fourier Fourier transform infrared spectroscopy
HRMS	**:** High resolution mass spectrometry
IUPAC	**:** International Union of Pure and Applied Chemistry
ICAR	**:** Initiators for continuous activator regeneration
GPC	: Gel permeation chromatography
CLRP	: controlled/living radical polymerization
TEP	: Tolman's electronic parameter
CAAC	**:** Cyclic Alkyl Amino Carbenes
AIBN	**:** Azobisisobutyronitrile

SYMBOLS

$Đ$	: Dispersity
M_w	: Weight Average Molecular Weight
M_n	: Number Average Molecular Weight
t	: Time
M	: Molarite
µ	: micro
m	: mili
n	: nano
L	: Liter
g	: gram

LIST OF TABLES

Sayfa

LIST OF FIGURES

Sayfa

DEVELOPMENT OF N-HETEROCYCLIC CARBENE CATALYSTS FOR ATOM TRANSFER RADICAL POLYMERIZATION

SUMMARY

Carbene chemistry is one of the most active topics in modern coordination and organometallic research. Carbenes are known for their distinctive bonding behavior. These bonds help stabilize metals in several oxidation states. N-heterocyclic carbenes (NHCs) is a significant class of ligand family of the carbene chemistry. They behave as strong σ-donors and moderate π-acceptors. This combination allows precise and tunable control over the electronic structure of metal centers. The progress in NHC-based catalysis has shaped many areas, from organic synthesis to polymer science. It has been especially influential in the design of catalysts for Atom Transfer Radical Polymerization (ATRP).

ATRP is a controlled/living radical polymerization method that is used to ensure the preparing of polymers not only with foreseeable molecular weights but also low/uniform molecular weight distributions. Its variant, Initiators for Continuous Activator Regeneration ATRP (ICAR-ATRP), utilizes reducing agents such as AIBN to consistently reproduce activator species, enabling polymerizations with very low amount of catalyst concentrations. While most ATRP systems rely on copper complexes, recent attention has turned to iron-based catalysts, which are more sustainable, less toxic, and environmentally benign. However, understanding how the ligand's electronic properties influence the Fe(II)/Fe(III) redox cycle and the polymerization control remains limited.

In this study, a new family of Fe–NHC catalysts was designed and synthesized to reveal the link between the modulated electronic structure of the carbene ligand and the catalytic activity in ICAR-ATRP. Four para-substituted NHC ligands as having methoxy (–OMe), iodine (–I), cyano (–CN), and hydrogen (–H) functional groups were synthesized and coordinated to $FeBr_3$ to form FeNHC-OMe, FeNHC-I, FeNHC-CN, and FeNHC-H complexes. The design rationale was to tune the electronic enviroment around the iron catalytic center by systematically altering the donor or withdrawing characteristics of the NHC backbone.

NMR analysis was performed on the free NHC ligands in inert atmosphere to evaluate the substituent effect by measuring the carbene carbon chemical shift. The ^{13}C NMR spectra displayed carbene-carbon peaks between 220 and 225 ppm, confirming strong σ-donation. The most downfield signal at 223.8 ppm appeared for NHC-OMe, showing its stronger electron-donating character. Electrochemical results indicated quasi-reversible Fe(II)/Fe(III) redox behavior for all complexes. The FeNHC-OMe catalyst showed the most positive anodic potential (E_pa). This means it formed a more oxidizing Fe(III) species that maintained a stable activation–deactivation balance during polymerization. DFT calculations supported the same conclusion. The methoxy-substituted complex had the most stable configuration (–93.8 kcal mol^{-1}). It also showed a slightly wider N–C–N bond angle as consistent with stronger resonance stabilization.

Polymerization trials were performed with polar methyl methacrylate (MMA) monomer and styrene monomer during the catalytic experiments. The results showed that Fe–NHC catalysts controlled the radical polymerization process efficiently. The dispersity (Đ) of the obtained polymers decreased from 1.70 to 1.33 for PMMA and from 1.61 to 1.20 for PS, confirming improved control in ICAR-ATRP. Increasing catalyst concentration further reduced dispersity below 1.14 for styrene. Kinetic studies performed with Fe-NHC-OMe revealed linear Mn growth with time and stable Đ ≈ 1.15, while minor deviations from theoretical Mn values were attributed to oxygen-induced chain transfer during in-situ sampling.

Chain-end fidelity and block-copolymer formation were verified through ^{1}H NMR and photochemical chain-extension experiments. Bromine-terminated chain ends were displayed by ^{1}H-NMR spectroscopic experiments with a peak resonated at 4.5 ppm, and block extension with MMA under 400 nm irradiation using $Mn_2(CO)_{10}$ produced PS-b-PMMA copolymers. GPC and FTIR results verified the formation of the new block structure and a molecular-weight increase of approximately 130 %.

This study shows that Fe-NHC catalysts, especially Fe-NHC-OMe, allow efficient and well-controlled ICAR-ATRP even at low catalyst levels. The combination of carbene-ligand design, electrochemical testing, and computational modeling reveals a clear relationship between ligand electronics and catalytic behavior. The findings indicate that Fe–NHC systems offer a sustainable and non-toxic alternative to traditional copper-based ATRP catalysts. They also expand the understanding of how carbene chemistry can drive progress in controlled radical polymerization technology.

ATOM TRANSFER RADİKAL POLİMERİZASYONU İÇİN N-HETEROSİKLİK TABANLI KATALİZÖR GELİŞTİRİLMESİ

ÖZET

Karben kimyası, organometalik ve koordinasyon kimyasının tarihinde özel bir kırılma noktası oluşturan ve kimyasal düşüncenin evrimini etkileyen alanlardan biridir. Karbenlerin, yani divalent karbon merkezine sahip nötr türlerin varlığı ve kararlılığı, 20. yüzyılın ortalarına kadar tartışmalı bir konu olarak kalmış; yüksek reaktiviteleri nedeniyle uzun yıllar boyunca yalnızca geçici ara ürünler olarak kabul edilmiştir. Ancak karbenlerin elektron çiftlerinin dizilimine bağlı olarak singlet ve triplet olmak üzere iki temel elektronik duruma sahip olabileceğinin anlaşılması ve bu türlerin spektroskopik yöntemlerle doğrulanması, modern karben kimyasının temellerini atmıştır.

Karbenler, altı değerlik elektronu içeren ve dolayısıyla elektronca eksik, yüksek enerjili kimyasal türlerdir. Elektronik durumlarına göre singlet ve triplet olarak sınıflandırılırlar. Singlet karbenlerde iki elektron aynı orbitalde eşleşmiş halde bulunur ve karbon üzerinde boş bir p orbitali bulunur. Bu boş orbital onların temel olarak elektrofilik davranmasına neden olur. Ancak heteroatomlarla stabilize edilmiş belirli singlet karbenler örneğin N-heterosiklik karbenler (NHC'ler) rezonans ve σ-donör kabiliyetleri nedeniyle belirgin nükleofilik özellik de gösterebilir; bu durum singlet karbenlerin genel davranışının bir istisnası olarak kabul edilir. Triplet karbenlerde ise iki elektron farklı orbitallerde eşleşmemiş halde bulunduğundan bu sinif paramanyetiktir ve reaktivite radikal karakterlidir. Karbenlerin singlet–triplet ayrımı, reaksiyon mekanizmalarının yönünü, geçiş durumlarının enerjisini ve ürün seçiciliğini belirlediğinden sentetik ve organometalik kimyada kritik önem taşır. Özellikle NHC'ler gibi kararlı singlet karbenler, güçlü σ-donör özellikleri sayesinde metal merkezlerini stabilize eder ve günümüz katalizlerinde temel ligand sınıflarından biri haline gelmiştir.

Bu tarihsel gelişim içinde N-heterosiklik karbenler (NHC'ler) kimya dünyasında devrim niteliğinde bir adım olarak kabul edilmiştir. Arduengo'nun 1991 yılında oda sıcaklığında izole edilebilir, kararlı imidazol-2-iliden karbenini raporlaması, karben kimyasını teorik bir alandan çıkarıp organometalik kimyanın en güçlü ligand sınıflarından birine dönüştürmüştür. NHC'lerin kararlılığı, aromatik halkadaki rezonans etkisi ve hetero atomlarının elektronik dengesinden kaynaklanmaktadır. Bu nedenle NHC ligandları, klasik fosfin ligandlarına kıyasla oksijen ve neme karşı çok daha dirençli, daha yüksek termal stabiliteye sahip ve elektronik olarak daha güçlü σ-donor özellik gösteren bir alternatif sağlamaktadır.

NHC'lerin yapı çeşitliliği oldukça geniştir: imidazol, benzimidazol, triazol, thiazol türevleri; imidazolin, imidazolidin türevleri; backbone-substitue edilmiş, yüklü/yüksüz NHC türleri; abnormal karbenler (aNHC); mesoiyonik karbenler; ve bicyclic NHC sistemleri bunlardan bazılarıdır. Her bir yapısal varyasyon, ligandın donor/akseptör özelliklerini, sterik koruyuculuğunu ve metal-ligand bağının doğasını farklılaştırarak uygulama alanlarını genişletmektedir.

Bugün NHC'ler yalnızca metal kompleksleriyle sınırlı değildir. Serbest NHC'ler organokataliz alanında benzoin kondensasyonu, Stetter reaksiyonları, transesterifikasyon gibi çok sayıda dönüşümde aktif şekilde yer almaktadır. Metal-NHC kompleksleri ise katalizör olarak; olefin metatezi, C–C bağ oluşumları, hidrojenasyon ve dehidrojenasyon süreçleri, CO_2'nin kimyasal aktivasyonu, ilaç sentezinde mediyatör katalizörler, yüzey modifikasyonu, nanomalzeme stabilizasyonu, MOF/COF tasarımı ve polimer kimyasında kontrollü radikal polimerizasyon gibi oldukça geniş bir kullanım alanına sahiptir. Özellikle katalizde NHC'lerin güçlü σ-donör karakteri, metal merkezini elektronca zenginleştirerek katalitik çevrimin hızını ve seçiciliğini iyileştirmektedir.

Polimer kimyası tarafında ise kontrollü/living radikal polimerizasyon yöntemlerinin gelişmesi, NHC'li metal komplekslerinin önemini daha da artırmıştır. Atom Transfer Radikal Polimerizasyonu (ATRP), Matyjaszewski tarafından geliştirilmiş olup kontrollü radikal polimerizasyon yöntemleri içerisinde en esnek, en geniş monomer uyumluluğuna sahip tekniklerden biridir. ATRP'de metal kompleksleri zincir büyümesini kontrol eden temel unsurdur; aktivasyon/deaktivasyon döngüsünü yöneterek radikal yoğunluğunu çok düşük seviyelerde tutar ve böylece polimer zincirlerinin eşzamanlı büyümesini sağlar.

ATRP'nin çevresel kaygılar nedeniyle daha düşük metal içerikli versiyonlarının geliştirilmesi, bu yöntemin endüstriyel uygulanabilirliğini önemli ölçüde artırmıştır. ICAR-ATRP, aktivatörün sürekli yenilendiği ve çok düşük metal konsantrasyonlarının yeterli olduğu bu yöntemlerden biridir. ICAR-ATRP'nin çalışma mantığı, başlatıcının yüksek bir konsantrasyonda, aktivatörün ise düşük ve sürekli yenilenen bir konsantrasyonda tutulmasına dayanır. Bu mekanizma hem yüksek reaktör hacimlerine uyum sağlar hem de metal kontaminasyonunu minimize eder.

Geleneksel ATRP sistemlerinde kullanılan bakır temelli komplekslerin yerine demirin önerilmesi ise çevre dostu kataliz fikrinin giderek güçlendiğinin göstergesidir. Demir, biyolojik sistemlerle uyumluluğu, düşük toksisitesi, geniş redoks penceresi ve bol bulunabilirliği ile sürdürülebilir kimya açısından ideal bir metal olarak öne çıkmaktadır. Ancak Fe(II)/Fe(III) redoks dengesinin ligand elektronik özelliklerinden çok güçlü şekilde etkilendiği bilinmesine rağmen literatürde Fe–NHC kompleksleri üzerine yapılmış sistematik çalışmalar sınırlıdır.

Bu tez çalışmasında, elektronik özellikleri sistematik olarak değiştirilmiş dört yeni NHC ligandı sentezlenmiş ve bunların $FeBr_3$ ile kompleksleşmesi sonucunda dört yeni Fe–NHC katalizörü elde edilmiştir (FeNHC-OMe, FeNHC-I, FeNHC-CN ve FeNHC-H). Para konumundaki sübstitüentler, ligandın π-sistemiyle rezonans yapabilen ya da indüktif etkilerle elektron yoğunluğunu değiştirebilen gruplar olarak seçilmiştir. Bu tasarım yaklaşımıyla, NHC ligandlarının elektron yoğunluğu değiştirilerek demir merkezinin katalitik aktivitesi ve redoks kararlılığı sistematik biçimde değerlendirilmiştir.

Sentezlenen ligandların ^{13}C NMR spektrumlarında 220–225 ppm civarında karben-karbon sinyali tespit edilmiş ve bu sinyaller ligandla metal arasındaki bağın güçlü σ-donor karakterini doğrulamıştır. En büyük aşağı kayma NHC-OMe ligandında gözlenmiş ve bu bulgu metoksi grubunun mezomerik etkisiyle elektron yoğunluğunu ligand merkezine doğru ittiğini göstermiştir.

Elektrokimyasal analizler, tüm komplekslerin yarı-tersinir redoks davranışı sergilediğini, fakat Fe-NHC-OMe'nin en pozitif Epa değerine sahip olduğunu göstermiştir. Bu durum aktivasyon-deaktivasyon dengesinde daha güçlü bir deaktivasyon türünün varlığına işaret eder ki bu, kontrollü polimerizasyon için oldukça kritik bir parametredir.

Teorik DFT hesaplamaları, metoksi substitüentinin rezonans delokalizasyonuyla kompleksin toplam enerjisini belirgin şekilde düşürdüğünü ve kararlılığı artırdığını göstermiştir. Enerjinin -93.8 kcal.mol^{-1} değerine ulaşması, OMe-substitüe kompleksin diğerlerine kıyasla daha kararlı bir elektron dağılımına sahip olduğunu desteklemiştir.

Polimerizasyon deneylerinde MMA ve stiren monomerleri kullanılmış ve ICAR-ATRP koşullarında Fe–NHC komplekslerinin zincir büyümesini etkin şekilde kontrol edebildiği gözlenmiştir. PMMA'da dispersite (Đ) 1.70'ten 1.33'e inerken, stirende 1.61'den 1.20'ye düşmüştür. Özellikle Fe-NHC-OMe ile yapılan polimerizasyonlar düşük dispersite, doğrusal Mn artışı ve zincir uçlarının korunması açısından en başarılı sonuçları vermiştir.
Zincir uç fonksiyonelliği ^{1}H-NMR ile doğrulanmış, 4.5 ppm civarındaki brom uç sinyali polimer zincirlerinin kontrollü şekilde büyüdüğünü ortaya koymuştur. Ayrıca $Mn_2(CO)_{10}$ katalizinde 400 nm ışık altında MMA ile yapılan zincir uzatma deneylerinde PS-b-PMMA blok kopolimerleri başarıyla elde edilmiş; GPC ve gravimetrik analizlerde yaklaşık %130'luk molekül ağırlığı artışı tespit edilmiştir.
Tüm bu sonuçlar değerlendirildiğinde, Fe-NHC-OMe katalizörü hem teorik hem deneysel açıdan ICAR-ATRP için en uygun yapıyı sunmuştur. Güçlü elektron vericiliği, redoks döngüsünü optimum denge noktasında tutmuş; polimer zincirlerinin kontrollü büyümesine, düşük dispersite değerlerinin elde edilmesine ve zincir uçlarının korunmasına olanak tanımıştır.
Bu çalışma, karben kimyasının polimer bilimindeki yeni uygulama alanlarına nasıl yön verdiğini göstermesi açısından önemlidir. Ayrıca sürdürülebilir ve toksisitesi düşük demir katalizörlerinin geliştirilmesine yönelik ileriki çalışmalara güçlü bir zemin hazırlamaktadır. NHC ligand tasarımının metal merkezinin elektronik özellikleri ve katalitik performansı üzerindeki etkisi bu tezde sistematik olarak ortaya konmuş; kontrollü radikal polimerizasyon süreçlerinde ligand mühendisliğinin ne denli kritik olduğu açıkça gösterilmiştir.

1. INTRODUCTION

The field of polymer chemistry has revolutionized thanks to developing controlled/living radical polymerization (CRP) by allowing the fabrication of polymeric materials with foreseeable molecular weights, uniform dispersities, and complex molecular engineering. Among the CRP techniques, Atom Transfer Radical Polymerization stands out thanks to its versatility, tolerance to different type of functional groups, and wide range of monomers. Since its introduction by Sawamoto and Matyjaszewski during the mid-1990s, ATRP has occured such a powerful method for creating advanced polymeric materials with specific, tunable properties.

Conventional ATRP usually relies on copper-based catalysts to reversibly activate and deactivate growing radical chains. Copper complexes offer strong catalytic activity. However, issues such as toxicity, cost, and the need for purification have motivated research toward more sustainable and biocompatible systems. In this regard, iron catalysts have drawn significant attention. Iron is abundant, less toxic, and environmentally benign. Early studies showed that Fe(II)/Fe(III) redox pairs can mediate radical polymerization effectively. Still, achieving high activity and precise control at low catalyst levels remains a major challenge especially for polar monomers.

Ligand design is key to adjusting the electronic behavior and stability of metal centers in ATRP catalysts. N-heterocyclic carbenes (NHCs) exhibit highly effective catalytic performance as a ligand because they donate its electrons strongly through σ-bonds, offer adjustable steric environments, and remain stable under heat and chemical stress. These traits allow NHCs to tune the redox potential of the bound metal and stabilize reactive intermediates during polymerization. Although Cu–NHC systems have been widely studied, research on Fe–NHC catalysts is still limited. Understanding how electronic groups on the NHC ring affect the redox chemistry and catalytic power of iron is essential for developing efficient and sustainable ATRP systems.

This work fills that gap by designing and synthesizing a series of Fe–NHC complexes with electron-donating and electron-withdrawing groups at the four-position of the aniline precursor. The substituents (–OMe, –I, –CN, –H) were studied systematically to assess their influence on the electronic environment of the iron catalytic center and also on polymerization performance. To define the link between structure and activity, ^{13}C NMR spectroscopy, cyclic voltammetry experiment as an electrochemical analysis, and computatioanl study by density functional theory (DFT) were applied. Polymerization behavior was evaluated in the ICAR-ATRP of polar methyl methacrylate monomer and styrene. Attention was given to molecular-weight control, dispersity, kinetic trends, and chain-end fidelity to identify this structure-activity relationship. The results show how tuning the electronics of NHC ligands governs redox balance and radical propagation in Fe-mediated ATRP. By establishing a clear relationship between ligand structure and catalytic efficiency, this study supports the rational design of next-generation.

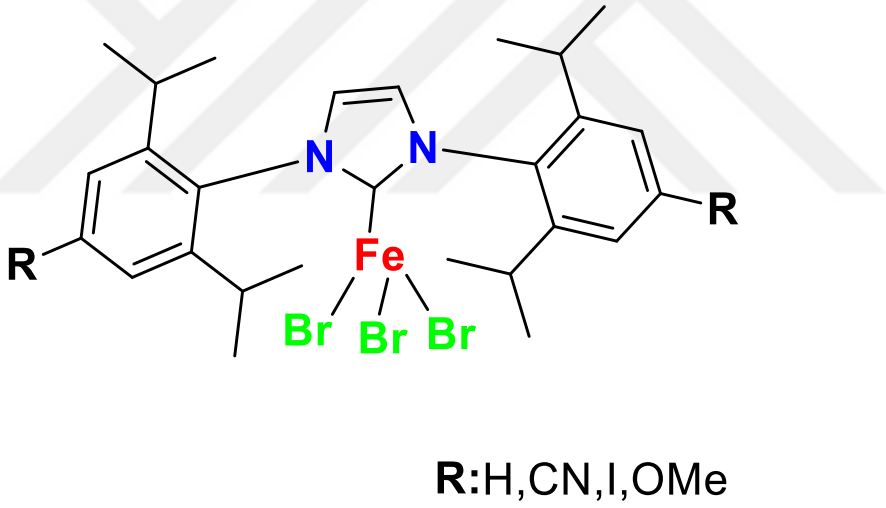

Figure 1.1 : Synthesized Iron NHC complexes by varying different substituent.

Chapter 2 provides a detailed review of the literature on ATRP, ICAR mechanisms, and the chemistry of NHC ligands. Chapter 3 explains the experimental methods, covering ligand synthesis, complex preparation, and characterization steps. Chapter 4 presents the results from spectroscopic, electrochemical, and computational analyses, along with polymerization and kinetic studies. Finally, Chapter 5 summarizes the main findings and evaluates the catalytic systems developed in this work. It also highlights their potential for future research and industrial use.

2. GENERAL OVERVIEW

2.1 Carbenes

Carbenes are neutral, divalent carbon species in which the carbon atom forms two σ-bonds and holds two non-bonding electrons by giving a formal oxidation state of zero. Depending on how these electrons are coupled, carbenes appear in singlet (paired) or triplet (unpaired) forms. This distinction was first clarified through studies in the mid-twentieth century[1]. The singlet–triplet difference defines their main reactivity. Singlet carbenes often insert into σ-bonds or add to π-systems, while triplet carbenes act like diradicals. They are unique among carbon compounds because they possess only six valence electrons. That electron deficiency gives them both electrophilic and nucleophilic character. From their first theoretical proposal in the nineteenth century to the later isolation of stable, bottleable forms, carbenes have become essential to organometallic and catalytic chemistry[2, 3].

By the early twentieth century, carbene chemistry was founded on studies of diazo compound decomposition. Photolysis or thermolysis of diazo precursors was found to generate reactive intermediates that could form cyclopropane groups on the studied molecule. These discoveries confirmed that carbenes were real even if they are short-lived, chemical species. For the next fifty years, however, they were never directly isolated. Their presence was recognized only through the products they formed[4, 5].

Mid-twentieth century progress in quantum chemistry reshaped how carbenes were understood. Hine's Divalent Carbon gave the first systematic definition of a carbene. It described a compound with a neutral, two-coordinate carbon bearing six valence electrons, two of which occupy nonbonding orbitals. Later ab initio calculations on methylene predicted an angular geometry (bent) and also revealing its triplet ground state. This view contradicted earlier linear models proposed from spectroscopic evidence[6].

During the 1960s and 1970s, chemists viewed carbenes as intrinsically unstable. Even Wanzlick's 1960 proposal of a cyclic imidazolidin-2-ylidene was treated as speculation because his synthesis produced only a dimeric enetetramine[3, 7]. This

view began to change later by a study published in the late 1980s by Bertrand and colleagues exhibited a (phosphino)(silyl)carbene that could be isolated as a red oil. Their result showed that heteroatom substitution can provide both electronic and kinetic stabilization[8]. Three years later, Arduengo and colleagues reached a major milestone. They crystallized 1,3-bis(adamantyl)imidazolylidene as the first stable, free carbene ever obtained. This compound became the prototype for N-heterocyclic carbenes (NHCs). It combined strong σ-donor ability with steric protection from bulky substituents[9].

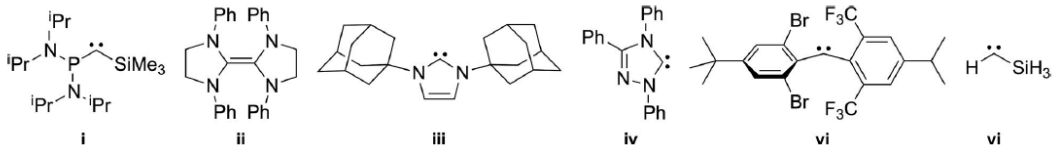

Figure 2.1 : Different type of carbene compounds by heteroatom and sterically stabilized from.

The discovery transformed coordination and organometallic chemistry due to the NHC`s superior ligand ability. NHCs quickly became strong ligands for transition-metal complexes. They rival phosphines in σ-donor strength and often exceed them in stability under catalytic conditions[10]. The electronic structure of these singlet carbenes was later clarified by solid-state ^{13}C NMR analysis of the carbene carbon. This produced the first crystal-state measurement of its resonance. An anisotropy of about 240 ppm, among the largest known for carbon in an organic lattice, showed the deshielded nature of the empty p orbital perpendicular to the molecular plane[11].

NHCs represent stabilized singlet carbenes, yet the search for long-lived triplet analogues continues. Hirai, Itoh, and Tomioka reviewed decades of efforts to create such species through bulky aryl substitution, π-delocalization, and confinement in solid matrices. Their electron spin resonance (ESR) studies linked zero-field splitting parameters to structural factors such as bond angle and spin delocalization. They identified di(9-anthryl) carbene as one of the most delocalized triplet systems known[12].

By the early twenty-first century, experimental and theoretical carbene chemistry had become a predictive field. Density functional and coupled-cluster methods made it possible to calculate singlet–triplet gaps (ΔE_S–T) with quantitative accuracy. These tools also enabled the design of carbenes with targeted reactivity. Computational results showed that heteroatom (N,O,P, and S) π-donation and steric restriction

stabilize singlet carbenes. In contrast, substitution with electropositive atoms such as silicon or boron reduces π-conjugation and favors triplet character[6].

Today, carbenes are viewed not as fleeting species but as a versatile family of ligands, catalysts, and intermediates at the core of organometallic, polymerization, and materials chemistry. Their development—from Dumas's elusive methylene to Arduengo's stable imidazolylidene—reflects the broader evolution of carbon chemistry itself. It marks the shift from empirical observation to the deliberate design of electronic structure[2, 13–15].

2.2 N-heterocyclic Carbenes

N-heterocyclic carbene ligands are such a significant division of compounds in modern coordination chemistry and organometallic fields by shaping the way of the catalyst design and application not only as homogeneous catalyst but also supported heterogeneous catalyst. They are neutral divalent carbon species that have a lone pair of electrons having a strong sigma bond forming ability on the carbene carbon. The carbene carbon is stabilized by two adjacent nitrogen atoms embedded in a heterocyclic ring. In contrast to classical carbenes that typically possess a triplet ground state, NHCs feature a singlet ground state. Their lone pair resides in an sp^2 orbital within the plane of the ring, whereas an empty p orbital extends perpendicular to that plane. The ring structure enforces a rigid geometry and widens the singlet–triplet energy gap. At the same time, the neighboring nitrogen atoms donate electron density through inductive and resonance effects, stabilizing the singlet form[15–17].

N-heterocyclic carbene (NHC) ligands can be now considered as valuable tools in catalysis. They provide several advantages over conventional ligands such as phosphines, phosphide etc. Each NHC ligand contains a carbon atom bound to a nitrogen-containing heterocycle. Electron delocalization within this ring gives the ligand strong stability. That stability supports efficient and selective catalytic transformations. NHC ligands are highly adaptable and can be modified for different catalytic purposes. Changes in the backbone, substituents, or coordinating sites allow precise tuning of their properties. This versatility has broadened the reach of NHC-based catalysis across many areas of chemistry.

Historically, the idea of NHC coordination appeared before the isolation of free carbenes. Wanzlick and Schönherr, and independently Öfele, reported the first carbene

complexes with mercury(II) and chromium(0), respectively in the year of 1968. It was not until 1991 that Arduengo and colleagues isolated and structurally confirmed a stable free NHC—the imidazol-2-ylidene compound known as IAd. This achievement marked a turning point in ligand design. It showed that NHCs could serve as adjustable ligands comparable to, and often stronger than, phosphines[18].

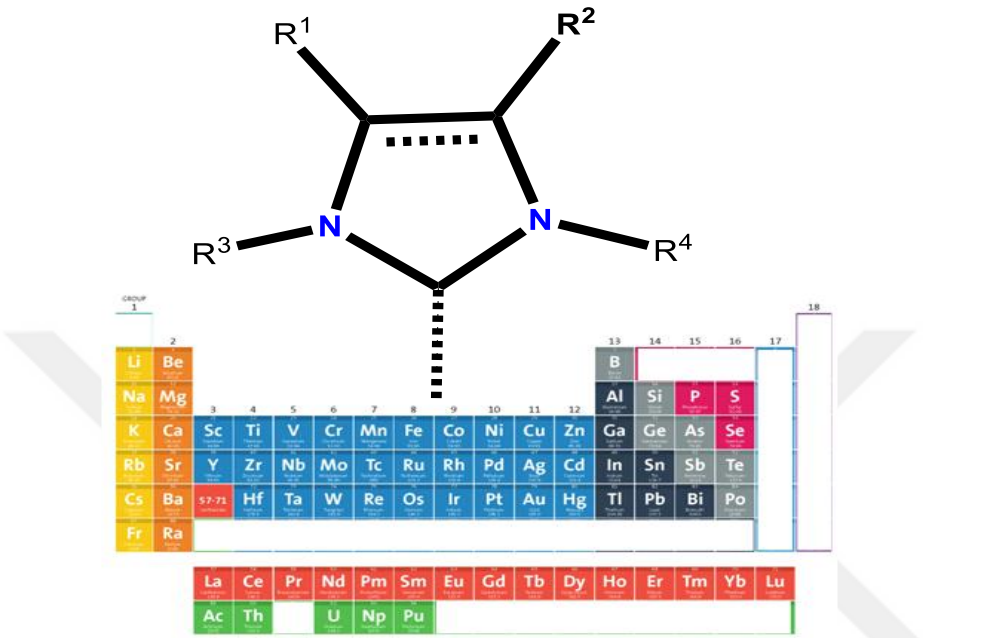

Figure 2.2 : NHC and its coordination ability.

The bonding nature of NHCs is defined by evaluating their strong sigma donation and weak π-acceptor character. This feature is evident in spectroscopic data such as the carbonyl stretching frequencies of prepared nickel complexes as can be depicted $LNi(CO)_3$. In these systems, CO bands appear at lower wavenumbers than in analogous phosphine complexes, indicating stronger σ donation[19]. The σ-donor ability of NHCs strengthens the metal–carbon bond. As a result, the complexes show a strong trans influence and remain stable under heat or oxidative conditions. Electronic contributions are often measured using Tolman's electronic parameter (TEP). On the other hand, steric effects are evaluated using the buried-volume parameter. When combined, these descriptors provide a comprehensive measure of the ligand's electronic donating ability and its steric bulk[20, 21].

Due to their electronic and steric features, NHCs are now common throughout coordination chemistry. They are able to make coordination compounds with most of the transition metal in the periodic table. They also coordinate with main-group and even f-block elements[16, 22]. Their capacity to stabilize both low- and high-valent

metals has opened new paths in catalysis field and small-molecule activation strategies. Compared with phosphine-based systems, complexes of Pd(II) and Ni(II) containing NHC ligands possess markedly greater stability and undergo oxidative addition at a much faster rate[15]. Likewise, Ru(II)–NHC complexes serve as the core of the second-generation Grubbs and Hoveyda–Grubbs olefin-metathesis catalysts, which have become essential tools in modern synthetic chemistry[16].

Beyond transition-metal systems, NHCs bond effectively with main-group elements for example boron, aluminum, silicon, tin, and bismuth, as well as with actinides. They can stabilize reactive or low-coordinate species. Their role as organocatalysts—especially in umpolung transformations—has greatly broadened their synthetic range. The combination of electronic flexibility, steric control, and resistance to air and moisture makes NHCs distinct among ligand families[15, 17, 19].

2.2.1 Types of N-heterocyclic carbene ligands

The appearing of N-heterocyclic carbenes marked a turning point in organometallic chemistry. Their chemistry reshaped how researcher approach ligand design and catalysis. Stabilizing a divalent carbon atom with neighboring heteroatoms inside a cyclic framework introduced a new dimension to carbene chemistry, far beyond the short-lived nature of classical carbenes. Since demonstrating of the first stable imidazolylidene carbene compound in 1991, the field has expanded rapidly. Many NHC frameworks have been developed with adjustable steric and electronic properties[18, 23]. Their structural variety, strong donor ability, and chemical durability have given chemists a powerful platform for designing efficient homogeneous catalysts, metal–organic frameworks, and organocatalysts. This discovery began an era where fine control of the carbene core and heteroatoms allowed ligand properties to be tailored precisely for specific catalytic goals.

The earliest and most widely investigated families of NHCs are collectively referred to as classical or normal NHCs, where the carbene center is positioned at the carbon atom flanked by two heteroatoms, most commonly nitrogen, within a five- or six-membered ring. Classical NHCs include imidazolylidene, imidazolinylidene, benzimidazolylidene, thiazolylidene, oxazolylidene, and triazolylidene derivatives, among others[19, 22].

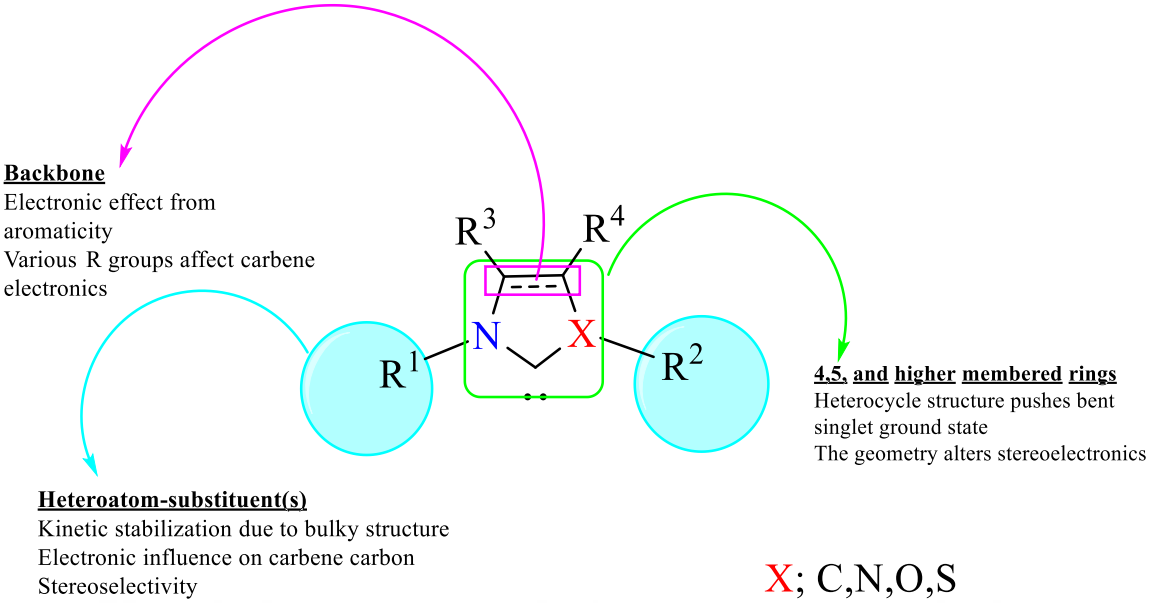

Figure 2.3 : General structural detailing of NHC skeleton.

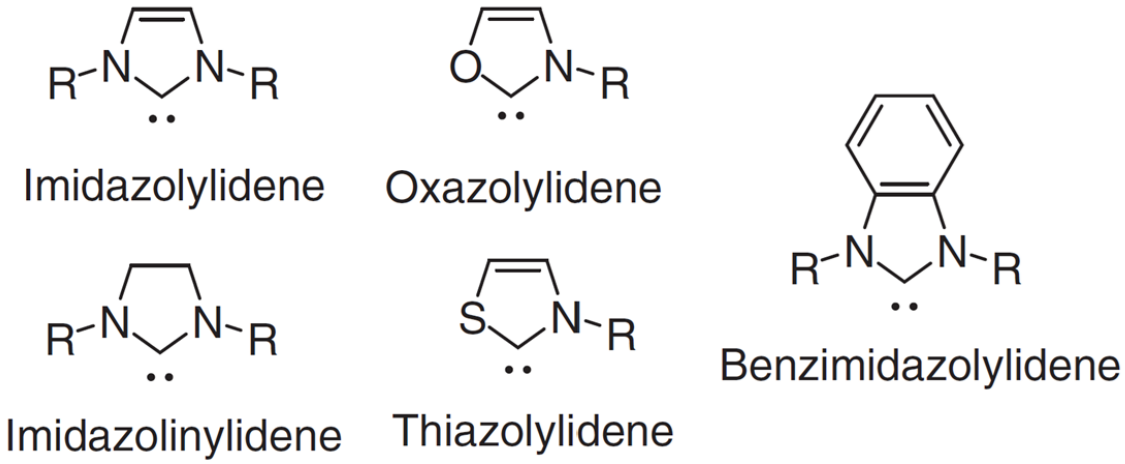

Figure 2.4 : Some classical type NHC structures**.**

Among these, imidazolylidene ligands remain archetypal representatives, offering an exceptional balance of σ-donor strength and thermal stability. Their electronic stabilization arises from delocalization within the aromatic imidazole ring, while steric protection is imparted through bulky N-substituents that prevent dimerization of the carbene species. Imidazolinylidenes, which contain a saturated backbone, display slightly stronger σ-donation due to the absence of π-delocalization, rendering them particularly suited for transition-metal complexes requiring higher electron density. Benzimidazolylidenes, on the other hand, incorporate a fused benzene ring that enhances rigidity and offers additional steric shielding close to the metal center, which can be advantageous for stabilizing reactive species. Thiazolylidene and oxazolylidene

carbenes represent variants in which one nitrogen atom is replaced by sulfur or oxygen, respectively, altering the donor softness and precursor acidity in predictable ways. The heavier sulfur atom in thiazolylidenes generally produces softer donor ligands. These species show stronger affinity toward late transition metals. In contrast, oxazolylidenes contain a more electron-deficient carbene center[21].

Figure 2.5 : Some nonclassical (remote, abnormal, and cyclicalkyl) NHC structures.

Triazolylidene ligands, characterized by a nitrogen-rich backbone, further extend the electronic tunability of this class and exhibit distinctive coordination behavior with both main-group and transition metals. Beyond the five-membered cores, ring-expanded systems such as six- and seven-membered pyrimidinylidene, perimidinylidene, and triazine-based carbenes have been developed to manipulate the N–C–N angle and consequently the steric profile surrounding the metal. These larger rings often strengthen σ-donation and provide more flexibility in catalyst design. Their easy preparation has made them widely used as stable and modular ligands in catalysis and coordination chemistry[24, 25].

The success of classical NHCs inspired research beyond the traditional C2-bound carbene center, leading to the development of non-classical or abnormal NHCs. In these systems, the carbene carbon occupies an unconventional site, often at the C4 or C5 (backbone carbons of an imidazole) the ring system. This shift in bonding profoundly changes the electronic structure, producing ligand structure that are usually stronger sigma donors and weaker π-acceptors than classical NHCs[18]. Such mesoionic or abnormal NHCs can stabilize metals in unusually low oxidation states and are useful in reactions requiring high electron density, including oxidative addition and difficult cross-coupling steps. A notable subgroup, the cyclic (alkyl)(amino)carbenes (CAACs), replaces one adjacent nitrogen with a quaternary carbon carrying alkyl groups. CAACs balance strong σ-donation with notable π-acceptor ability, enabling them to support both electron-rich and electron-poor centers. They also activate small molecules such as H_2, CO_2, and NH_3, showing unusual

reactivity in main-group chemistry. Another non-classical family, N,N-diamidocarbenes (DACs), features an amidinate-like framework that provides stronger steric shielding through a wider N–C–N angle and greater flexibility for chelation. Remote NHCs, where the carbene carbon is located farther from the heteroatoms, permit finer independent tuning of steric and electronic features. Together, these non-classical derivatives have expanded the boundaries of carbene chemistry, granting access to reactivity patterns that classical systems could not achieve[19, 26].

In comparison, the key difference between classical and non-classical NHCs lies in how they balance electronic donation, steric control, and synthetic flexibility. Classical NHCs are generally easier to synthesize. They show predictable coordination geometries and a well-balanced mix of donor strength and stability. Their straightforward preparation from azolium salts makes them suitable for large-scale use. Non-classical NHCs, although more challenging to prepare, provide greater electronic richness and distinctive bonding patterns that can reshape catalytic behavior. For example, the strong σ-donation of CAACs and abnormal NHCs promotes oxidative addition and stabilizes reactive intermediates. Their asymmetric molecular structure can also favor chiral induction and selectivity in asymmetric reactions. Both ligand families are modular, allowing fine adjustment of electronic and steric factors through ring size, heteroatom choice, and N-substituent modification for stereo selectivity. Overall, this broad chemical space defines their essential role in modern catalysis and continues to inspire the creation of new carbene architectures with finely tuned properties[16, 25, 27].

2.2.2 Synthetic methods of N-heterocyclic carbenes

Since their discovery, N-heterocyclic carbenes have turned out one of the striking, versatile ligand families in the region of coordination chemistry as well as catalyst science. In addition to their strong σ-donor ability also capacity to stabilize low-valent metals make them powerful alternatives to traditional phosphines. Phosphines are usually sensitive to air and moisture and tend to oxidize. In contrast, NHCs form very stable complexes due to their strong covalent bonding and low tendency to dissociate. NHCs` steric and electronic properties can also be tuned precisely by altering the ring size, backbone substituents, or N-substituent bulk. This flexibility gives them a unique modular character[25]. While phosphine ligands often link electronic and steric changes, limiting separate control, NHCs allow independent adjustment of both

factors. This makes them ideal for catalysts requiring high stability and reactivity. As a result, the creation of efficient synthetic routes for NHCs has been crucial to their broad use in organometallic chemistry, polymerization catalysis, and organocatalysis[17, 23].

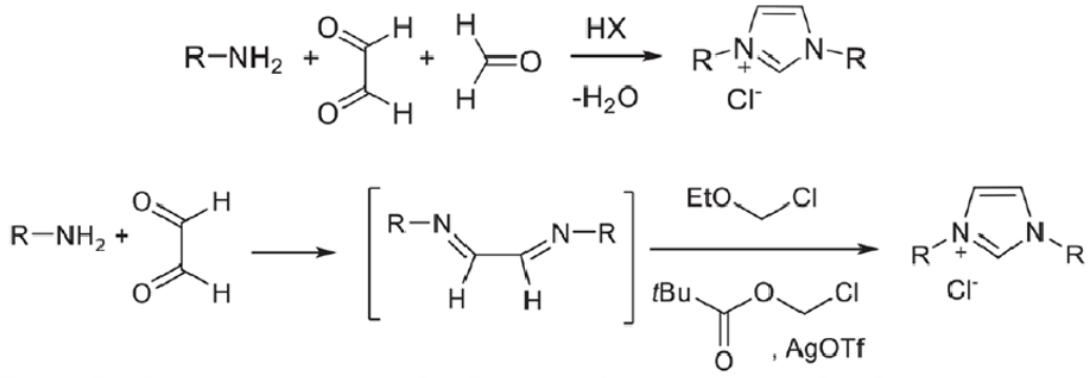

Figure 2.6 : Synthetic method of symmetric NHCs synthesis.

In a typical condensation–reduction sequence, primary amines react with glyoxal to generate diimines, which are subsequently reduced to the corresponding diamines. Cyclization of the diamine with triethyl orthoformate under acidic conditions affords imidazolinium salts, precursors of imidazolinylidene-type NHCs. The reduction step is omitted in the case of imidazolium salt formation, corresponding to the unsaturated imidazolylidene class. This approach is versatile and allows easy access to both symmetric and asymmetric derivatives by varying the amine substituents. Other variations of this route include bisacylation–reduction methods employing oxalyl chloride or ethyl oxalyl chloride, and acylation–alkylation strategies based on chloroacetyl chloride, both of which enable the synthesis of unsymmetrical imidazolium salts as exhibited in Figure 2.6. for symmetrical and Figure 2.7. for unsymmetrical NHCs.

Alternative synthetic pathways employ electrophilic C1 sources such as gem-dihalides, chloromethyl ethers, and chloromethyl pivalate (commonly known as Glorius' reagent). The latter, developed by Glorius and co-workers, is particularly effective for constructing rigid, sterically encumbered NHC architectures, especially those derived from bisoxazoline intermediates[17]. Other less conventional routes include the reduction of N-heterocyclic thiones with molten potassium, α-elimination or dehalogenation of haloimidazolines, and vacuum pyrolysis of NHC–adduct complexes. While these methods are more limited in scope, they provide access to unique NHC structures with unusual electronic properties, often used in specialized

applications such as small-molecule activation or surface coordination chemistry. The structural diversity of imidazolylidene and imidazolinylidene ligands achieved through these synthetic strategies underscores their unparalleled versatility as tunable platforms for ligand design and catalysis[23].

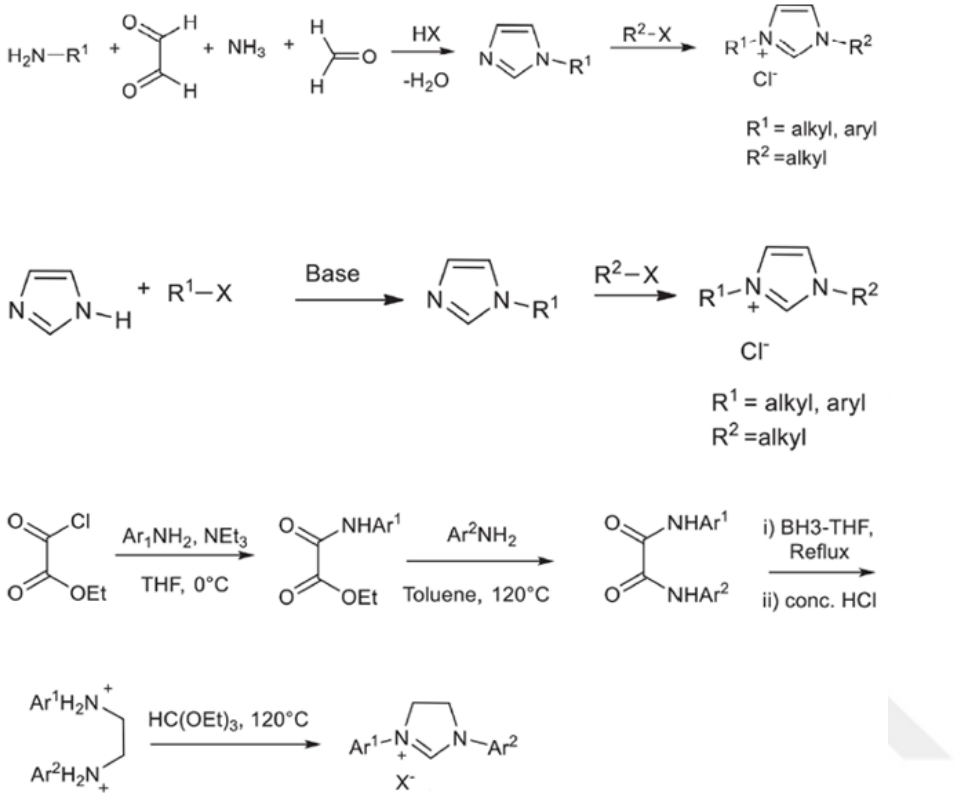

Figure 2.7 : Synthetic method of unsymmetric NHCs synthesis.

2.2.3 Iron–NHC complexes and its catalytic reactions

Iron–N-heterocyclic carbene (Fe–NHC) coordination complexes have embellished a key class of coordination compounds that represent the principles of green and sustainable chemistry. Iron element is the most abundant transition metal in the Earth's crust. Moreover, iron metal provides a cost-effective alternative to noble, highly expensive metals for instance ruthenium, palladium, and rhodium found in many catalytic transformations. Introducing NHC ligands into the coordination sphere of iron has transformed its catalytic and structural chemistry. This modification improves the stability, selectivity, and reactivity of iron complexes[28, 29]. Beside that iron's inherent advantages include its multiple accessible oxidation states, ranging from Fe(0) to Fe(III) and occasionally Fe(IV/V). Its ability to participate in both single- and two-electron redox processes makes Fe–NHC systems highly versatile for catalysis and small-molecule activation[30]. In addition to strong sigma donation ability and

pale π-accepting nature of NHCs allows formation of stable, electron-rich iron centers, marking a renewed era in iron organometallic chemistry.

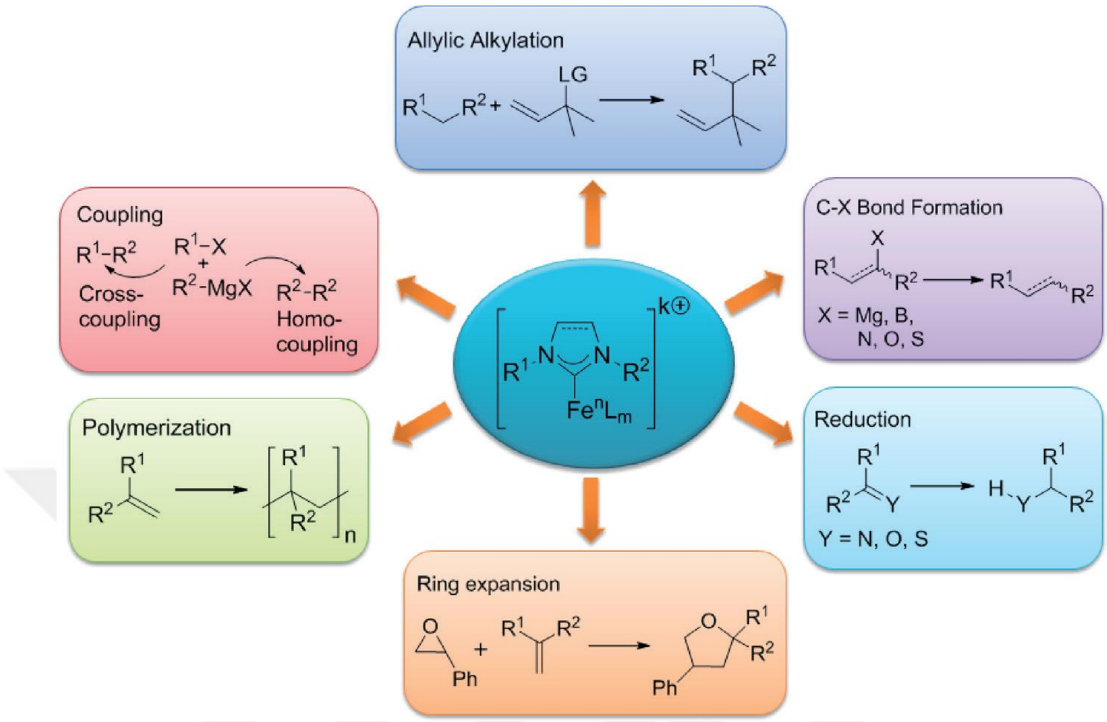

Figure 2.8 : Various catalytic transformation by Iron-NHC`s[31].

In Fe–NHC complexes, the bonding essence between the carbene carbon and the iron center is dominated by substantial σ-electron transfer. This effective donation enriches the electron density around the metal and contributes to the stabilization of iron across multiple oxidation states. The strong σ-donor effect gives the complexes exceptional thermal and chemical stability. Minimal π-backbonding helps prevent destabilization under oxidative conditions. As a result, Fe–NHC complexes display redox flexibility. The iron center can shift between Fe^{0}, Fe^{+1}, Fe^{+2}, and Fe^{+3} states without notable ligand damage[29]. The steric tunability of the NHC framework—through changes in ring size, backbone, and N-substituents—provides control over spin states and coordination geometry. Unlike phosphine ligands, which often undergo P–C bond cleavage or oxidation, NHC ligands maintain structural integrity under harsh catalytic conditions. This mix of electronic stability and tunability places Fe–NHC complexes in a unique position that combines high durability with active redox behavior. Such a balance is rarely found in other ligand systems[30].The catalytic profile of Fe–NHC complexes, displayed in Figure 2.8, is one of radical versatility. They operate with high efficacy

across a disparate landscape of reactions, uniting domains like synthetic coupling (C–C/X), reduction (hydrogenation), and polymer science (ATRP) under a single, efficient platform. Beside that in cross-coupling chemistry, Fe–NHC catalysts perform Kumada, Negishi, and Suzuki reactions under mild conditions. They offer practical alternatives to palladium-based systems. The Fe(II)/Fe(III) redox pair, stabilized by the strongly donating NHC ligand, supports both radical and two-electron pathways, increasing substrate scope. In hydrogenation and hydrosilylation, Fe–NHC catalysts reach or even surpass the activity of Ru and Ir analogues. At the same time, they are more economical and environmentally benign[28]. Fe–NHC catalyst usage in atom transfer radical polymerization revealed a new way of thinking by advancing in polymer chemistry by Grubbs and co-workers introduced [$(IiPrMe_2)_2FeX_2$], the first Fe–NHC complex applied in ATRP. This system mediates polymerization through a reversible redox cycle between Fe^{+2} and Fe^{+3}, similar to the Cu^{+1} and Cu^{+2} mechanism in conventional ATRP but with better environmental and economic profiles. The strong σ-donation from NHC ligands stabilizes the Fe(II) center and improves halogen abstraction efficiency. As a result, initiation becomes faster and molecular weight distributions narrower[32]. Compared with Cu-based systems, Fe–NHC catalysts leave less residual metal and resist oxidative deactivation. These traits are particularly beneficial for biomedical and coating uses. Although Cu catalysts often provide finer kinetic control of polymer growth, Fe-based systems are more biocompatible and can operate under milder conditions. The oxidation/reduction potential between Fe^{+2} and Fe^{+3} couple can also be tuned by changing the NHC backbone and substituents. This adjustment enables precise control of the activation–deactivation balance central to controlled radical polymerization[33]. Comparative studies show that Fe–NHC catalysts match Cu-based systems in polymer dispersity and extend usability to more polar monomers and aqueous media. Despite these advantages, Fe–NHC complexes face certain challenges. The presence of multiple spin states complicates mechanistic understanding. Advanced spectroscopic and computational tools are often needed to separate competing reaction pathways. Low-valent species remain sensitive to air and moisture, limiting their practicality. Although the range of Fe–NHC catalysis continues to expand, activity in some reactions still lags behind that of optimized noble-metal systems. Even so, ongoing work on robust, air-stable Fe^{+2} and Fe^{+3} precursors is encouraging. The use of chiral and pincer-type NHC frameworks is also helping to address these issues. Integrating Fe–NHC chemistry into sustainable

catalysis, polymer synthesis, and bioinspired activation illustrates its transformative potential in modern coordination and organometallic chemistry[34–37].

2.3 Controlled/Living Radical Polymerization

Modern polymer science was transformed by the development of Controlled/Living Radical Polymerization (CLRP). This technique, which IUPAC terms Reversible Deactivation Radical Polymerization (RDRP), introduced unprecedented precision to what was once a statistically controlled process. This technique provides exact control on molecular weight, distribution, and macromolecular structure. It overcomes the limitations of traditional free-radical polymerization that has two main unsolved problems; (i) irreversible chain termination and (ii) transfer reactions[38]. By establishing an equilibrium active and dormant species in a dynamic process, CLRP combines the robustness of traditional radical polymerization with the control typical of living anionic systems[39]. These methods enable the preparation of narrowly dispersed polymers and complex shaped structure—for example; star, block, graft, and network polymers. As a result, their employment extends broadly into biotechnology, nanotechnology, coatings, and smart materials.

The core idea of CLRP is that reversible deactivation of growing radicals suppresses bimolecular termination and chain transfer. The first evidence of “living” radical behavior came from Otsu’s iniferter systems in the early 1980s, which used thiuram disulfides for reversible activation and deactivation[40]. [40]. Later developments defined three main mechanistic classes as nitroxide-mediated polymerization (NMP), atom transfer radical polymerization (ATRP), and also reversible addition–fragmentation chain transfer (RAFT) polymerization. In all cases, the propagating radical alternates between active and dormant states. The result is a system where initiation is exceptionally efficient, and the polymer's molecular weight grows predictably with monomer consumption. This precise growth is evidenced by a linear evolution of molecular weight with conversion and a consistently low dispersity ($Đ < 1.5$), hallmarks of a well-controlled process. Such features define a living-like process where most polymer chains retain reactive end groups for block or chain-extension reactions[38, 41].

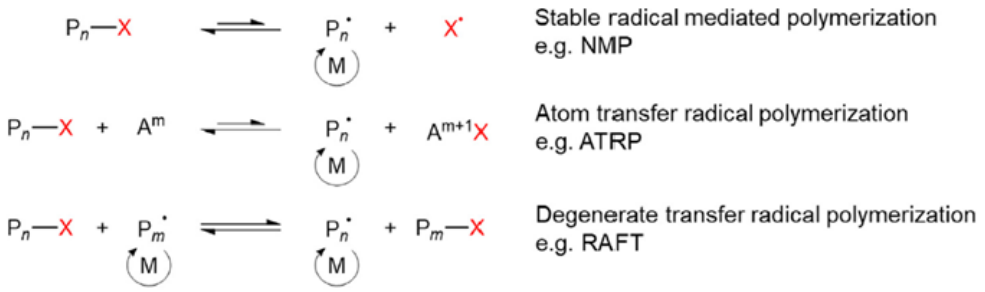

Figure 2.9 : General reaction mechanism of CLRP.

Mechanistically, maintaining control requires a dynamic equilibrium in which the concentration of active radicals stays very low compared with dormant species. This minimizes termination. Two main pathways define this balance. The first is the persistent radical effect (PRE), where a stable radical mediates reversible activation and deactivation, as in NMP and ATRP. The second involves degenerative transfer, in which chain activity shifts between dormant and active species through reversible addition–fragmentation steps, as seen in RAFT[39]. Both mechanisms promote uniform chain growth. However, the kinetic balance among activation, deactivation, and propagation rates determines the overall degree of control and "livingness." In optimized systems, polymerization rate and molecular weight evolution can be tuned by modifying the metal catalyst, ligand, and also control-agent structure. These strategies provide chemists with versatile tools for rational macromolecular design[42].

From a practical perspective, the versatility of CLRP has driven major progress in advanced material development. By tuning polymer architecture and composition, researchers have produced stimuli-responsive hydrogels, surface-grafted brushes, nanocarriers for drug delivery, and self-assembling block copolymers for electronic and photonic uses. The inherent robustness of radical mechanisms allows the use of many functional monomers and solvents, including water, ionic liquids, and supercritical CO_2, supporting green-chemistry approaches. New activation strategies—such as electrochemical (eATRP), photoinduced (photoATRP and PET-RAFT), enzymatic, and mechanically driven polymerizations—highlight the adaptability of CLRP systems. These innovations have reduced catalyst loadings, improved oxygen tolerance, and enabled spatial–temporal control. Together, they have expanded the industrial and biomedical significance of CLRP[38, 42].

2.3.1 Atom transfer radical polymerization(ATRP)

ATRP stands as a revolutionary technique in polymer science, moving beyond the limitations of conventional radical polymerization. It renders possible to advance materials along with unprecedented way, allowing for the precise preparation of polymers with targeted molecular weights, uniform dispersity, and bespoke structures, thus enabling the design of advanced functional materials. This level of control has opened broad applications in materials science, biomedical engineering, coatings, adhesives, and electronics. ATRP makes it possible to prepare block copolymers, graft copolymers, and complex architectures, leading to advanced materials with tailored properties. Significant efforts have been devoted to developing new ATRP catalysts to improve rate, control, and efficiency. Various metals for instance copper, iron, osmium, cobalt, and ruthenium have been explored to broaden the scope of ATRP and to enable new monomer systems. Ligand design plays a central role in regulating catalyst activity and selectivity. Recent progress has focused on ligands that improve catalytic efficiency, enhance the living character of polymerization, and expand monomer compatibility with ATRP[43–47].

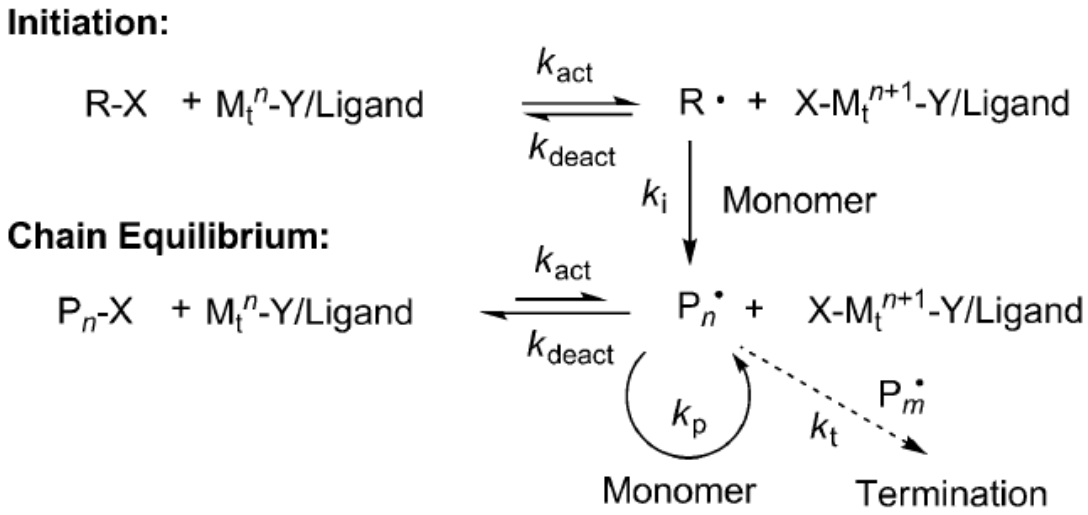

Figure 2.10 : Proposed ATRP mechanistic pathway.

Mechanistically, ATRP works through a reversible redox balance between active radical species and dormant alkyl halides. This equilibrium is mediated in the presence of transition metal and a ligand, most often a copper/ligand complex. This reaction proceeds via a homolytic atom transfer mechanism, in which the metal complex in its

low oxidation state (M^n/L) abstracts one halogen atom (X) from one organic halide initiator (R–X), generating a carbon-centered radical (R•) and the metal complex in its higher oxidation state (X–M^{n+1}/L). This carbon-centered radical reacts with monomer molecules to propagate the chain, after which it is quickly deactivated by the produced metal complex in its higher oxidation state, returning to the dormant R–X form[48]. This continuous activation–deactivation cycle maintains a very low steady-state radical concentration and minimizes bimolecular termination. The equilibrium constant ($K_{ATRP} = k_{act}/k_{deact}$) governs the degree of control and polymerization rate, depending on halogen type, ligand electronics, and solvent polarity. Efficient ATRP systems show linear molecular-weight growth with increasing conversion. They produce polymers with dispersities in the range of 1.1 to 1.3[49].

ATRP has become a powerful tool in macromolecular engineering, providing control over chain length, topology, and functional design. It allows predictable preparation of sophisticated materials such as block, comb, gradient, star, and bottlebrush copolymers. Its applications cover many fields: biomedicine (drug delivery systems, hydrogels, and bioconjugates), materials engineering (elastomers, nanocomposites, and coatings), electronics (conductive and dielectric films), and surface science (polymer brushes for antifouling and catalysis). Surface-initiated ATRP (SI-ATRP) has gained particular importance. It enables polymer chains to be covalently attached to nanoparticles, fibers, or metal oxides with molecular-level precision. Such coatings add stability, selective permeability, and responsiveness to surfaces, making ATRP essential for next-generation materials[50].

Beyond the classical ATRP system, different developed variants have been discovered to overcome issues of catalyst loading, oxygen sensitivity, and scalability. ARGET ATRP (activators regenerated by electron transfer) uses mild reducing chemicals for instance tin(II) octoate or ascorbic acid to continuously convert Cu(II) into Cu(I). This approach allows reactions to proceed with only a few parts per million of catalyst and provides excellent oxygen tolerance. ICAR ATRP (initiators for continuous activator regeneration) relies on conventional radical initiators like AIBN or peroxides to regenerate activator species during polymerization. It maintains good control even under open-air conditions, making it attractive for industrial applications. PhotoATRP, another widely used form, employs visible or UV light to photochemically regenerate

Cu(I) species from Cu(II) complexes. This method offers spatial and temporal control, enabling on-demand activation or deactivation of polymerization. Together, these approaches move ATRP toward more sustainable, energy-efficient, and precisely controlled polymerizations consistent with green chemistry principles. Their versatility supports uses ranging from high-performance coatings to biointerfaces and smart nanomaterials, bridging the gap between laboratory synthesis and industrial-scale production[49, 51, 52].

2.3.2 Initiators for continuous activator regeneration atom transfer radical polymerization (ICAR-ATRP)

Initiators for Continuous Activator Regeneration Atom Transfer Radical Polymerization (ICAR-ATRP) is a developed variant of ATRP that enables polymerizations with extremely low catalyst concentrations, typically at the ppm level. Originally introduced by Matyjaszewski and coworkers in 2007, ICAR-ATRP addresses the limitations of conventional ATRP systems that require relatively high metal catalyst loadings (0.1–1 mol%), which can cause issues with product purification and metal residues. In ICAR-ATRP, a conventional radical initiation by applying heat with azobisisobutyronitrile (AIBN) continuously produces free radicals to reduce transition-metal complexes (L/Cu^{+2}, L/Fe^{+3}) to their active lower states (L/Cu^{+1}, L/Fe^{+2}), which in turn activate alkyl halide initiators. This approach maintains an equilibrium in a dynamic way between aforementioned dormant and active species while minimizing catalyst requirements and improving oxygen tolerance, making the process industrially and environmentally attractive[53–55].

Mechanistically, ICAR-ATRP is controlled by a redox equilibrium between the oxidized and reduced states of a transition-metal coordination complex. For ICAR-ATRP, a conventional radical initiator decomposes thermally in order to regenerate radicals that are able to reduce the oxidized catalyst to its lower oxidation state. The reduced metal centers then intereact with an alkyl halide initiator (R–X) to form an active radical (R•) and a higher oxidation-state complex. The equilibrium constant determines the degree of polymerization control. A steady balance between activation and deactivation ensures uniform chain growth and narrow molecular-weight distribution. Unlike ARGET or AGET ATRP, ICAR-ATRP employs a continuous thermal initiator instead of a chemical reducing agent. This enables constant regeneration of activator species during polymerization. Copper, ruthenium, and iron

have been used as common transition metals in ICAR-ATRP systems. Iron is particularly attractive due to its low toxicity, cost-effective, and environmental compatibility. Typical ligands include triphenylphosphine (PPh_3), tris (2-pyridylmethyl) amine (TPMA), and N-heterocyclic carbenes (NHCs), which stabilize both the oxidized and reduced states of the metal. Polymerization is commonly initiated with alkyl halides such as ethyl 2-bromo isobutyrate (EBiB) or ethyl 2-bromo phenylacetate (EBPA), combined with thermally activated initiators like AIBN or 1,1′-azobis (cyclohexane carbonitrile) (ACHN). Solvents such as toluene, anisole, and tetrahydrofuran (THF) are typically used, and homogeneous systems maintain efficient control even in the presence of trace oxygen[53–58].

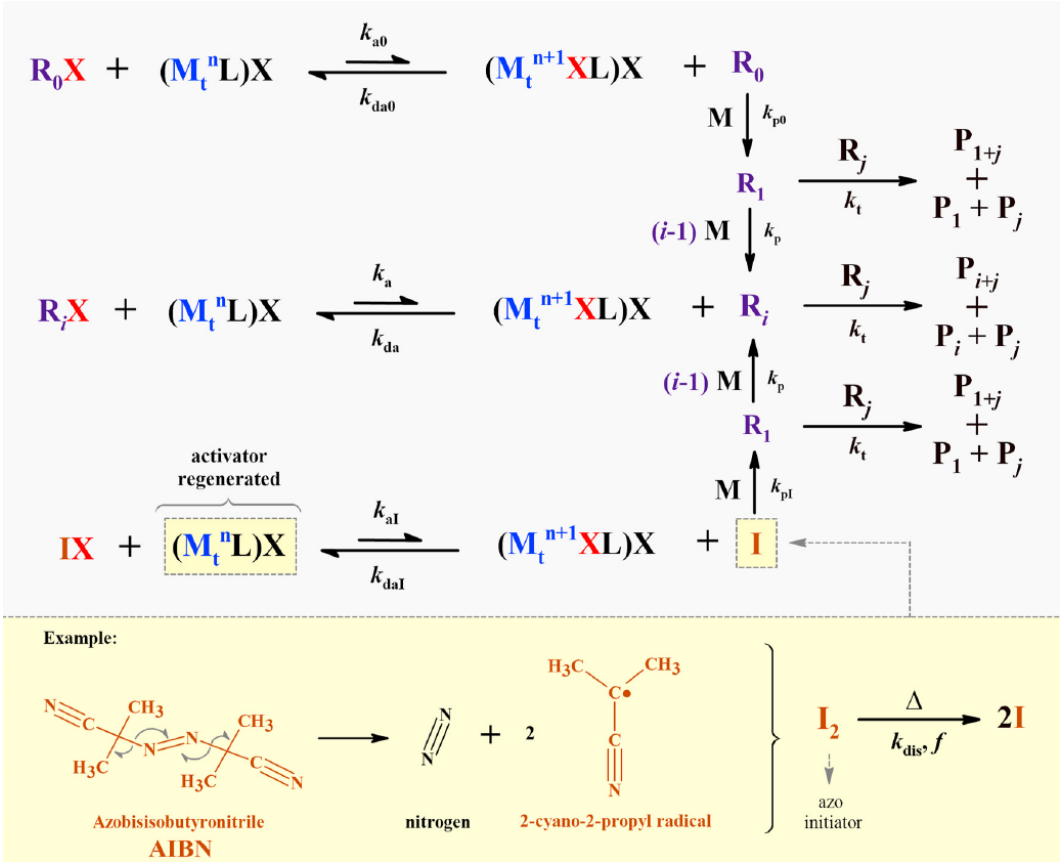

Figure 2.11 : Mechanistic illustration of ICAR-ATRP in the presence of AIBN.

The ICAR-ATRP technique provides significant benefits for industrial-scale and biomedical applications where minimal metal residue is required. Its low catalyst usage, compatibility with diverse polar monomers, and high oxygen tolerance make it ideal for continuous-flow and bulk polymerization processes.Polymers synthesized via ICAR-ATRP are widely applied in coatings, adhesives, nanocomposites, and

biomedical materials. The method also facilitates hybrid strategies such as photo-ICAR-ATRP and electrochemically mediated ICAR-ATRP, which introduce spatiotemporal control and further reduce catalyst loading[52, 58–60].

2.4 NHC-Based ATRP Catalyst Examples In Literature

Siyanin Atom Transfer Radical Polymerization (ATRP) in the presence of N-heterocyclic carbenes ligands was demonstrated over some literature examples from early proof-of-concepts into chemistry that is both mechanistically insightful and application-ready. The studies below collectively map that arc: from first demonstrations of highly donating NHCs on iron that rival Cu systems, to ppm-level ICAR protocols with air-stable Fe(III)–NHC precursors, and finally to fully aqueous ATRP using Ru–NHC catalysts designed for water—together illustrating how NHC electronics and ligand topology can be tuned to control activation/deactivation, dispersity, and practical handling at low catalyst loadings.

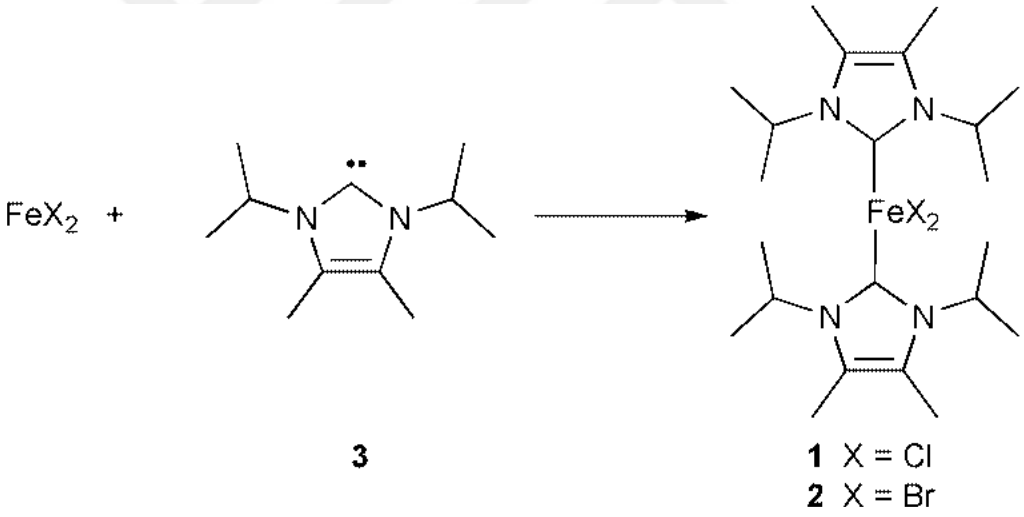

Figure 2.12 : Louie & Grubbs study for dihalide example of NHC catalyst.

Louie & Grubbs reported discrete Fe(II) dihalide complexes bearing a strongly donating imidazolylidene [1,3-diisopropyl 4,5-dimethyl imidazolylidene] that catalyze ATRP reaction of styrene (1-PEBr, 50% toluene, 85 °C) and MMA (EBiB, 50% benzene, 60 °C) with fast kinetics and excellent control. For styrene, $k_{obs} \approx 3.4\times10^{-5}$ s^{-1} ($FeCl_2$–NHC) with linear Mn vs conversion and Mw/Mn is near to 1.1 (further narrowed to ~1.05 upon adding $FeCl_3$ to bias dormancy). For MMA, $FeBr_2$–NHC gave $k_{obs} \approx 1.6\times10^{-4}$ s^{-1} and Mw/Mn ~1.09–1.47 depending on deactivator level; in both monomers the bromo complex outpaced the chloro analogue, consistent with weaker

M–Br bonds. These data established that highly basic NHCs lower the iron redox potential, accelerate halide abstraction, and still preserve control by stabilizing Fe(III) during rapid exchange[61].

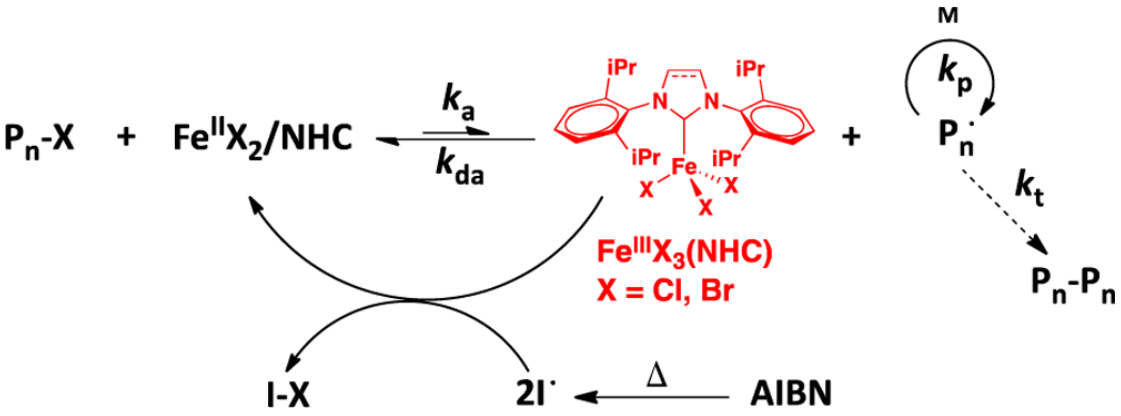

Figure 2.13 : Okada, Park & Matyjaszewski study for ICAR-ATRP.

Okada, Park & Matyjaszewski advanced Fe–NHC catalysis into ICAR-ATRP at ppm iron using air-stable FeX_3(NHC) (X = Cl, Br; NHC = IDipp or HIDipp). With MMA (200:1:0.01:0.2 = [M]/[EBrPA]/[Cat.]/[AIBN], 50% anisole, 60 °C), 50 ppm catalyst reached ~64–65% conversion in 24 h, delivering PMMA with $Mn^{(th)} \approx$ Mn(GPC) and Mw/Mn = 1.20–1.23 for Br complexes (H–Br, I–Br), whereas Cl analogues were slightly broader (Mw/Mn ≈ 1.40–1.45). With styrene under analogous ICAR conditions (72 h), Br complexes again gave narrower distributions (Mw/Mn 1.13–1.19 at ~52–53% conv.). CV showed NHCs render FeX_3 more reducing ($E_{½}$ down to −0.48 V vs Fc/Fc^+), rationalizing efficient activator regeneration and control at ultra-low loadings without TBAX/PPh_3 additives[62].

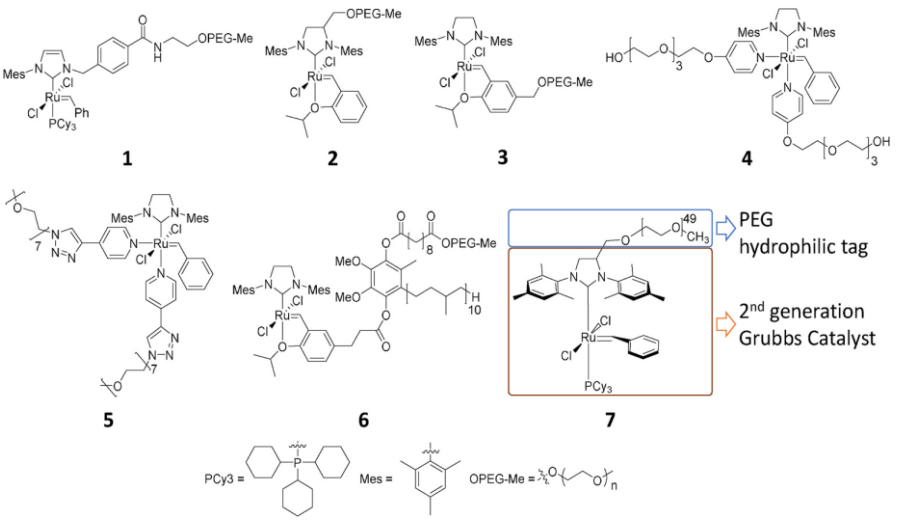

Figure 2.14 : Kim, Kim & Chung study for aqueous ATRP catalyst design.

Kim, Kim & Chung designed a PEG-tethered Ru–NHC benzylidene (Grubbs-type) catalyst "7" that is homogeneous and highly soluble in water, enabling aqueous ATRP (neat H_2O, no co-solvent/surfactant) of acrylamide, SBMA (zwitterion), and PEGMEMA with typical ATRP signatures: first-order kinetics, linear Mn–conversion, and decreasing dispersity. With SBMA at 80 °C and 0.05 mol% catalyst ([M]/[I]/[Cat] = 200/1/0.1), 91% conversion in 6 h gave polySBMA with Mn ≈ 335 kDa and PDI 1.66; acrylamide reached 90% in 8 h (PDI 1.38). Chain-extension from polySBMA-Br to SBMA-b-PEGMEMA produced a unimodal GPC shift (PDI ~1.24), confirming preserved ω-Br ends. The study also benchmarked solvent and concentration effects (faster in water than MeCN; higher [M] accelerates) and discussed initial induction consistent with halide-assisted activation ofRu-benzylidene[63].

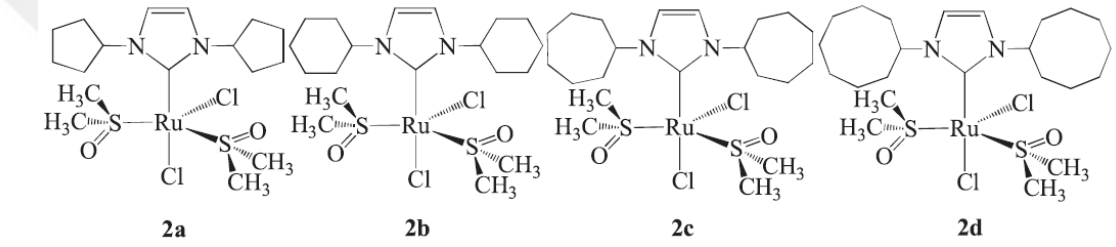

Figure 2.15 : Idehara et al. designed Ru(II)–NHC dimethyl-sulfoxide complexes.

Idehara and co-worker synthesized a family of Ru(II)–NHC dimethyl-sulfoxide catalysts. [$RuCl_2$(S-dmso)$_2$(NHC)] bearing cycloalkyl-substituted imidazolylidenes (IPent, IHex, IHept, IOct; complexes 2a–2d) and evaluated them as dual-function catalysts for ROMP and ATRP. For ROMP of norbornene (CH_2Cl_2, 50 °C) they required ethyl diazoacetate (EDA) to reproduce the metathetically active Ru–carbene; polymer yields rose with time but showed broad dispersities (PDI ≈ 1.6–4.0; Mn ≈ 2.2×10^3–5.7×10^3 g mol^{-1}) and an activity order 2a > 2b > 2c > 2d, attributed to steric control of the initiation step via S-dmso labilization. For ATRP reaction of polar methyl methacrylate (toluene, 85 °C; [MMA]/[EBiB]/[Ru] = 1000/2/1), all four complexes displayed controlled kinetics with linear ln([M]$_0$/[M]) vs time also Mn increasing with consumption while PDI decreased; first-order rate constants rose with NHC bulk (k_{obs} ≈ 1.52×10^{-5}, 2.29×10^{-5}, 2.73×10^{-5}, 3.70×10^{-5} s^{-1} for 2a–2d). After 12 h, 2d reached ~77% conversion with PDI ≈ 1.09 (Mn ≈ 4.1×10^4 g mol^{-1}), while 2a gave ~48% conversion with PDI ≈ 1.45 (Mn ≈ 3.6×10^4 g mol^{-1}). Electrochemistry showed reversible Ru(II/III) couples (E½ ~0.65–0.70 V vs Ag/AgCl) consistent with efficient activation/deactivation in ATRP and highlighted how NHC σ-donation plus

DMSO coordination tune redox and ligand-exchange steps to enable both ROMP and ATRP in a single, accessible platform[64].

3. EXPERIMENTAL

3.1 Materials And Methods

Toluene (Aldrich %98) and DMF (Aldrich %98) were dried by vacuum distillation while stirring with magnesium sulfate. Ethanedithiol (Aldrich %98), hexanedithiol (Aldrich %98), thiophenol (Aldrich %98), Ethyl α-bromo isobutyrate (EBIB) (Aldrich %98) and BHT-free tetrahydrofuran (THF) were used as received without distillation. Methyl methacrylate (MMA) was filtrated by column filtration over basic alumina. All other chemicals used as purchased from commercial supplier. Chromatographic purification was realized using Merck Silica 60. For monitoring purposes, Thin-layer chromatography was carried out utilizing Merck TLC Silicagel 60 F254 plates, and monitoring was performed inside UV cabin that has light at 254 and 357 nm.

^{1}H-NMR experiment were run at room temperature by Agilent NMR system V NMRS 500 Spectrometer using CDCl3 as solvent containing TMS as internal standard. Chemical shifts will be recorded in ppm units using tetramethylsilane standard at zero ppm and either undeutoriated DMSO trace in d_6-DMSO or CHCl3 trace in CDCl3 as an internal standard for 2.50 ppm and 7.27 ppm respectively. GPC measurements were performed by TOSOH EcoSEC GPC equipped with an autosampler system, TSK gel superhZ2000 4,6mm ID, 15 cm length, 2 cm width column and refractive index detector. THF solvent was utilized as the eluent with a flow rate of 1 mL/min^{-1} at 40oC. Refractive index detector was calibrated with PS internal standard. Both detectors were calibrated with PS standards in the narrow molecular weight distribution. Three ViscoGEL GPC columns (G2000HHR, G3000HHR and G4000HHR) employed with THF in the 1.0 mL min-1 flow rate at 300 C. All data were analyzed utilizing Viscotek OmniSEC Omni-01 software. Size exclusion chromatography results were analyzed by using ECO-SEC Analysis software. FTIR spectrums were recorded by using Perkin–Elmer FT-IR Spectrum One B spectrometer.

3.2 Synthetic Procedures

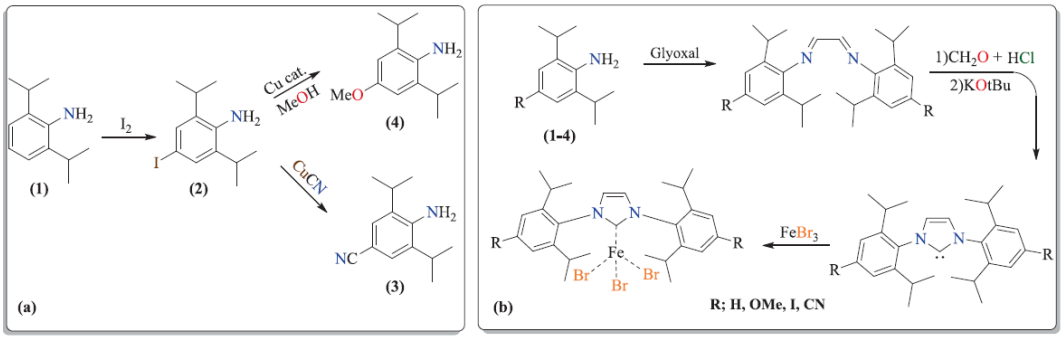

Figure 3.1 : General reaction scheme for the preparation of 2,6-diisopropyl anilines (a), and the Fe-based NHC catalysts (b).

Para-substituted aniline derivatives serve as versatile precursors for synthesizing symmetrical N-heterocyclic carbenes (NHCs). In this approach, aniline compounds are first reacted with glyoxal to form diimine intermediates. These intermediates are then cyclized by reaction with formaldehyde under acidic (HCl) conditions to produce the corresponding ligand frameworks. Subsequent treatment of the ligands with potassium tert-butoxide (KOtBu) affords the free carbene species—NHC-H, NHC-I, NHC-OMe, and NHC-CN. Finally, coordination with $FeBr_3$ generates the iron-based ATRP catalysts FeNHC-H, FeNHC-I, FeNHC-OMe, and FeNHC-CN under nitrogen atmosphere.

3.2.1 Synthesis of 2

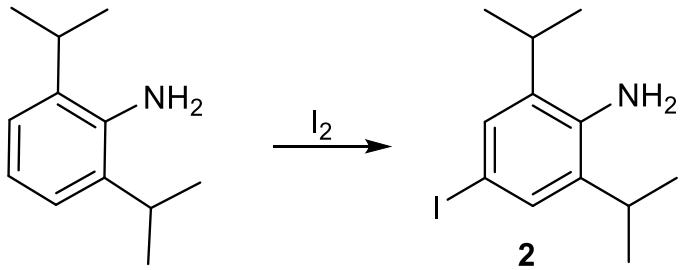

Figure 3.2 : Synthesis of 2.

4.4 g 2,6 diisopropylaniline (%92), (22.8 mmol, 1eq) taken in 50 ml of diethyl ether with 50 ml saturated $NaHCO_3$ solution added. Then, 6.85 g I_2 (26.9 mmol, 1.2 eq) put in and let to mix at ambient condition(RT) for 5 hours. Then after, 0.85 g $Na_2S_2O_3$ was added into the solution to oxidize the excess amount of I2 and allowed to stir until water phase become clear (app. 10 minutes). The water phase discarded, and organic phase treated to wash with water (50 ml x 2). Finally, the organic phase (top) dried

with sodium sulfate, and ether removed by distillation. Yield 95%. HR-MS calc. 304.0557, Expr. 304.0563. ^{1}H NMR (400 MHz, Methylene Chloride-d_2) δ 7.27 (s, 2H), 3.79 (s, 2H), 2.85 (hept, J = 6.8 Hz, 2H), 1.23 (dd, J = 6.8, 1.8 Hz, 12H). ^{13}C NMR (101 MHz, Methylene Chloride-d_2) δ 143.06, 137.70, 134.20, 83.20, 30.44, 24.65.

3.2.2 Synthesis of 3

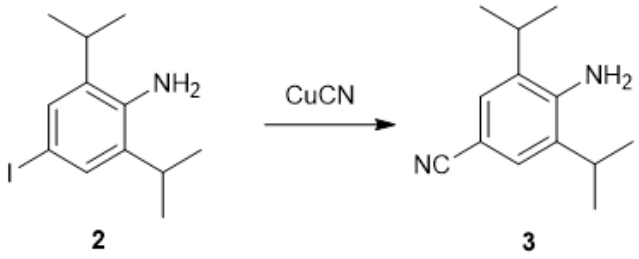

Figure 3.3 : Synthesis of 3.

1.00 g of **2** (3.3 mmol, 1eq) and 1.48 g of CuCN (16.5 mmol, 5 eq) were placed into a glass vessel with a stirring bar and brought into the glovebox. 17 ml of DMF was taken into the vessel. After that, the vessel was put in a hot bath (silicone oil) at 120 °C to allow to stir for 1 day (1440 min). At the end of the time, the reaction solution was brought to RT and poured into 0.1 L of 0.1M HCl solution. The organics conveyed to ethyl acetate (80 ml x 2) phase and mixed with saturated $NaHCO_3$ (0.1 L) and distilled water (0.1 L), respectively. Finally, the organic layer was dried with sodium sulfate and distilled to obtain the brownish solid. Yield 91%. (In case of impurities a silica gel column can be used to purify with a solvent mixture of hexane/EtOAc (4/1), Rf=0.6). HR-MS calc. 203.1543 expr. 203.1543. ^{1}H NMR (400 MHz, Methylene Chloride-d_2) δ 7.29 (s, 2H), 4.31 (s, 2H), 2.87 (hept, J = 6.8 Hz, 2H), 1.25 (d, J = 6.8 Hz, 12H). ^{13}C NMR (101 MHz, Methylene Chloride-d2) δ 144.93, 132.15, 127.15, 120.87, 99.81, 27.72, 21.69.

3.2.3 Synthesis of 4

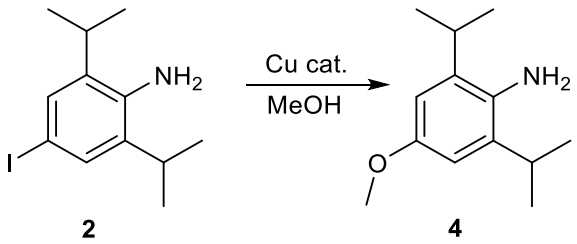

Figure 3.4 : Synthesis of 4.

A 0.02 L of scintillation glass vessel was filled along 2.930 g of **2** (9.7 mmol, 1.0 eq), 0.184 g of CuI (0.97 mmol, 0.1 eq), 0.400 g 3,5 dimethyl phenanthroline (1.92 mmol, 0.15 eq), 5.580 g Cs_2CO_3 (19.4 mmol, 1.5 eq), and 5 ml of toluene in glovebox. The glass reaction vessel was put in oil bath at 80 C and allowed to stir for 20 minutes. Then, 0.931 g of methanol (29.1 mmol, 3.0 eq) was added with syringe over septum and allowed to stir for 28 hours. 0.05 L of ethyl acetate taken into to the solution to dilute it and filtered over paper filter to remove solids and evaporated. Hexane/ethyl acetate (9/1) solvent mixture used in silica gel column to purify the red-oily compound, Rf=0.45. Yield 65%. HR-MS Calc. 208.1692, Expr.208.1696. ^{1}H NMR (400 MHz, Methylene Chloride-d_2) δ 6.63 (s, 2H), 3.75 (s, 3H), 3.48 (s, 2H), 2.97 (p, J = 6.8 Hz, 2H), 1.26 (dd, J = 6.8, 0.6 Hz, 12H). ^{13}C NMR (101 MHz, Methylene Chloride-d2) δ 152.75, 134.15, 134.07, 108.54, 55.39, 28.07, 21.98.

3.2.4 Synthesis of diimine-I

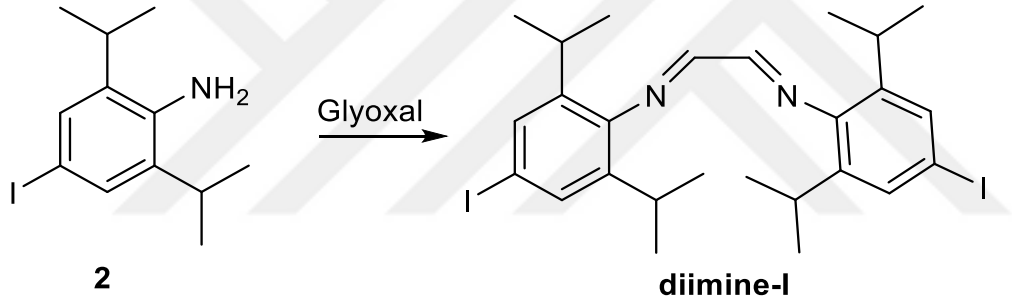

Figure 3.5 : Synthesis of diimine-I.

A strring bar, 600 mg of **2** (1.98 mmol) and 156 mg of 40% glyoxal (0.99 mmol) were put in a 0.05 L of round bottom flask. Then,7 ml of methanol and 150 µl of formic acid were added into the flask and allowed to mix at 323 K for 12 hours. After that, the yellow precipitation was filtered and washed with cold methanol (10 ml x 2). Yield 70 %. HR-MS Calc. 629.1542, Expr. 629.0872. ^{1}H NMR (400 MHz, Methylene Chloride-d2) δ 8.06 (d, J = 1.6 Hz, 2H), 7.49 (s, 4H), 2.85 (h, J = 6.9 Hz, 4H), 1.17 (d, J = 7.0 Hz, 24H). ^{13}C NMR (101 MHz, Methylene Chloride-d2) δ 165.94, 150.49, 141.96, 135.03, 92.45, 30.37, 25.55.

3.2.5 Synthesis of diimine-CN

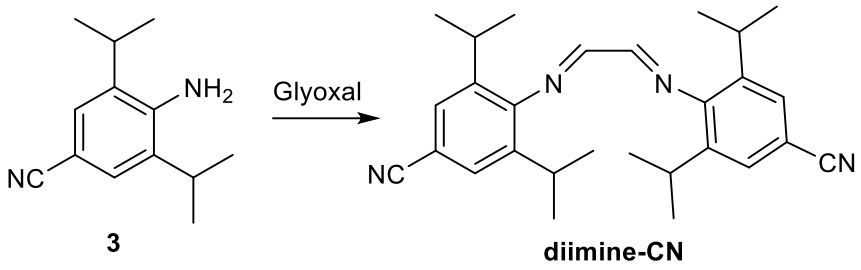

Figure 3.6 : Synthesis of diimine-CN.

600 mg of **3** (2.97mmol), 234 mg of 40% glyoxal (1.49 mmol) were put into a 48 ml pressure safe glass vessel with a stirring bar. 4 ml of hot ethanol and 0.150 ml of formic acid were taken into this vessel which was irradiated for 10 minutes with an irradiation power of 300 W. After that, ethanol was removed by rotary evap. and the yellowish solid loaded into a silica gel column to obtain the yellow solid with the solvent system of hexane/ethyl acetate (4/1), Rf=0.9. Yield 65% HR-MS calc. 427.2856, expr.427.2881. ^{1}H NMR (400 MHz, Methylene Chloride-d2) δ 8.08 (s, 2H), 7.49 (s, 4H), 2.90 (p, J = 7.0 Hz, 4H), 1.20 (d, J = 6.8 Hz, 24H). ^{13}C NMR (101 MHz, Methylene Chloride-d2) δ 165.43, 154.26, 140.50, 130.19, 122.10, 111.37, 30.73, 30.32, 25.27.

3.2.6 Synthesis of diimine-OMe

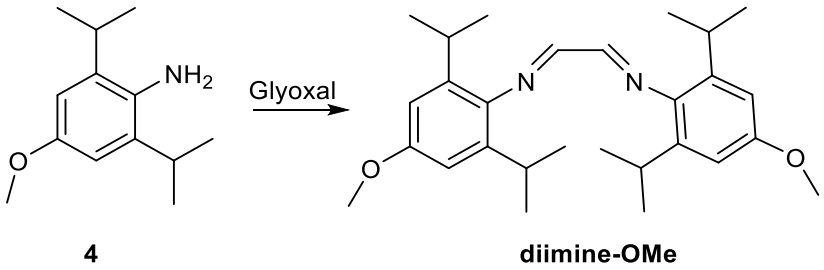

Figure 3.7 : Synthesis of diimine-OMe.

A stirring bar 600 mg of **4** (2.88 mmol) and 208 mg of 40% glyoxal (1.44 mmol) were taken in a 0.05 L of round bottom flask. Then, 7 ml of methanol and 150 µl of formic acid were added into the flask and allowed to stir at 50 °C for 12 hours under nitrogen atmosphere. After that, the yellow precipitation was filtered and cleaned with cold methanol (10 ml x 2) finally dried under vacuum. Yield 80%. HR-MS Calc. 437.3153, Expr. 437.3174. ^{1}H NMR (400 MHz, Methylene Chloride-d2) δ 8.07 (d, J = 1.0 Hz, 2H), 6.73 (s, 4H), 3.81 (d, J = 1.0 Hz, 6H), 2.98 (hept, J = 6.9 Hz, 4H), 1.19 (d, J = 7.0

Hz, 24H). ^{13}C NMR (101 MHz, Methylene Chloride-d2) δ 163.64, 157.22, 141.73, 138.59, 108.62, 55.16, 28.11, 23.10.

3.2.7 Synthesis of NHC-H

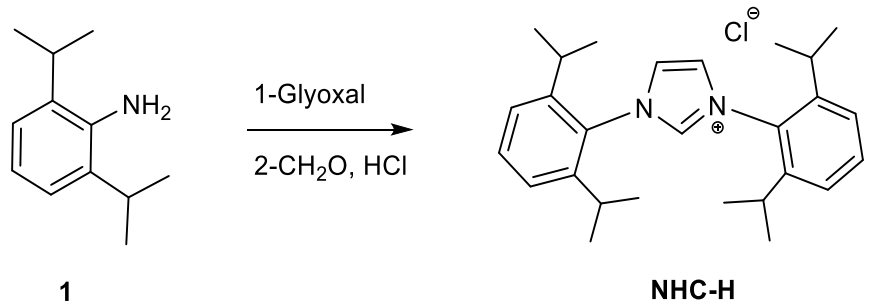

Figure 3.8 : Synthesis of NHC-H.

A stirring bar and 2 .00 g diisopropyl aniline **1** (11 mmol) were put into a 0.1 L of round bottom flask. 6 ml isopropyl/water (6/4) mixture containing 0.82 g %40 glyoxal solution (5.6 mmol) was placed into the flask and allowed to mix at ambient condition (RT) for 12 hours. After that, the yellow precipitation was filtered and washed with water (10ml x 2) and methanol (5ml x 2). After washing step, the precipitate was dried and used for further step without additional purification. 1.00 g yellow powder (diimine) was put into an oven dried 0.05 L of round bottom flask with a stirring bar and dissolved in 20 ml of dried toluene by stirring at 60 °C. In a separate vial, 95.6 mg paraformaldehyde (3.2 mmol, 1.2 eq) and 1.00 ml of 4M HCl in dioxane (4 mmol, 1.5 eq) stirred at hot plate until all solid dissolved and transferred into the diimine solution with a pipette drop by drop. After completion of addition, the flask taken out from hot bath and stirred at RT for 4 hours. The white precipitate was filtered over paper filter and washed with ethyl acetate (10 ml) and diethyl ether (10 ml). Yield 80%. HR-MS calc. 389.2957, expr. 389.2972. ^{1}H NMR (400 MHz, Methanol-d4) δ 9.96 (p, J = 1.8 Hz, 1H), 8.26 (d, J = 2.4 Hz, 2H), 7.67 (td, J = 7.9, 3.0 Hz, 2H), 7.56 – 7.47 (m, 4H), 2.54 – 2.39 (m, 4H), 1.28 (dtd, J = 30.5, 4.1, 2.0 Hz, 24H). ^{13}C NMR (101 MHz, Methanol-d4) δ 147.78, 142.39, 134.63, 132.75, 128.84, 127.23, 31.65, 26.02, 25.14.

3.2.8 Synthesis of NHC-I

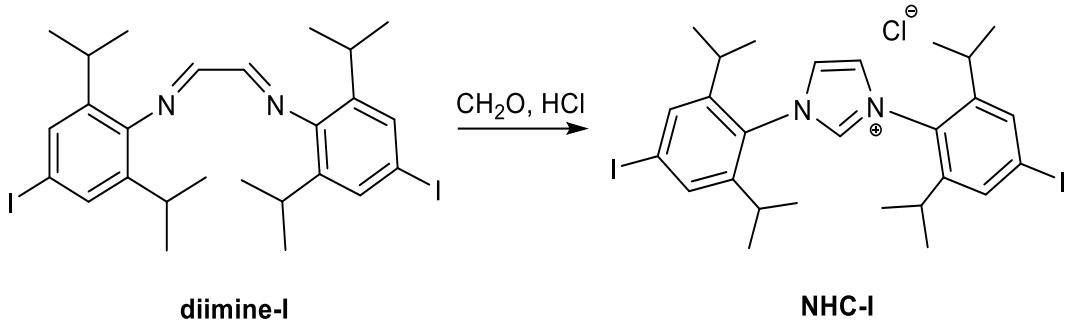

Figure 3.9 : Synthesis of NHC-I.

400 mg of 14 (0.64 mmol) was taken into an pre-dried 0.05 L of round bottom flask in oven with a stirring bar and dissolved in 10 ml of dried methyl benzene by stirring at 60 °C. In a separate vial, 23 mg paraformaldehyde (0.76 mmol, 1.2 eq) and 0.25 ml of 4M HCl in dioxane (0.96 mmol, 1.5 eq) stirred at hot plate until all solid dissolved and transferred into the 14 solution with a pipette drop by drop. After finishing of addition, the reaction solution allowed to mix at ambient condition (RT) for 8 hours. The white precipitate was filtered over paper filter and cleaned with ethyl acetate (0.01 L x 2) then, Et2O (0.01 L x 2). Yield 80%. HR-MS calc. 641.0890, expr.641.0935 ^{1}H NMR (400 MHz, Methanol-d4) δ 10.05 (s, 1H), 8.31 (d, J = 1.5 Hz, 2H), 7.83 (s, 4H), 2.37 (p, J = 6.7 Hz, 4H), 1.29 (d, J = 6.7 Hz, 12H), 1.21 (d, J = 6.8 Hz, 12H). ^{13}C NMR (101 MHz, Methanol-d4) δ 149.89, 142.27, 136.77, 132.57, 128.98, 101.16, 31.57, 25.84, 24.90.

3.2.9 Synthesis of NHC-CN

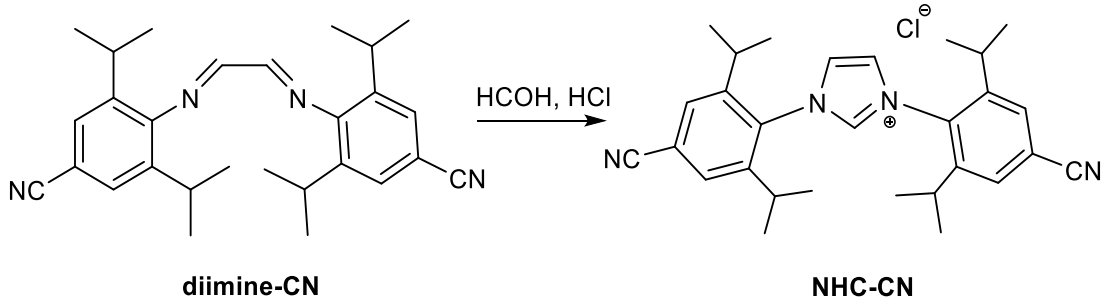

Figure 3.10 : Synthesis of NHC-CN.

500 mg of 12 (1.14 mmol) was taken into a pre-dried 50 ml of round bottom flask in oven with a stirring bar and dissolved in 10 ml of dried methyl benzene by stirring at 90 °C. In a separate vial, 41 mg paraformaldehyde (1.36 mmol, 1.2 eq) and 0.43 ml of

4M HCl in dioxane (1.71 mmol, 1.5 eq) stirred at hot plate until all solid dissolved and transferred into the diimine solution with a pipette drop by drop. After completion of addition, the reaction solution allowed to mix for 8 hours. The white precipitate was filtered over paper filter and cleaned with ethyl acetate (0.01 L x 2) and diethyl ether (0.01 L x 2). Yield 20%. HR-MS calc. 439.2862 expr. 439.2882. ^{1}H NMR (400 MHz, Methanol-d4) δ 10.24 – 10.17 (m, 1H), 8.44 (d, J = 1.6 Hz, 2H), 7.93 (s, 4H), 2.48 (p, J = 6.9 Hz, 4H), 1.34 (d, J = 6.8 Hz, 12H), 1.26 (d, J = 6.9 Hz, 12H). ^{13}C NMR (101 MHz, Methanol-d4) δ 149.86, 142.00, 136.14, 131.54, 129.04, 119.87, 119.01, 31.94, 31.88, 31.83, 26.33, 25.87, 25.69, 24.81, 24.72, 24.04.

3.2.10 Synthesis of NHC-OMe

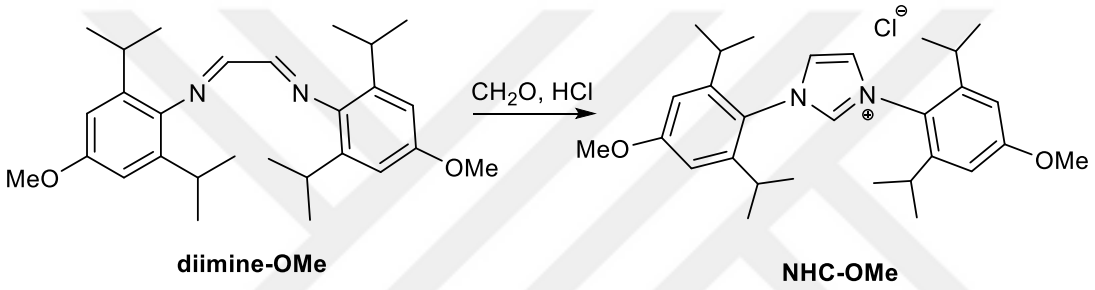

Figure 3.11 : Synthesis of NHC-OMe.

500 mg of 13 (1.15 mmol) was taken into a pre-dried 50 ml of round bottom flask in oven with a stirring bar and dissolved in 10 ml of dried methyl benzene by stirring at 60 °C. In a separate vial, 41 mg paraformaldehyde (1.37 mmol, 1.2 eq) and 0.43 ml of 4M HCl in dioxane (1.73 mmol, 1.5 eq) stirred at hot plate until all solid dissolved and transferred into the 13 solution with a pipette drop by drop. After finishing the addition, the reaction solution allowed to mix at ambient condition (RT) for 8 hours. The white precipitate was filtered over paper filter and cleaned with ethyl acetate (0.01 L x 2) and diethyl ether (0.01 L x 2). Yield 80%. HR-MS Calc. 449.3168, Expr. 449.3277. ^{1}H NMR (400 MHz, Methylene Chloride-d2) δ 10.79 (d, J = 1.7 Hz, 1H), 7.73 (d, J = 1.6 Hz, 2H), 6.83 (s, 4H), 3.88 (s, 6H), 2.43 – 2.34 (m, 4H), 1.24 (d, J = 6.8 Hz, 12H), 1.20 (d, J = 6.9 Hz, 12H). ^{13}C NMR (101 MHz, Methylene Chloride-d2) δ 161.87, 146.72, 140.88, 125.93, 122.82, 109.81, 55.48, 29.24, 24.26, 23.22.

3.3 Polymerization Experiments

3.3.1 Polymerization procedure for MMA

Stock solutions of the NHC catalyst (0.0235M) complexes were prepared in THF. The reactants were added into a stir bar equipped 25 mL Schlenk flask in the order of anisole, MMA, catalyst solution, and EBIB under nitrogen flow. Three freeze pump thaw series applied to the regarding solution in order to degas the system, and then AIBN was taken in when the titled solution was crystallized at the third set, yielding a stoichiometry of [MMA]/[EBIB]/[Catalyst]/[AIBN] = 200/1/0.01/0.2 where [MMA] = 4.7M. The flask was closed up and put in a hot bath at 60 °C. The regarding solution was diluted with THF. To remove the iron catalysts, mentioned diluted reaction mixture flowed in a column of neutral alumina, and analyzed by GPC using calibration based on polystyrene standards.

3.3.2 Polymerization procedure for styrene

Stock solutions of the NHC catalyst (0.0235M) complexes were prepared in THF. The reactants were added into a stir bar equipped 25 mL Schlenk flask in the order of anisole, styrene, catalyst solution, and EBIB under nitrogen flow. Three freeze pump thaw series applied to the regarding solution in order to degas the system, and then AIBN was taken in when the titled solution was crystallized at the third set, yielding a stoichiometry of [Styrene]/[EBIB]/[Catalyst]/[AIBN] = 200/1/0.01/0.2 where [styrene] = 4.7M The flask was closed up and put in a hot bath at 60 °C. The regarding solution was diluted with THF. To remove the iron catalysts, mentioned diluted reaction mixture flowed in a column of neutral alumina, and analyzed by GPC using calibration based on polystyrene standards.

3.4 Electrochemical Measurements

The electrochemical characterization was carried out via cyclic voltammetry (CV) in a rigorously controlled environment to ensure data integrity. The solvent, dichloromethane, was dried and degassed to eliminate moisture and oxygen, thereby preventing solvent coordination to the metal center or other side reactions. A 0.2 M tetrabutylammonium hexafluorophosphate (Bu_4NPF_6) solution acted as the supporting electrolyte, and the entire experiment was conducted under an inert argon atmosphere. A three-electrode configuration was employed, consisting of a boron-doped diamond

(BDD) working electrode, a platinum counter electrode, and a silver wire pseudo-reference electrode. The internal standard ferrocene was used for potential calibration. The voltammograms were recorded at a scan rate of 100 mV/s over a potential window from 0 V to -0.65 V (cathodic sweep), then to +0.5 V (anodic sweep), and finally back to -0.2 V.

3.5 Computational Experiments

DFT calculations were run using the Gaussian 16 software. (1) Optimization and frequency analysis were performed using the MN15 functional with the Def2TZVP basis set.(2-3) The method was selected for its reliable performance with transition metal complexes, as well as its favorable balance between computational efficiency and accuracy. The complexation energies were calculated across different substitutions of Fe-NHC complexes. Ground state structures were confirmed based on the lack of imaginary frequencies. Despite extensive efforts, the transition states involved in the interaction between the catalysts and substrates, where bromide insertion occurs, could not be identified. This can explain the equilibrium in the system, making it challenging to locate a transition state.

3.5.1 Optimized xyz-matrices and thermodynamic data for ($FeBr_3$)

Br	0.00000000	0.00000000	2.18236300
Br	0.00000000	-1.88049300	-1.09179300
Fe	0.00000000	0.00000000	0.00164600
Br	0.00000000	1.88049300	-1.09179300

Sum of electronic and zero-point Energies =-8987.3486 Hartree
Sum of electronic and thermal Energies =-8987.3427 Hartree
Sum of electronic and thermal Enthalpies =-8987.3418 Hartree
Sum of electronic and thermal Free Energies =-8987.3832 Hartree

3.5.2 Optimized xyz-matrices and thermodynamic data for (Fe-NHC-OMe)

N	-1.06671200	2.02692900	0.17810200
N	1.07108800	2.02472900	0.17796800
C	2.43259100	1.59339200	0.24423700
C	4.64179700	1.53715900	-0.69074500

C	4.13193300	0.29660700	1.31966900
C	5.04421200	0.68192900	0.33437200
H	5.32958200	1.83906300	-1.46753300
H	4.46712800	-0.37142800	2.10143600
C	-2.42883300	1.59732900	0.24501800
C	-4.13012500	0.30589000	1.32388800
C	-4.63627800	1.53620900	-0.69378700
C	-5.04056500	0.68616800	0.33482700
H	-4.46649800	-0.35858200	2.10818000
H	-5.32242300	1.83390700	-1.47364200
C	-2.82945700	0.76225600	1.28244700
H	-2.11093500	0.45624800	2.03355300
C	-3.32261100	1.98733200	-0.73379200
H	-2.98599700	2.61439400	-1.55067000
C	2.83118900	0.75278900	1.27793400
H	2.11164200	0.44371000	2.02681800
C	3.32820600	1.98841300	-0.73097000
H	2.99308400	2.62011800	-1.54490300
C	0.00126800	1.19804400	0.16245400
Fe	-0.00162000	-0.90651900	-0.10483400
Br	-0.00280300	-1.80044400	2.05034800
Br	1.88115200	-1.44844900	-1.34442700
Br	-1.88618900	-1.44558900	-1.34244500
O	-6.28890300	0.18753900	0.45213800
O	6.29235400	0.18255800	0.45133200
C	7.23288100	0.50064300	-0.54737400
H	8.15283500	-0.01305900	-0.28280000
H	6.89617100	0.15732700	-1.52967800
H	7.41986800	1.57794300	-0.58739400
C	-7.22735900	0.50000600	-0.55027300
H	-6.88860500	0.15124100	-1.52994200
H	-8.14784400	-0.01227400	-0.28478300
H	-7.41424000	1.57707000	-0.59668200
C	0.67897800	3.34820800	0.16815900

H	1.39358000	4.15182400	0.19549300
C	-0.67186100	3.34959700	0.16617000
H	-1.38487500	4.15464400	0.19288200

Sum of electronic and zero-point Energies = -9903.7903 Hartree

Sum of electronic and thermal Energies = -9903.7642 Hartree

Sum of electronic and thermal Enthalpies = -9903.7633 Hartree

Sum of electronic and thermal Free Energies = -9903.8534 Hartree

3.5.3 Optimized xyz-matrices and thermodynamic data for (NHC-OMe)

C	0.04395600	0.00008400	0.00043300
N	-1.06124400	0.79661700	0.00036900
N	1.06578800	0.90109100	0.00021700
C	2.43780500	0.51358500	0.00008500
C	4.78288900	1.07066600	-0.00061300
C	4.10415300	-1.23257100	0.00038800
C	5.12017000	-0.28037600	-0.00017600
H	5.57989400	1.80275000	-0.00106200
H	4.33146200	-2.28966400	0.00073600
C	-2.38825600	0.27672500	0.00016400
C	-4.78484900	0.59241000	-0.00017100
C	-3.86305500	-1.62543800	-0.00005200
C	-4.97672000	-0.78287700	-0.00020600
H	-5.62333700	1.27477500	-0.00028800
H	-4.02776900	-2.69525100	-0.00007800
C	-3.49173300	1.11312700	0.00001300
H	-3.37443300	2.18811900	0.00002000
C	-2.58613600	-1.10538200	0.00013300
H	-1.71858600	-1.75016300	0.00025200
C	2.77389800	-0.83254400	0.00051800
H	1.97653400	-1.56252800	0.00095700
C	3.45660400	1.46366600	-0.00049100
H	3.23158300	2.52131600	-0.00087400
O	6.44428200	-0.57434700	-0.00034100

O	-6.19128200	-1.38614900	-0.00037600
C	6.81408000	-1.93106500	0.00008300
H	7.90054100	-1.95930800	-0.00013400
H	6.44005000	-2.44510000	0.89091100
H	6.43967700	-2.44575800	-0.89020800
C	-7.33059300	-0.56301200	-0.00054400
H	-7.36197200	0.07246100	-0.89125700
H	-8.19431700	-1.22266000	-0.00067200
H	-7.36223500	0.07246100	0.89015900
C	-0.73456400	2.14686900	0.00077300
H	-1.45550800	2.94330500	0.00111300
C	0.60820500	2.21267300	0.00003800
H	1.24748900	3.07602400	-0.00019500

Sum of electronic and zero-point Energies = -916.27648 Hartree
Sum of electronic and thermal Energies = -916.26020 Hartree
Sum of electronic and thermal Enthalpies = -916.25926 Hartree
Sum of electronic and thermal Free Energies = -916.32068 Hartree

3.5.4 Optimized xyz-matrices and thermodynamic data for (Fe-NHC-H)

N	-1.06681600	2.06906000	0.14579600
N	1.06962400	2.06761000	0.14568500
C	2.43330300	1.64245600	0.21901700
C	4.64584000	1.62929100	-0.68370400
C	4.13046400	0.34473800	1.28876600
C	5.04244500	0.76126200	0.32732900
H	5.35421100	1.94541200	-1.43813000
H	4.43614600	-0.33498300	2.07288700
H	6.06388200	0.40534200	0.36164200
C	-2.43094600	1.64496500	0.21869700
C	-4.13004600	0.35104200	1.28999700
C	-4.64244400	1.63061100	-0.68649300
C	-5.04067800	0.76548500	0.32634900
H	-4.43696600	-0.32641100	2.07559400

H	-5.34967300	1.94506700	-1.44268100
H	-6.06238400	0.41032800	0.36052700
C	-2.81690200	0.79658000	1.24471000
H	-2.08777100	0.47373000	1.97823700
C	-3.32938200	2.07485900	-0.74566400
H	-2.99027300	2.71647100	-1.54995700
C	2.81760200	0.79110900	1.24316900
H	2.08753500	0.46684300	1.97515700
C	3.33310400	2.07436400	-0.74324100
H	2.99518200	2.71822000	-1.54624100
C	0.00084200	1.23901800	0.14671500
Fe	-0.00073800	-0.87140900	-0.11767100
Br	-0.00140900	-1.77490700	2.03351000
Br	-1.88231100	-1.40266200	-1.35952000
Br	1.88022900	-1.40196300	-1.36111300
C	0.67740000	3.39091100	0.10885500
H	1.39164400	4.19523600	0.12104800
C	-0.67289000	3.39184700	0.10881400
H	-1.38608500	4.19711000	0.12043200

Sum of electronic and zero-point Energies = -9674.9529 Hartree

Sum of electronic and thermal Energies = -9674.9321 Hartree

Sum of electronic and thermal Enthalpies = -9674.9311 Hartree

Sum of electronic and thermal Free Energies = -9675.0091 Hartree

3.5.5 Optimized xyz-matrices and thermodynamic data for (NHC-H)

C	0.00000300	-0.31894800	-0.00012300
N	-1.06490800	0.53103500	-0.00001100
N	1.06489500	0.53100800	-0.00005600
C	2.41460400	0.07575400	-0.00000300
C	4.78248500	0.51262600	0.00002800
C	3.98408400	-1.74538500	0.00008800
C	5.04698600	-0.84858400	0.00008000
H	5.59693000	1.22597200	0.00001800

H	4.17444400	-2.81130300	0.00012700
H	6.06791500	-1.20766900	0.00011200
C	-2.41462500	0.07578300	-0.00001900
C	-3.98402900	-1.74540800	-0.00004400
C	-4.78250300	0.51258400	0.00000700
C	-5.04695000	-0.84863400	-0.00001900
H	-4.17436700	-2.81132900	-0.00006400
H	-5.59698400	1.22589100	0.00002500
H	-6.06786900	-1.20774800	-0.00001800
C	-2.67458400	-1.29244200	-0.00004400
H	-1.83771300	-1.97626500	-0.00006400
C	-3.47303100	0.97775400	0.00000800
H	-3.29545500	2.04417600	0.00001700
C	2.67463100	-1.29246400	0.00004700
H	1.83778700	-1.97632300	0.00005100
C	3.47299800	0.97774100	-0.00001500
H	3.29538800	2.04416400	-0.00005900
C	0.67153400	1.86513700	-0.00020400
H	1.35215500	2.69608800	-0.00031700
C	-0.67158400	1.86515000	0.00024100
H	-1.35225600	2.69607100	0.00047500

Sum of electronic and zero-point Energies = -687.44200 Hartree
Sum of electronic and thermal Energies = -687.43089 Hartree
Sum of electronic and thermal Enthalpies = -687.42995 Hartree
Sum of electronic and thermal Free Energies = -687.47953 Hartree

3.5.6 Optimized xyz-matrices and thermodynamic data for (Fe-NHC-I)

N	1.06789500	2.04103100	-0.01081700
N	-1.06783500	2.04089600	-0.01087100
C	-2.43033400	1.61654400	-0.08603000
C	-4.64495100	1.59866300	0.82178900
C	-4.13037300	0.32495300	-1.16776700
C	-5.03616800	0.73992300	-0.19955700

H	-5.35530300	1.90789200	1.57671100
H	-4.44050800	-0.34708600	-1.95642600
C	2.43039300	1.61667400	-0.08599900
C	4.13031700	0.32488300	-1.16768000
C	4.64506700	1.59881400	0.82168500
C	5.03619000	0.73992900	-0.19956100
H	4.44040200	-0.34724300	-1.95628600
H	5.35545100	1.90810100	1.57655300
C	2.81879600	0.77242800	-1.11427000
H	2.09322600	0.44928200	-1.85129800
C	3.33127200	2.03900700	0.87906700
H	2.99793800	2.67677800	1.68869500
C	-2.81882000	0.77244100	-1.11436900
H	-2.09330900	0.44934400	-1.85147600
C	-3.33113800	2.03878000	0.87916000
H	-2.99772200	2.67639700	1.68887500
C	0.00008500	1.21105500	-0.01764300
Fe	0.00000500	-0.90321600	0.22910400
Br	-0.00005800	-1.76797200	-1.93666700
Br	-1.88387500	-1.44026600	1.46218400
Br	1.88391100	-1.43986300	1.46234100
I	7.00597300	0.06730700	-0.27611400
I	-7.00599600	0.06742200	-0.27606300
C	-0.67497900	3.36456800	0.03511600
H	-1.38834700	4.16975200	0.02786400
C	0.67488200	3.36465700	0.03509900
H	1.38815500	4.16992700	0.02799300

Sum of electronic and zero-point Energies = -10267.753 Hartree

Sum of electronic and thermal Energies = -10267.729 Hartree

Sum of electronic and thermal Enthalpies = -10267.728 Hartree

Sum of electronic and thermal Free Energies = -10267.818 Hartree

3.5.7 Optimized xyz-matrices and thermodynamic data for (NHC-I)

N	-1.06061500	1.21728900	0.00066800
N	1.06064100	1.21730500	-0.00055900
C	2.40870100	0.77202700	-0.00231000
C	4.73033600	1.12759600	-0.53109800
C	4.03181000	-0.91792100	0.53386000
C	5.03606000	-0.11423400	0.00617100
H	5.51012400	1.74791600	-0.95300300
H	4.27314500	-1.88638400	0.95211700
C	-2.40867900	0.77200100	0.00240200
C	-4.03170100	-0.91822500	-0.53321700
C	-4.73043900	1.12784900	0.53049000
C	-5.03606700	-0.11425900	-0.00617400
H	-4.27294800	-1.88691000	-0.95101400
H	-5.51030800	1.74841500	0.95188600
C	-2.71928300	-0.47351900	-0.53282300
H	-1.92024200	-1.07969000	-0.93750000
C	-3.41327400	1.56785200	0.53895000
H	-3.17324900	2.52215000	0.99015100
C	2.71939100	-0.47320200	0.53351500
H	1.92043200	-1.07916100	0.93867600
C	3.41317300	1.56759400	-0.53950900
H	3.17298300	2.52163600	-0.99117200
C	0.00002700	0.36163900	-0.00013400
I	-7.01219700	-0.78060800	-0.01850300
I	7.01218700	-0.78060000	0.01839300
C	-0.67209500	2.55312800	0.00164400
H	-1.36821600	3.37259300	-0.01993800
C	0.67210400	2.55313100	-0.00111800
H	1.36823500	3.37258200	0.02096100

Sum of electronic and zero-point Energies = -1280.2458 Hartree

Sum of electronic and thermal Energies = -1280.2297 Hartree

Sum of electronic and thermal Enthalpies = -1280.2287 Hartree

Sum of electronic and thermal Free Energies = -1280.2948 Hartree

3.5.8 Optimized xyz-matrices and thermodynamic data for (Fe-NHC-CN)

N	-1.06698100	2.04896600	0.10971800
N	1.06733100	2.04890800	0.10977000
C	2.42914800	1.62558300	0.18435000
C	4.64518200	1.63891300	-0.70954800
C	4.12144200	0.32203400	1.25523100
C	5.03981300	0.75961200	0.30070500
H	5.36501800	1.96193100	-1.44900800
H	4.43673300	-0.36234500	2.03062200
C	-2.42886400	1.62577800	0.18421100
C	-4.12140000	0.32270600	1.25525600
C	-4.64476500	1.63910700	-0.70997200
C	-5.03958600	0.76012600	0.30048800
H	-4.43690700	-0.36141700	2.03078500
H	-5.36450900	1.96197600	-1.44958400
C	-2.81047000	0.76358300	1.20121100
H	-2.07939300	0.42603800	1.92565000
C	-3.33228500	2.07375600	-0.76837700
H	-2.99868400	2.72522300	-1.56623800
C	2.81057300	0.76307200	1.20115400
H	2.07939900	0.42539200	1.92543600
C	3.33275000	2.07371200	-0.76799000
H	2.99936600	2.72541500	-1.56575000
C	0.00015600	1.21775800	0.11717200
Fe	0.00002400	-0.89806400	-0.15973600
Br	-0.00006100	-1.78348700	1.99402500
Br	1.88465000	-1.39897200	-1.40334000
Br	-1.88514200	-1.39983000	-1.40225800
C	-6.40219300	0.31141700	0.35801200
C	6.40236900	0.31077700	0.35826500
N	-7.49869100	-0.03907500	0.40567600

N	7.49884200	-0.03979400	0.40594900
C	-0.67428200	3.37393700	0.06291400
H	-1.38671400	4.17998600	0.07117700
C	0.67470500	3.37390300	0.06292800
H	1.38716200	4.17992800	0.07124000

Sum of electronic and zero-point Energies = -9859.2969 Hartree

Sum of electronic and thermal Energies = -9859.2724 Hartree

Sum of electronic and thermal Enthalpies = -9859.2714 Hartree

Sum of electronic and thermal Free Energies = -9859.3585 Hartree

3.5.9 Optimized xyz-matrices and thermodynamic data for (NHC-CN)

C	0.00000200	-0.04531800	0.00032900
N	-1.06435200	0.80561500	0.00025700
N	1.06435800	0.80558500	0.00026300
C	2.40785800	0.34690400	0.00016000
C	4.77450800	0.78270400	-0.00018200
C	3.96273100	-1.48580900	0.00020200
C	5.03163000	-0.58629700	-0.00003800
H	5.59945800	1.48237900	-0.00037400
H	4.16109200	-2.54930400	0.00031200
C	-2.40787700	0.34694100	0.00007100
C	-4.77453200	0.78270200	-0.00020300
C	-3.96271700	-1.48580100	-0.00017700
C	-5.03162700	-0.58629700	-0.00027800
H	-5.59949800	1.48235800	-0.00028200
H	-4.16107700	-2.54929600	-0.00023500
C	-3.46972300	1.24697900	-0.00002900
H	-3.29716800	2.31353600	0.00002000
C	-2.66100800	-1.02410000	-0.00000300
H	-1.82247700	-1.70531900	0.00007700
C	2.66101000	-1.02412900	0.00030100
H	1.82250300	-1.70537900	0.00048800
C	3.46969700	1.24695500	-0.00008500

H	3.29710700	2.31351000	-0.00021800
C	6.38282900	-1.06612000	-0.00013900
C	-6.38282100	-1.06614200	-0.00045600
N	7.46952200	-1.45096400	-0.00022000
N	-7.46950900	-1.45100000	-0.00060000
C	-0.67079900	2.14220800	0.00047000
H	-1.35059400	2.97378900	0.00058800
C	0.67081900	2.14217500	0.00029600
H	1.35063100	2.97374600	0.00029200

Sum of electronic and zero-point Energies = -872.97692 Hartree

Sum of electronic and thermal Energies = -871.77810 Hartree

Sum of electronic and thermal Enthalpies = -871.77715 Hartree

Sum of electronic and thermal Free Energies = -871.79287 Hartree

4. RESULTS AND DISCUSSION

4.1 Spesicification of Synthesized Intermediates

Iron-NHC catalysts synthesized by starting from commercial 2,6-diisopropyl aniline **(1)** starting material. For the aniline derivative precursors, (1) was first converted iodo compound, then, cyanation and metoxylation reactions realized in the presence of copper metal. After that, all aniline derivatives used to synthesize diimine compounds by reacting with glyoxal with a catalytic amount of formic acid. Finally, these diimine compounds converted to corresponding N-heterocyclic structure (NHC-H, NHC-CN, NHC-I, NHC-OMe) with HCl/paraformaldehyde as one carbon source by forming their electronically modified derivatives. After this point, to obtain the free carbene structures, all N-heterocyclic compounds reacted with KOtBu strong base in air free condition to observe their NMR spectrum and subsequently mixed with $FeBr_3$ salt to obtain the Fe-NHC metal catalysts. All these reaction products as indicated here specified by ^{1}H-NMR, ^{13}C-NMR, and HR-MS spectroscopy to confirm the structures.

4.1.1 Characterization of 2

As seen in Figure 4.1., 4.2., chemical shifts, integrations, and splitting patterns are correlated with the structure of the compound by showing a singlet peak at 7.30 ppm for aromatic proton(2H), a broad peak at 3.8 ppm for N-H protons (2H), a septet peak at 2.85 ppm for benzylic protons (2H), and a doublet peak at 1.25 ppm for isopropyl protons (12H). Also, number of the carbon and estimated chemical shift for ^{13}C NMR is well align with the titled compound.

4.1.2 Characterization of 3

As seen in Figure 4.3., 4.4., chemical shifts, integrations, and splitting patterns are correlated with the structure of the compound by showing a singlet peak at 7.32 ppm for aromatic protons (2H), a broad peak at 4.30 ppm for N-H protons (2H), a septet peak at 2.85 ppm for benzylic protons (2H), and a doublet peak at 1.25 ppm for isopropyl protons (12H). Also, number of the carbon and estimated chemical shift for

^{13}C NMR is well align with the titled compound. Characteristic CN carbon peak is seen at 100 ppm in the spectrum.

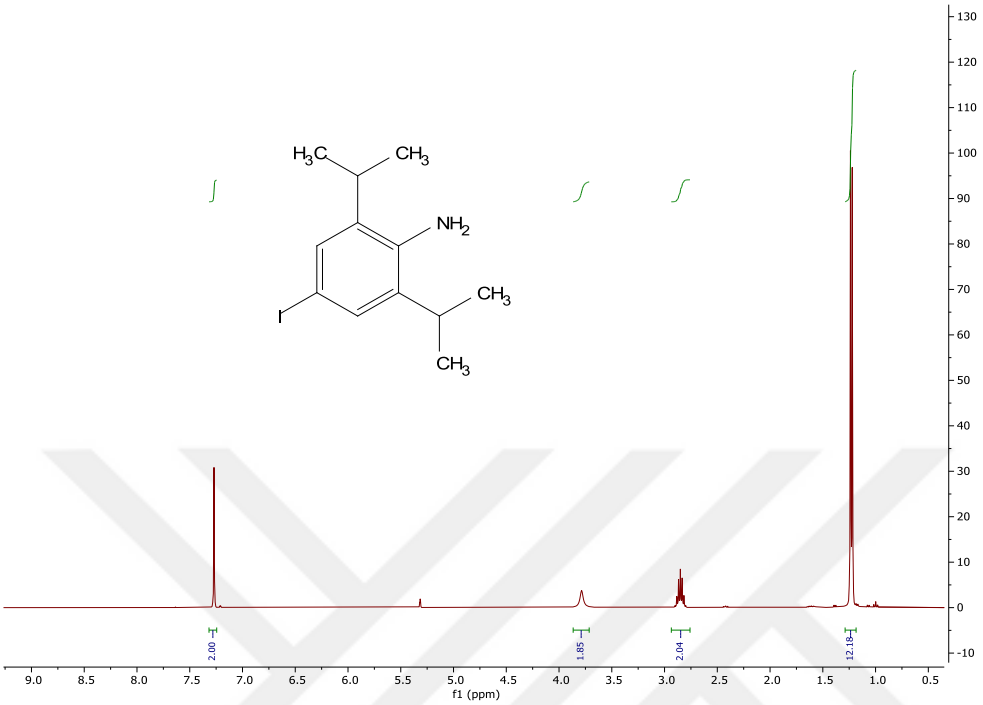

Figure 4.1 : ^{1}H NMR analysis of precursor 2.

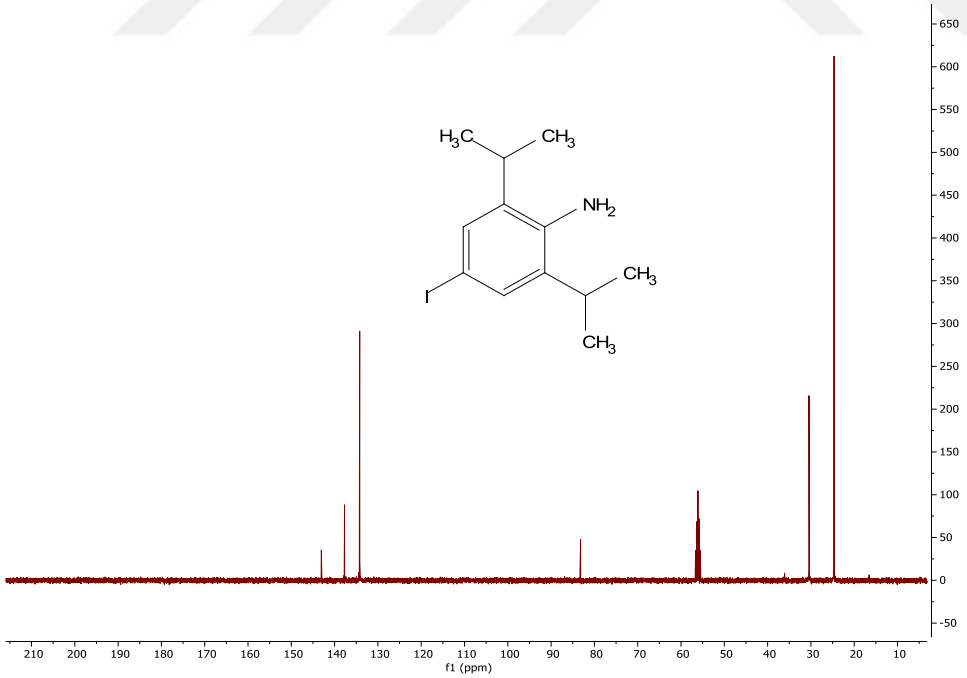

Figure 4.2 : ^{13}C NMR analysis of precursor 2.

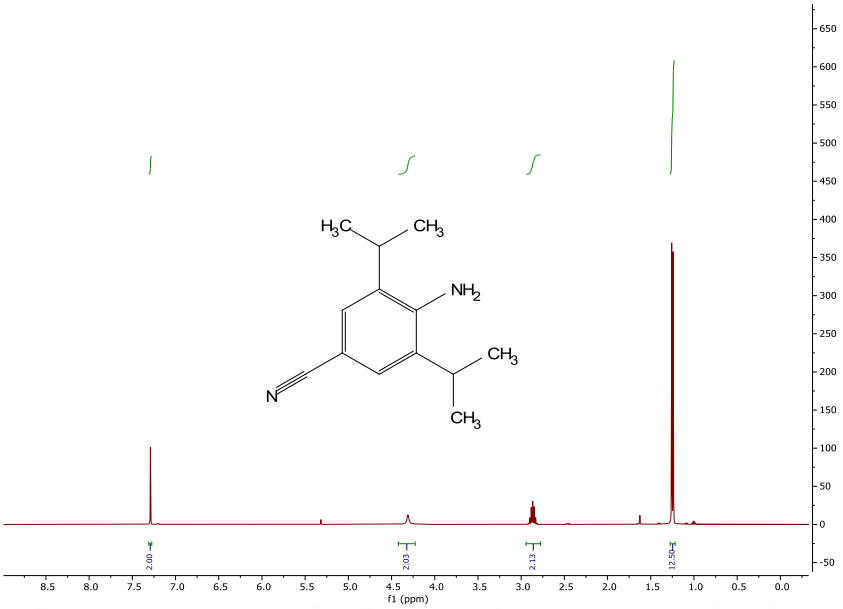

Figure 4.3 : ^{1}H NMR analysis of precursor 3.

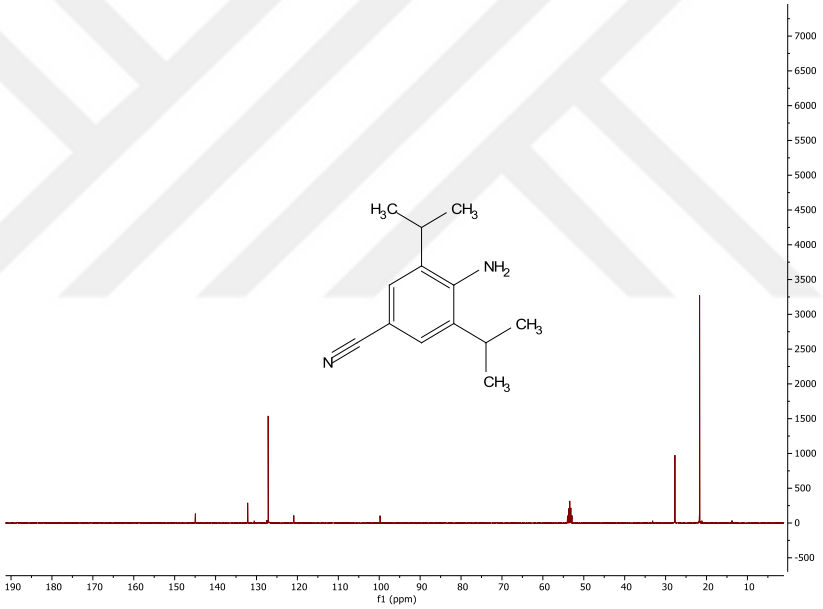

Figure 4.4 : ^{13}C NMR analysis of precursor 3.

4.1.3 Characterization of 4

As seen in Figure 4.5., 4.6., chemical shifts, integrations, and splitting patterns are correlated with the structure of the compound by showing a singlet peak at 6.58 ppm for aromatic protons (2H), a broad peak at 3.45 ppm for N-H protons (2H), a septet peak at 2.95 ppm for benzylic protons (2H), and a doublet peak at 1.25 ppm for isopropyl protons (12H). Also, number of the carbon and estimated chemical shift for ^{13}C NMR is well align with the titled compound. Characteristic methoxy carbon peak is seen at 56 ppm in the spectrum.

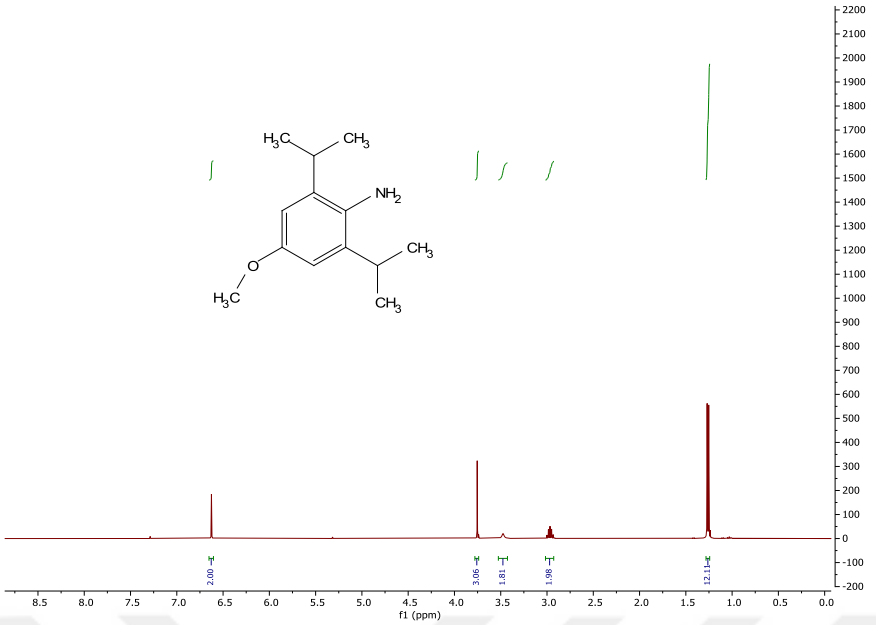

Figure 4.5 : ^{1}H NMR analysis of precursor 4.

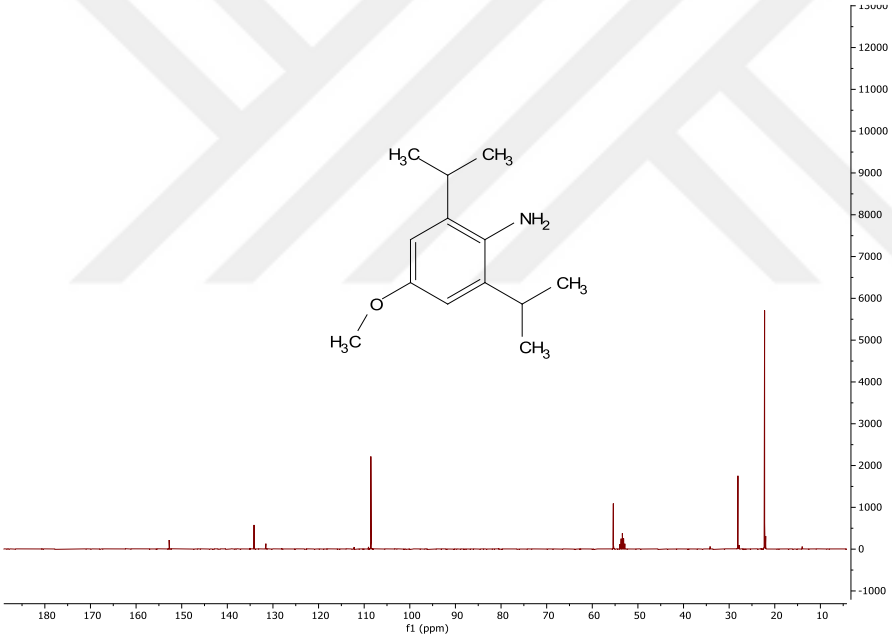

Figure 4.6 : ^{13}C NMR analysis of precursor 4.

4.1.4 Characterization of diimine-I

As seen in Figure 4.7., 4.8. chemical shifts, integrations, and splitting patterns are correlated with the structure of the compound by showing a singlet peak at 8.03 for imine protons (2H) a singlet peak at 7.50 ppm for aromatic protons (4H), a septet peak at 2.83 ppm for benzylic protons (4H), and a doublet peak at 1.20 ppm for isopropyl protons (24H). Also, number of the carbon and estimated chemical shift for ^{13}C NMR is well align with the titled compound. Characteristic imine carbon peak is seen at 166 ppm in the spectrum.

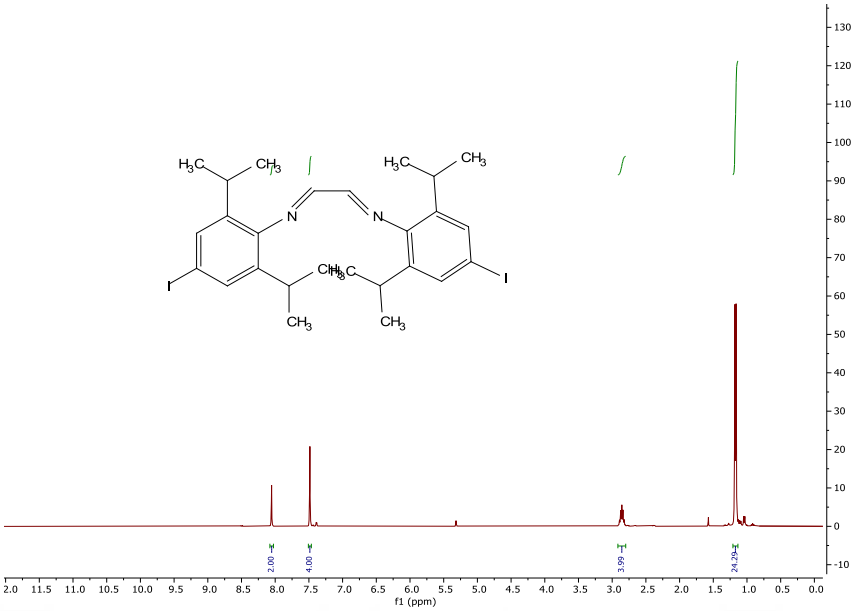

Figure 4.7 : ^{1}H NMR analysis of diimine-I.

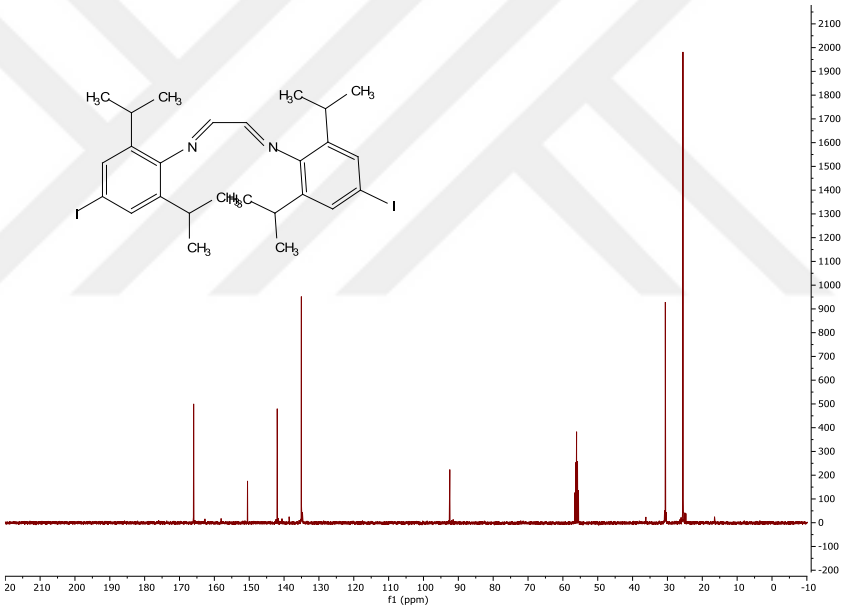

Figure 4.8 : ^{13}C NMR analysis of diimine-I.

4.1.5 Characterization of diimine-CN

As seen in Figure 4.9., 4.10. chemical shifts, integrations, and splitting patterns are correlated with the structure of the compound by showing a singlet peak at 8.10 for imine protons (2H) a singlet peak at 7.50 ppm for aromatic protons (4H), a septet peak at 2.92 ppm for benzylic protons (4H), and a doublet peak at 1.20 ppm for isopropyl protons (24H). Also, number of the carbon and estimated chemical shift for ^{13}C NMR is well align with the titled compound. Characteristic imine carbon peak is seen at 166 ppm in the spectrum.

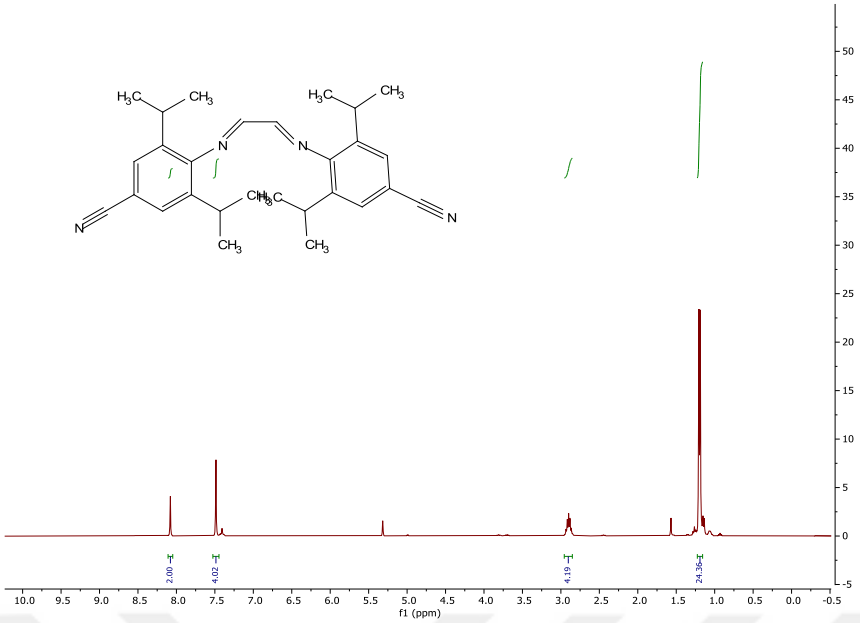

Figure 4.9 : ^{1}H NMR analysis of diimine-CN.

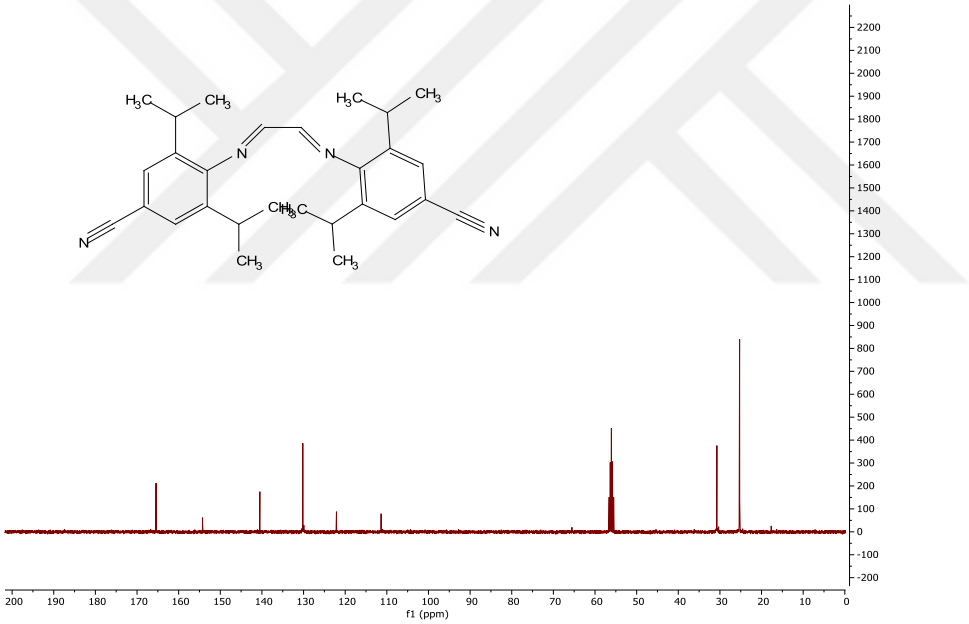

Figure 4.10 : ^{13}C NMR analysis of diimine-CN.

4.1.6 Characterization of diimine-OMe

As seen in Figure 4.11., 4.12. chemical shifts, integrations, and splitting patterns are correlated with the structure of the compound by showing a singlet peak at 8.05 for imine protons (2H) a singlet peak at 6.75 ppm for aromatic protons (4H), a septet peak at 2.98 ppm for benzylic protons (4H), and a doublet peak at 1.20 ppm for isopropyl protons (24H). Also, number of the carbon and estimated chemical shift for ^{13}C NMR is well align with the titled compound. Characteristic imine carbon peak is seen at 163 ppm and methoxy carbon peak at 55 ppm in the spectrum.

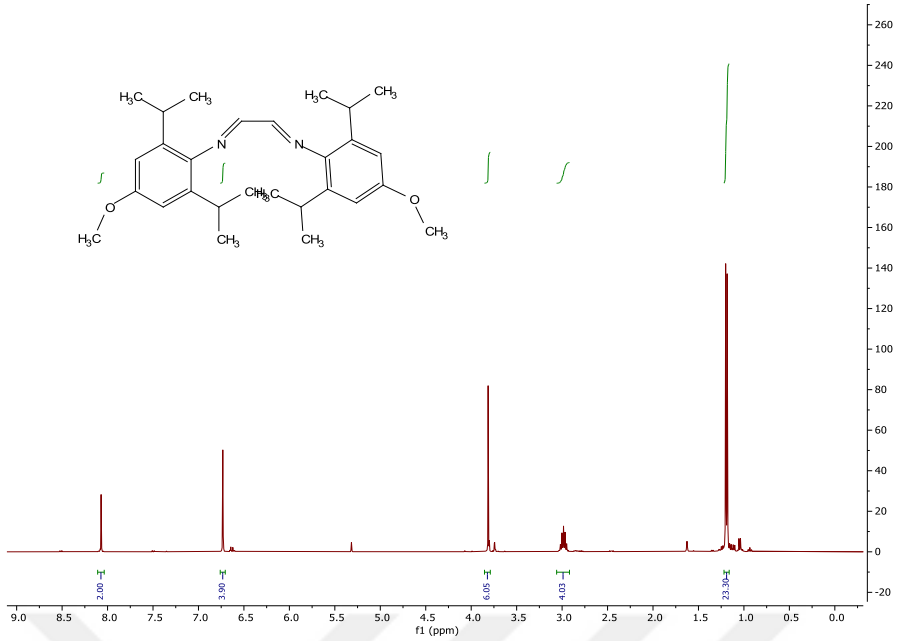

Figure 4.11 : ^{1}H NMR analysis of diimine-OMe.

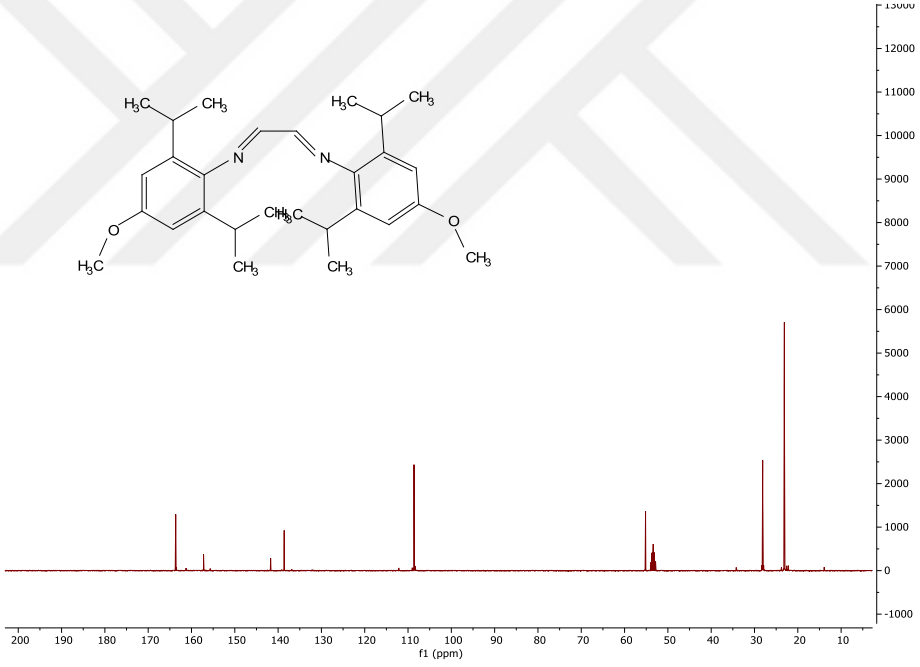

Figure 4.12 : ^{13}C NMR analysis of diimine-OMe.

4.1.7 Characterization of NHC-H

Figure 4.13. and 4.14. show ^{1}H and ^{13}C spectrums for NHC-H ligand. As seen in these spectrums one peak at 10.0 ppm is a characteristic C-2 imidazole ring proton (1H), a peak at 8.25 ppm is C-4,5 imidazole backbone protons (2H), two peaks at 7.65 ppm (2H) and 7.50 ppm (4H) are the aromatic proton peaks of the compound. On the other hand, benzylic protons appear at 2.48 ppm (4H) and isopropyl protons at 1.25 ppm (24H). Also, number of the carbon and estimated chemical shift for ^{13}C NMR is well

align with the titled compound. Characteristic C-2 carbon peak is seen at 142 ppm and in the spectrum.

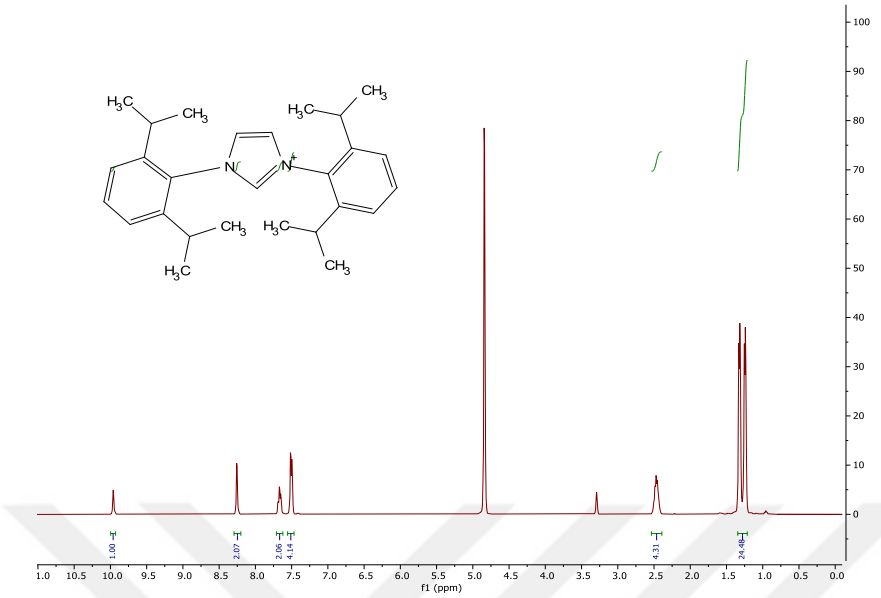

Figure 4.13 : ^{1}H NMR analysis of NHC-H.

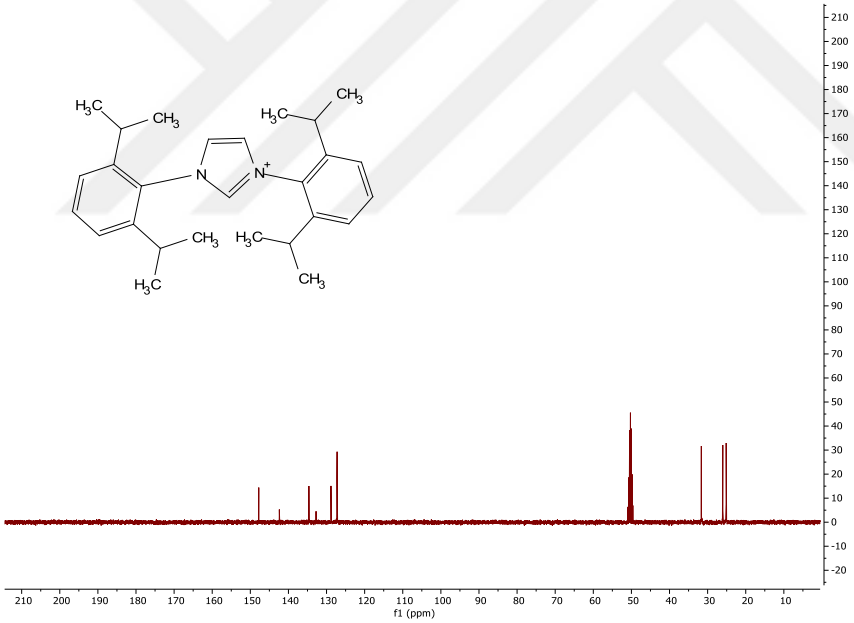

Figure 4.14 : ^{13}C NMR analysis of NHC-H.

4.1.8 Characterization of NHC-I

Figure 4.15. and 4.16. show ^{1}H and ^{13}C spectrums for NHC-I ligand. As seen in these spectrums one peak at 10.1 ppm is a characteristic C-2 imidazole ring proton (1H), a peak at 8.30 ppm is C-4,5 imidazole backbone protons (2H), one peak at 7.83 ppm (4H) is aromatic proton peak of the compound. On the other hand, benzylic protons appear at 2.37 ppm (4H) and isopropyl protons at 1.25 ppm (24H). Also, number of

the carbon and estimated chemical shift for ^{13}C NMR is well align with the titled compound. Characteristic C-2 carbon peak is seen at 142 ppm and in the spectrum.

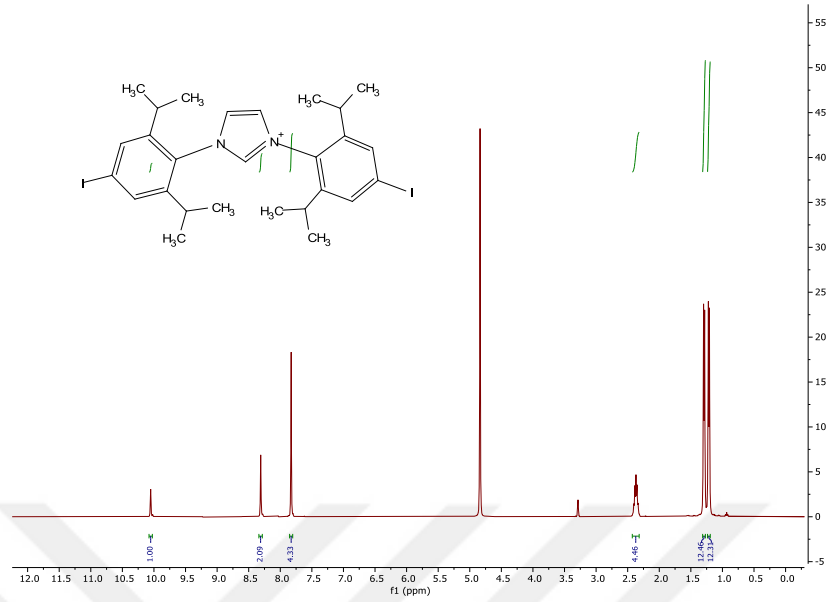

Figure 4.15 : ^{1}H NMR analysis of NHC-I.

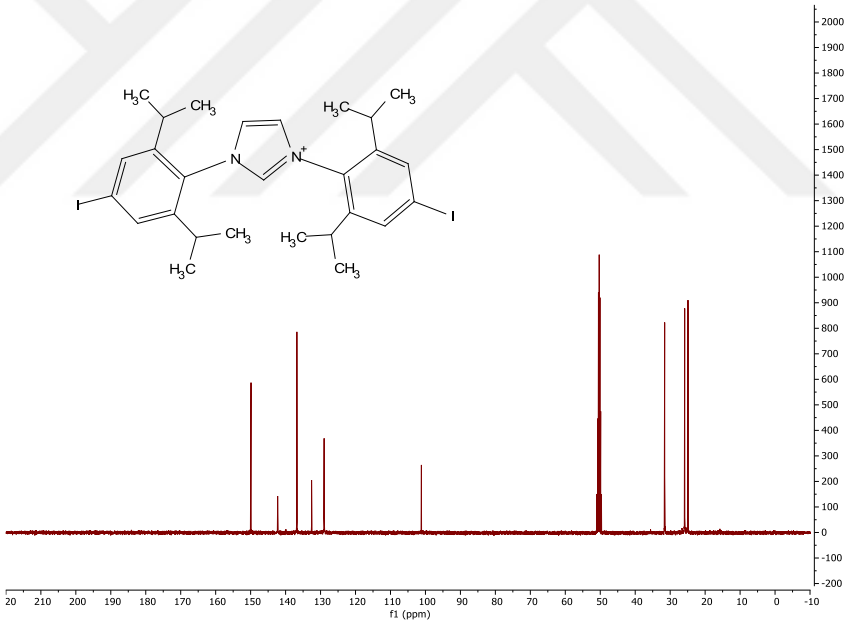

Figure 4.16 : ^{13}C NMR analysis of NHC-I.

4.1.9 Characterization of NHC-CN

Figure 4.17. and 4.18. show ^{1}H and ^{13}C spectrums for NHC-CN ligand. As seen in these spectrums one peak at 10.2 ppm is a characteristic C-2 imidazole ring proton (1H), a peak at 8.45 ppm is C-4,5 imidazole backbone protons (2H), one peak at 7.95 ppm (4H) is aromatic proton peak of the compound. On the other hand, benzylic

protons appear at 2.48 ppm (4H) and isopropyl protons at 1.29 ppm (24H). Also, number of the carbon and estimated chemical shift for ^{13}C NMR is well align with the titled compound. Characteristic C-2 carbon peak is seen at 142 ppm and in the spectrum.

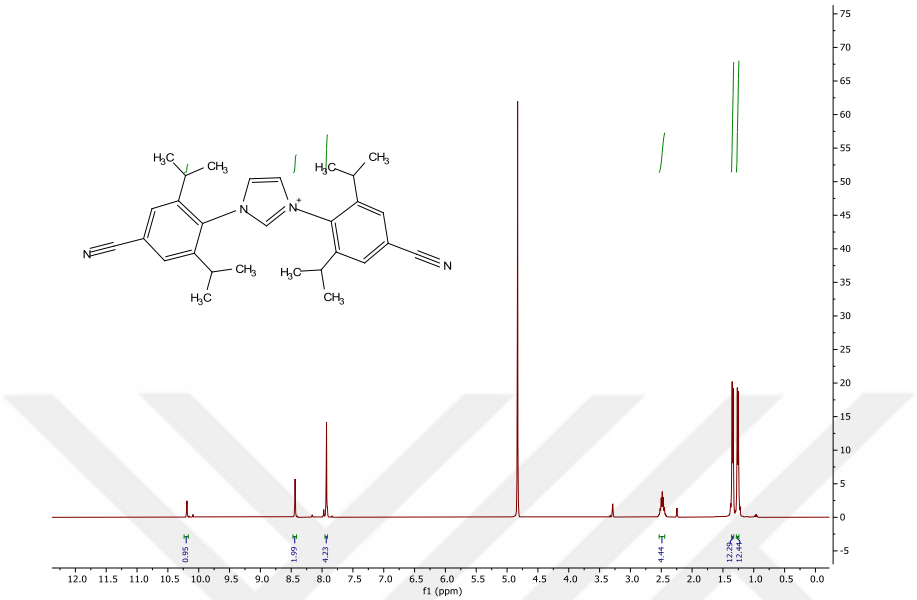

Figure 4.17 : ^{1}H NMR analysis of NHC-CN.

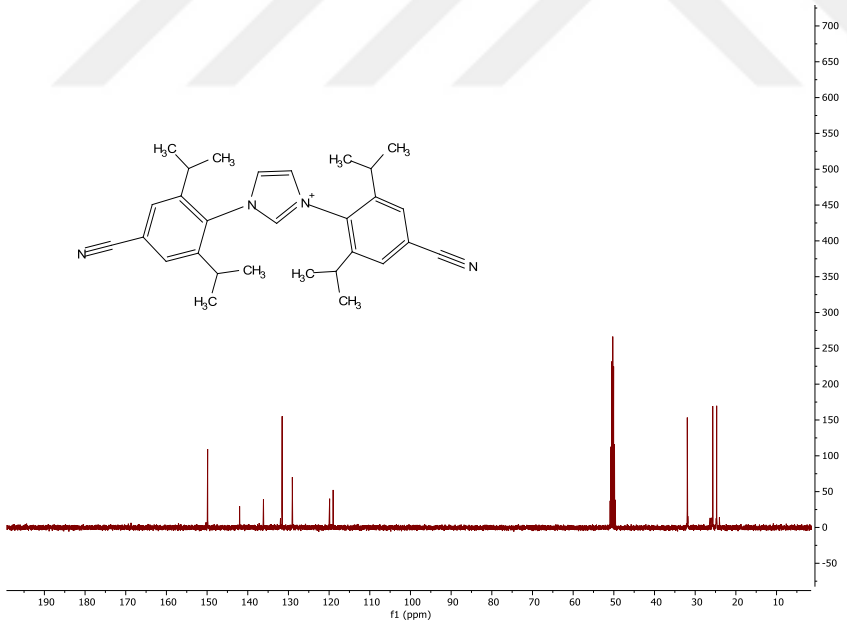

Figure 4.18 : ^{13}C NMR analysis of NHC-CN.

4.1.10 Characterization of NHC-OMe

Figure 4.19. and 4.20. show ^{1}H and ^{13}C spectrums for NHC-OMe ligand. As seen in these spectrums one peak at 10.65 ppm is a characteristic C-2 imidazole ring proton (1H), a peak at 7.75 ppm is C-4,5 imidazole backbone protons (2H), one peak at 6.75

ppm (4H) is aromatic proton peak of the compound. On the other hand, benzylic protons appear at 2.33 ppm (4H) and isopropyl protons at 1.23 ppm (24H). Also, number of the carbon and estimated chemical shift for ^{13}C NMR is well align with the titled compound. Characteristic C-2 carbon peak is seen at 140 ppm and in the spectrum.

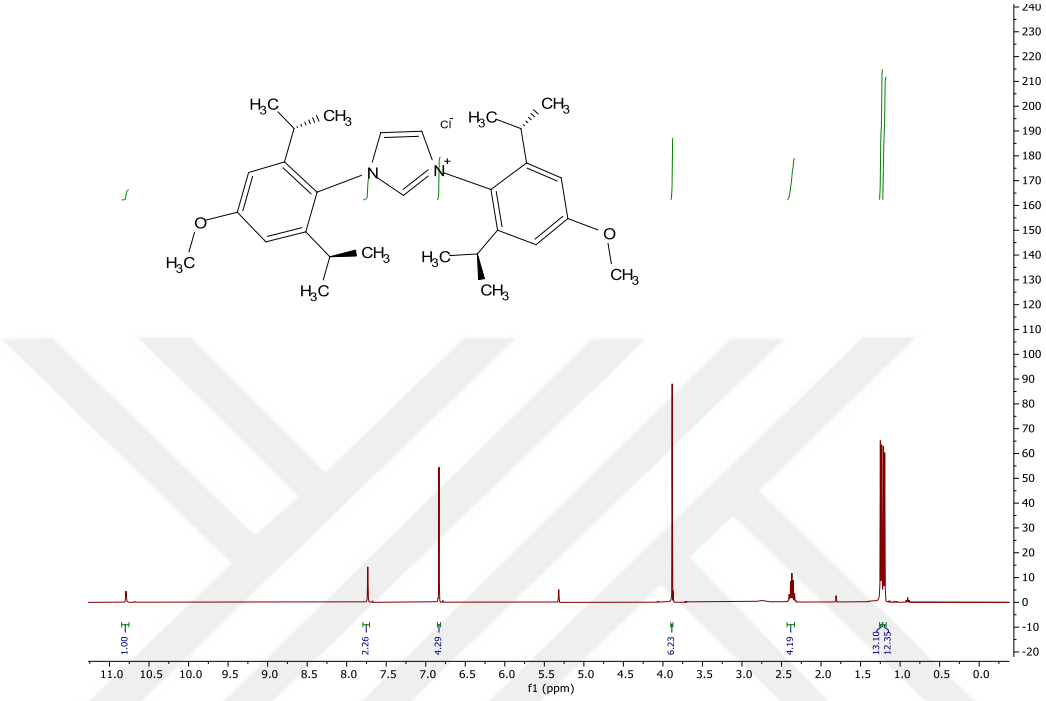

Figure 4.19 : ^{1}H NMR analysis of NHC-OMe.

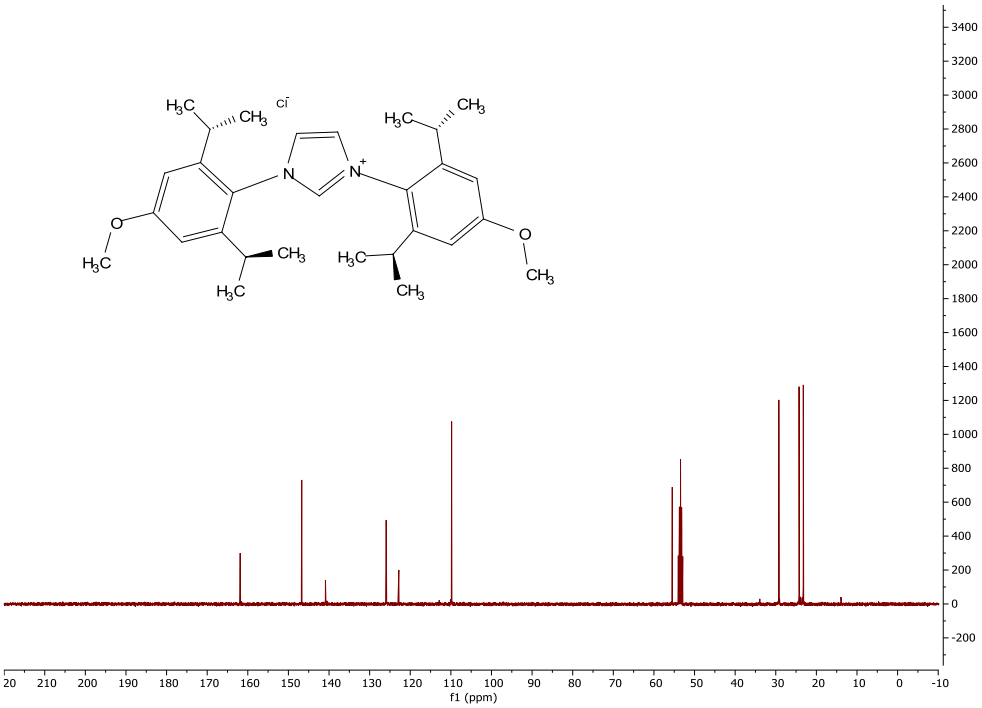

Figure 4.20 : ^{13}C NMR analysis of NHC-OMe.

4.2 Fe-NHC Catalyst`s Characterization To Infer Polymerization Activity

4.2.1 ^{13}C-NMR of free carbene

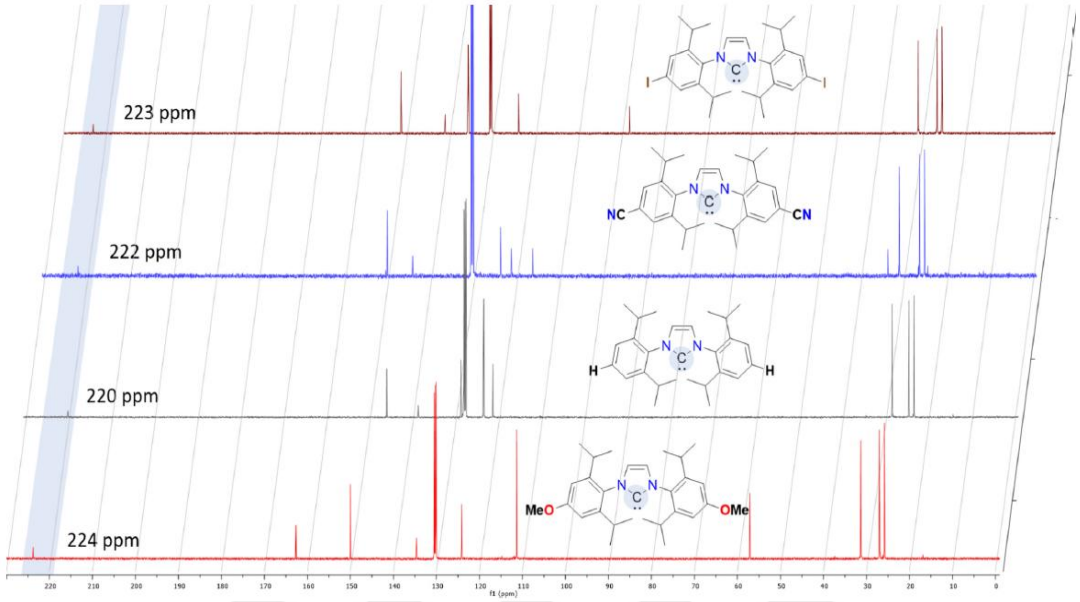

Figure 4.21 : ^{13}C-NMR of free carbene ligands.

Because the iron complexes are paramagnetic, NMR characterization was restricted to the free NHC ligands rather than their metal-bound forms. Within the NHC framework, the carbene carbon is electron-deficient and contains a vacant π-orbital that can accept electron density from the neighboring nitrogen atoms' lone pairs, thereby enhancing molecular stability. This electronic arrangement gives rise to a distinct downfield resonance in the ^{13}C NMR range, where carbene carbon (C-2) signals chracteristically appear between 190 and 240 ppm. Generally, a larger downfield shift indicates stronger σ-donation capability of the carbene carbon toward the corresponding catalytic metal center.

Therefore, as illustrated in Figure 4.21., the recorded ^{13}C NMR spectra revealed that NHC-OMe exhibited the most pronounced downfield signal at 223.80 ppm, followed sequentially by NHC-I (222.75 ppm), NHC-CN (222.00 ppm), and NHC-H (220.03 ppm). These data suggest that the methoxy-substituted carbene acts as the strongest electron donor to the iron center. Conversely, ligands bearing less donating substituents display progressively upfield shifts. The most notable upfield resonance was observed for NHC-H, which is likely attributed to differences in ligand geometry and N–C–N bond angles. Furthermore, variations in the N–C–N bond angle among

differently substituted NHCs can influence their NMR chemical shifts, occasionally complicating interpretation of the electron density at the metal site[9, 65].

4.2.2 Computational analysis of the catalysts

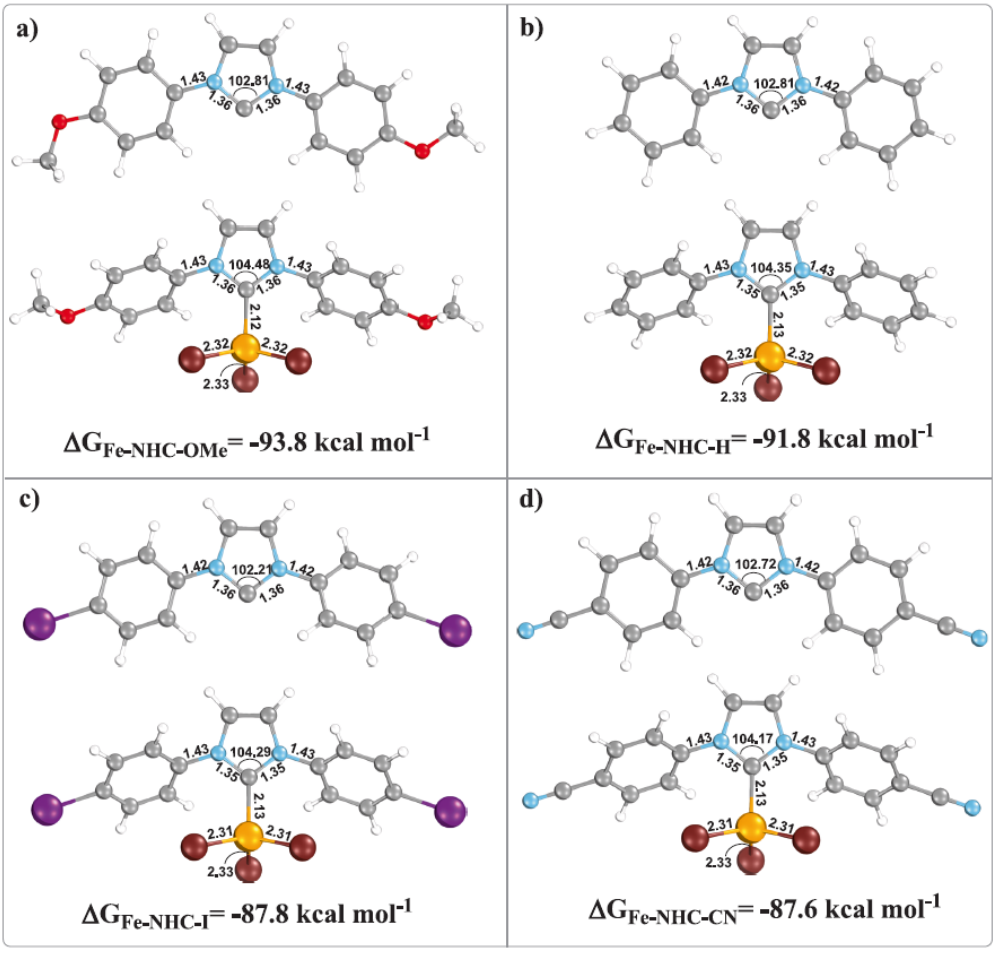

Figure 4.22 : 3D calculated structure of a) FeNHC-OMe, b) FeNHC-H, c) FeNHC-I, and d) FeNHC-CN catalysts.

A comprehensive set of density functional theory experiments was realized to comprehend and also quantify not only the thermodynamic stability but also geometrical characteristics of the synthesized FeNHC catalysts, as well as to elucidate the influence of ligand substituents. Upon coordination to the Fe–bromide center, the initially planar NHC framework adopts a slightly distorted configuration, as illustrated in Figure 4.22. The computed complexation energies for the methoxy-, hydrogen-, iodide-, and nitrile-substituted derivatives were –93.8, –91.8, –87.8, and –87.6 kcal mol^{-1}, respectively. Among these, the methoxy-substituted complex exhibited the greatest thermodynamic stability, which can be devoted to its resonance delocalization and more densely electron donation capability. In addition, the N–C–N bond angle

expanded gradually with increasing complex stability. The methoxy derivative showed a bond angle about 0.31° wider than that of the nitrile analogue. This systematic difference, clearly visible in the calculated structures (Figure 4.22), highlights how electronic substituent effects directly influence both geometry and bonding in Fe–NHC complexes.

4.2.3 Electrochemical analysis of the catalysts

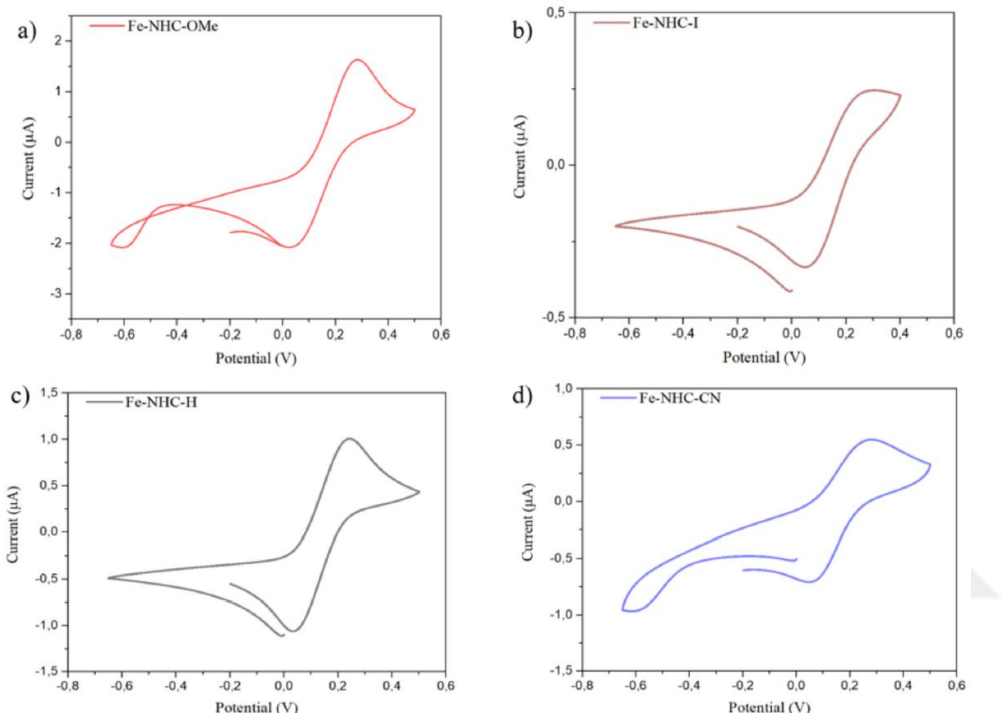

Figure 4.23 : Cyclic voltammogram of a) FeNHC-OMe, b) FeNHC-I, c) FeNHC-H, and d) FeNHC-CN complexes.

The cyclic voltammetry (CV) data for the four complexes are summarized in Figure 4.23 and Table 1, which report anodic peak (Epa), cathodic peak (Epc), and half-wave ($E_{1/2}$) potentials referenced to the Fc/Fc^+ couple. Measurements were performed in rigorously dried and degassed CH_2Cl_2 dissolved 0.2 M Bu_4NPF_6 under inert argon atmosphere. Each CV was recorded at 100 mV s^{-1}, beginning at 0 V, sweeping cathodically to –0.65 V, then anodically to +0.50 V, and finally returning to –0.20 V. A boron doped diamond working electrode was employed, with silver wire as the reference and Pt as the counter electrode; ferrocene served as an external standard. This solvent/electrolyte/electrode set-up was chosen to minimize ligand substitution at the Fe center during measurement. Across the series, the Fe complexes display quasi-reversible redox profiles with slow electron-transfer kinetics, evidenced by ΔEp values

that are substantially bigger than the 59 mV known for an ideal Nernstian couple. This type of quasi-reversible behavior matches catalysts that can alternate between Fe(II) and Fe(III). It maintains the activation–deactivation balance required for controlled ATRP[66].

In ATRP, the half-wave potential ($E_{1/2}$) correlates with the ATRP equilibrium constant (K_ATRP). It exhibites the reducing strength of the catalyst and mainly influences the activation rate (k_act). However, achieving low dispersity (Đ) also requires fast deactivation (k_deact) to limit the lifetime of propagating radicals[67]. Therefore, interpreting voltammetry in terms of both activation and deactivation is essential. Within this context, a more positive E_pa means that the oxidation from Fe^{+2} to Fe^{+3} is thermodynamically less favorable. In this case, the resulting Fe(III) species is thus more oxidizing but less stable. Such characteristics usually promote faster deactivation (higher k_deact) and tighter control (lower Đ). Yet, the trend is not entirely straightforward. The best-performing complex, Fe–NHC–OMe, shows the most positive E_pa but not the most positive E_pc. As a result, it displays a larger potential gap (ΔE_p), as seen in Figure 4.23 and Table 4.1.

Table 4.1 : Cyclic voltammogram data of the complexes.

Complex	***E*pa (V)**	***E*pc (V)**	**Δ*E*p (V)**	***E*1/2 (V)**	**Fc/Fc+ (V)**
FeNHC-H	0.243	0.039	0.204	0.141	−0.259
FeNHC-OMe	0.283	0.029	0.254	0.156	−0.244
FeNHC-CN	0.272	0.06	0.212	0.166	−0.234
FeNHC-I	0.256	0.058	0.198	0.157	−0.243

This observation indicates that peak positions are influenced by both thermodynamic driving forces and kinetic constraints at the electrode. The enlarged ΔE_p suggests the presence of significant kinetic barriers to electron transfer, which reduce the diagnostic value of E_pc when considered alone. Thus, the superior polymerization control observed for Fe–NHC–OMe—despite having an $E_{1/2}$ similar to Fe–NHC–I—is best explained by its more positive E_pa. This indicates a stronger Fe(III) deactivator and a more balanced activation–deactivation regime in solution. Overall, evaluating both E_pa (reflecting deactivator strength) and ΔE_p (reflecting kinetic effects) provides a more accurate prediction of ATRP performance than relying on $E_{1/2}$ alone.

4.3 Polymerization Studies

4.3.1 Styrene and MMA polymerization

Incorporating Fe–NHC catalysts into the free radical polymerization reactions which is a control experiment to test the catalysts in polar methyl methacrylate (MMA) and styrene monomers significantly improved the control of both reactions. A clear reduction in dispersity (Đ) was observed—from 1.70 to 1.33 for PMMA, and from 1.61 to 1.20 for PS—demonstrating a significant improvement in polymerization regulation (Figure 4.24 (a-d)). The [Monomer]:[Catalyst] ratio for ICAR-ATRP was initially selected in accordance with established literature protocols and gel permeation chromatography (GPC) confirmed effective control for MMA under these conditions[68, 69].

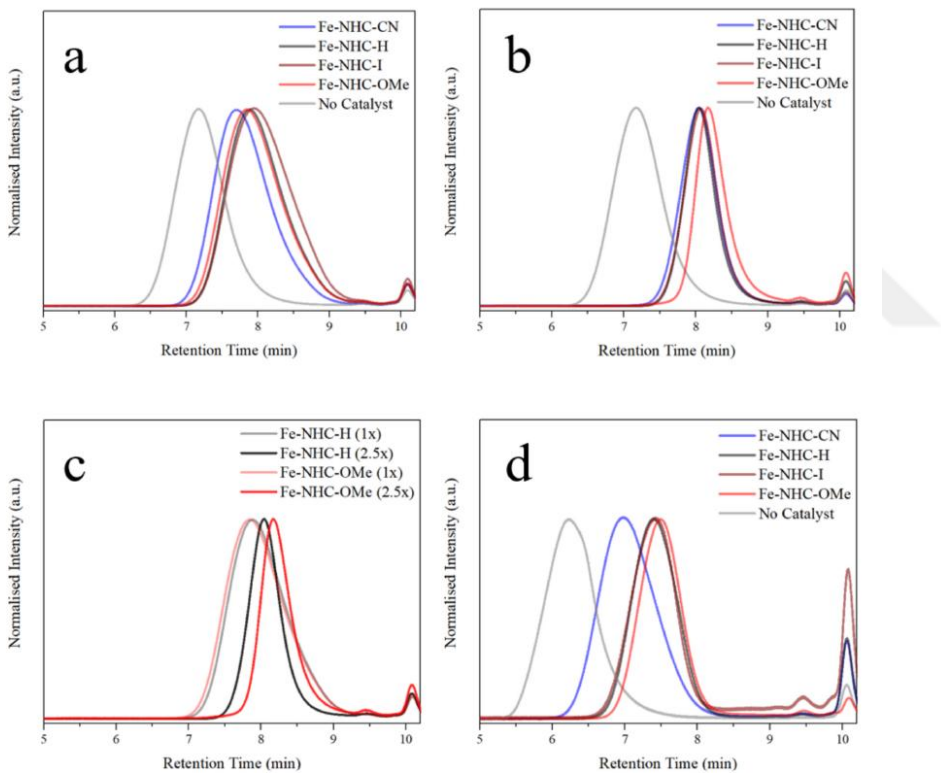

Figure 4.24 : GPC graphs of a) ICAR-ATRP of styrene monomer with the ratio of [Monomer]:[EBIB]:[Catalyst]:[AIBN] = 200:1:0.010:0.2 in 5 mL of solvent at 85 ◦C, b) ICAR-ATRP of styrene monomer with the ratio of [Monomer]:[EBIB]:[Catalyst]:[AIBN] = 200:1:0.025:0.2 in 5 mL of solvent at 85 ◦C c) ICAR-ATRP of styrene monomer with different catalysts concentrations d) ICAR-ATRP of MMA monomer with the ratio of [Monomer]:[EBIB]:[Catalyst]:[AIBN] = 200:1:0.01:0.2 in 5 mL of solvent at 60 ◦C.

However, when the same conditions were applied to styrene, the process displayed less efficient control, motivating an examination of the catalyst loading effect. Upon increasing the catalyst concentration by 2.5-fold and 5-fold, the polymerization

exhibited markedly narrower dispersities, reaching values below 1.20 as shown in Tables 4.2 and 4.3 and Figure 4.24. (c).

Table 4.2 : The synthesized PS polymers data by ICAR-ATRP.

Catalyst	Monomer	Time (h)	Conversion (%)	*Theorotical Mn* (kDa)	*Mn* (kDa)	*Đ*
No Catalyst	Styrene	2	25	5.4	45.2	1.61
FeNHC-H[a]	Styrene	2	17	3.7	9.1	1.8
FeNHC-H[a]	Styrene	6	~60	12.7	14.4	1.44
FeNHC-H[a]	Styrene	24	>95	20	50.7	1.79
FeNHC-H[b]	Styrene	2	15	3.3	12.2	1.24
FeNHC-CN[a]	Styrene	2	17	3.7	12.9	1.81
FeNHC-CN[b]	Styrene	2	19	4.2	13	1.28
FeNHC-I[a]	Styrene	2	16	3.5	8	1.87
FeNHC-I[b]	Styrene	2	18	3.9	12	1.24
FeNHC-I[b]	Styrene	5	~40	8.5	19.8	1.28
FeNHC-OMe[a]	Styrene	2	18	3.9	10	1.8
FeNHC-OMe[b]	Styrene	2	21	4.6	10	1.2
FeNHC-OMe[c]	Styrene	2	8	1.9	1.8	1.17

a- [Styrene]:[EBIB]:[Catalyst]:[AIBN] = 200:1:0.010:0.2 in 5 mL of anisole at 85 °C.
b- [Styrene]:[EBIB]:[Catalyst]:[AIBN] = 200:1:0.025:0.2 in 5 mL of anisole at 85 °C.
c- [Styrene]:[EBIB]:[Catalyst]:[AIBN] = 200:1:0.050:0.2 in 5 mL of anisole at 85 °C.

In contrast, MMA polymerization posed greater challenges due to its intrinsically faster propagation rate in ATRP, which demands catalysts of higher oxidative strength to sustain equilibrium. To moderate the rate and prevent uncontrolled chain growth, polymerizations were conducted at 60 °C, a substantially lower temperature than that used for styrene. Increasing the catalyst amount near to 2.5 times effectively promoted chain deactivation, reducing polymerization rate to the extent that no precipitable product formed within the first 2 hours. Under the original catalyst loading, only three complexes achieved Đ < 1.40, which represents the practical boundary for a well-controlled ATRP.

Table 4.3 : The synthesized PMMA polymers data by ICAR-ATRP.

Catalyst	Monomer	Time (h)	Conversion (%)	*Theorotical Mn* (kDa)	*Mn* (kDa)	*Đ*
No Catalyst	MMA	2	15	3.2	258.1	1.7
FeNHC-H[a]	MMA	2	5	1.2	34	1.38
FeNHC-H[a]	MMA	24	>95	19.2	354.4	1.95
FeNHC-H[b]	MMA	24	>95	19.2	80	1.65
FeNHC-CN[a]	MMA	2	6	1.4	60.5	1.67
FeNHC-I[a]	MMA	2	11	2.2	37	1.33
FeNHC-OMe[a]	MMA	2	6	1.4	30.1	1.33
FeNHC-OMe[b]	MMA	2	n.d.	n.d.	n.d.	n.d.
FeNHC-OMe[b]	MMA	6	19	3.8	13.5	1.4

a- [MMA]:[EBIB]:[Catalyst]:[AIBN] = 200:1:0.010:0.2 in 5 mL of anisole at 60 °C.

b- [MMA]:[EBIB]:[Catalyst]:[AIBN] = 200:1:0.025:0.2 in 5 mL of anisole at 60 °C.

Nevertheless, after 6 hours at elevated catalyst concentration, solid polymer formation was obtained with Đ ≈ 1.4 and high monomer conversion, confirming that enhanced deactivation dynamics contribute directly to the improved control of MMA polymerization (Figure 4.24. (d)).

4.3.2 Polymerization kinetics

The kinetic behavior of the ICAR-ATRP system was examined for styrene polymerization using the FeNHC-OMe catalyst at various concentrations. The experimental outcomes, presented in Table 4.4 and Figure 4.25., clearly demonstrate a well-controlled polymerization process, as reflected by the progressive increase in Mn with reaction time and the consistently narrow dispersity (Đ ≈ 1.15) observed at elevated catalyst loadings.

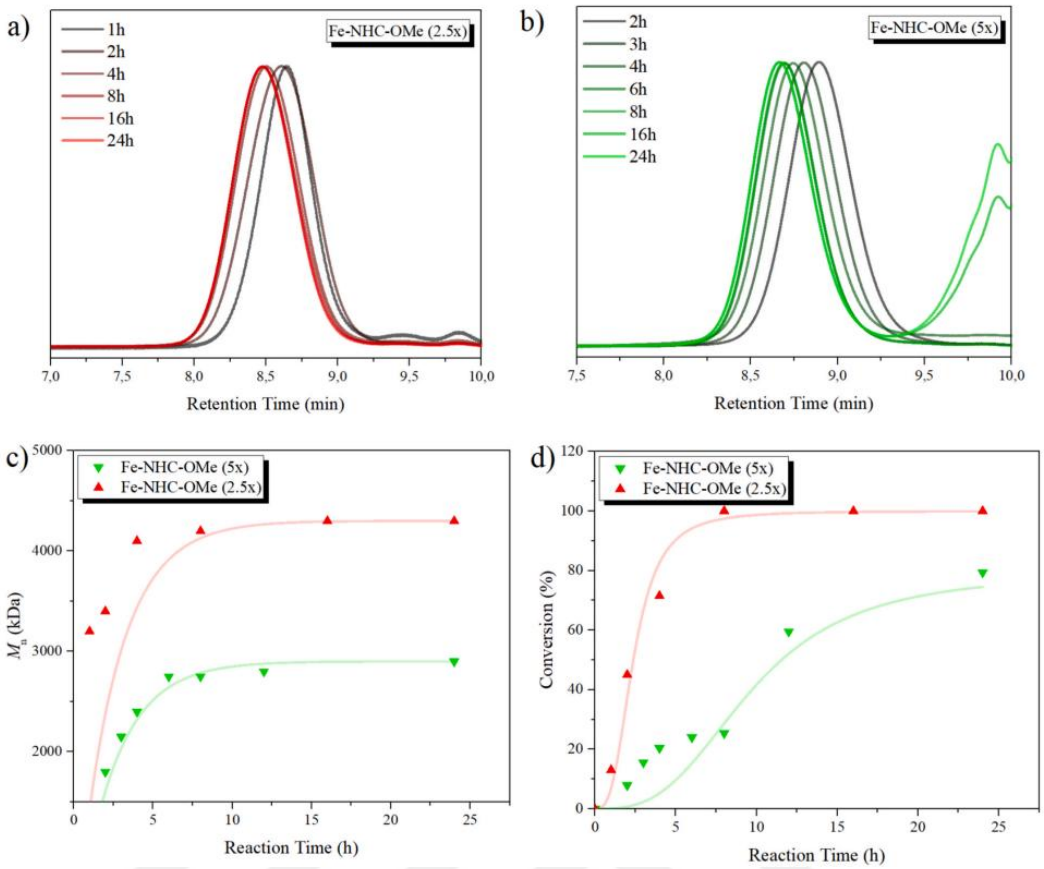

Figure 4.25 : GPC graphs of a) PS-Br polymer in the presence of 2.5 fold FeNHC-OMe, b) in the presence of 5 fold FeNHC-OMe, c) Mn analysis against time, and d) monomer conversion.

Over time graph derived from GPC, using the samples taken in-situ from ICAR-ATRP of styrene monomer with the ratio of [Monomer]:[EBIB]:[Catalyst]:[AIBN] = 200:1:0.025:0.2 in 5 mL of solvent at 85 ◦C.

A noticeable discrepancy was occured for the experimental and theoretical molecular weights (Mn), where the experimental values remained systematically lower as the reaction progressed. This deviation suggests the occurrence of additional initiation events beyond the expected stoichiometric initiation. Such behavior may arise from either (i) direct initiation of free-radical polymerization by 2-cyano-2-propyl radicals formed via AIBN decomposition, or (ii) the formation of 2-bromo-2-cyano-2-methyl ethane, generated through oxidation of the same radical species, which can also act as a secondary initiator during polymer growth.

Table 4.4 : The synthesized PS polymers for kinetics experiments using in-situ sampling and FeNHC-OMe as the catalyst.

Catalyst	Time (h)	Conversion (%)	*Theorotical Mn* (kDa)	*Mn* (kDa)	*Đ*
FeNHC-OMe[a]	1	13	2.9	3200	1.14
FeNHC-OMe[a]	2	45	9.5	3400	1.21
FeNHC-OMe[a]	4	72	15.2	4100	1.19
FeNHC-OMe[a]	8	>95	20.7	4200	1.2
FeNHC-OMe[a]	16	>95	20.7	4300	1.19
FeNHC-OMe[a]	24	>95	20.7	4300	1.19
FeNHC-OMe[b]	2	8	1.9	1.8	1.17
FeNHC-OMe[b]	3	16	3.4	2.1	1.17
FeNHC-OMe[b]	4	21	4.5	2.4	1.16
FeNHC-OMe[b]	6	24	5.2	2.7	1.14
FeNHC-OMe[b]	8	25	5.5	2.7	1.14
FeNHC-OMe[b]	12	59	12.6	2.8	1.16
FeNHC-OMe[b]	24	79	16.7	2.9	1.17

a- [Styrene]:[EBIB]:[Catalyst]:[AIBN] = 200:1:0.025:0.2 in 5 mL of anisol at 85 °C.

b- [Styrene]:[EBIB]:[Catalyst]:[AIBN] = 200:1:0.050:0.2 in 5 mL of anisol at 85 °C.

Importantly, this deviation was only observed in experiments by taking sample as in-situ. When polymerizations were performed in completely sealed systems without intermediate sampling, the relationship between theoretical and experimental Mn values reversed, strongly implying that the deviation originated from the sampling method. The most plausible explanation is the introduction of trace oxygen into the reaction mixture. At 85 °C, even minute amounts of oxygen can promote a degenerative chain-transfer mechanism: propagating radicals react with O_2 to yield peroxyl radicals, which—though poor initiators—can abstract hydrogen atoms from either solvent or polymer chains, thereby terminating one chain while initiating a new one. This side reaction increases the total number of polymer chains, resulting in a lower average Mn. However, the dispersity (Đ) remains controlled because the catalyst quickly restores the ATRP equilibrium.

The consistently low dispersity confirms that the FeNHC–OMe system maintains a strong activation–deactivation balance. It can rapidly incorporate newly formed chains

into the controlled regime. This interpretation is supported by the appearance of low-molecular-weight tailing in the GPC chromatograms at longer polymerization times. Such behavior is consistent with a slow and continuous reinitiation process caused by oxygen exposure. The complete kinetic data are summarized in Table 4.4, and the corresponding trends are shown in Figure 4.25.

4.3.3 Chain end functionality studies

To confirm halogen end-group retention and evaluate chain-end fidelity, a combination of ^{1}H NMR spectroscopy and chain-extension experiments was used. In the ^{1}H NMR experiment of the synthesized polystyrene (PS), a broad peak seen as resonating near at the 4.5 ppm, confirming bromine-terminated chain ends (Figure 4.26.(c)). The benzylic proton at the polymer chain end was further employed to estimate the molecular weight of the PS–Br precursor, which was found to be around 5000 Da, corresponding to roughly 50 repeating styrene units.

A chain-extension experiment was subsequently performed on PS–Br. The process employed a photochemically induced halogen atom transfer (XAT) mechanism using dimanganese decacarbonyl ($Mn_2(CO)_{10}$) as the photoinitiator. This well-established methodology generates $Mn(CO)_5$ radicals under visible light, which abstract halogen atoms from PS–Br to create reactive chain-end radicals in order to initiate further free-radical polymerization. Methyl methacrylate (MMA) served both as the monomer and solvent, leading to the formation of PS-b-PMMA block copolymers (P(S-b-MMA)). This approach was chosen because $Mn_2(CO)_{10}$-based XAT reactions are highly selective: while $Mn(CO)_5$ efficiently activates halogen-terminated chains, it does not independently initiate polymerization, and its excellent solubility in MMA ensures uniform reaction kinetics[70, 71].

For the experiment, the PS–Br prepolymer was mixed in MMA together in the presence of $Mn_2(CO)_{10}$ and irradiated under 400 nm visible light for 6 hours. The resulting block copolymer was subsequently precipitated in hexane to isolate the pure material. The GPC chromatogram of the obtained P(S-b-MMA) exhibited a distinct shift toward higher molecular weight, accompanied by an expected increase in dispersity (Đ) characteristic of a conventional free-radical process (Figure 4.26.(a)).

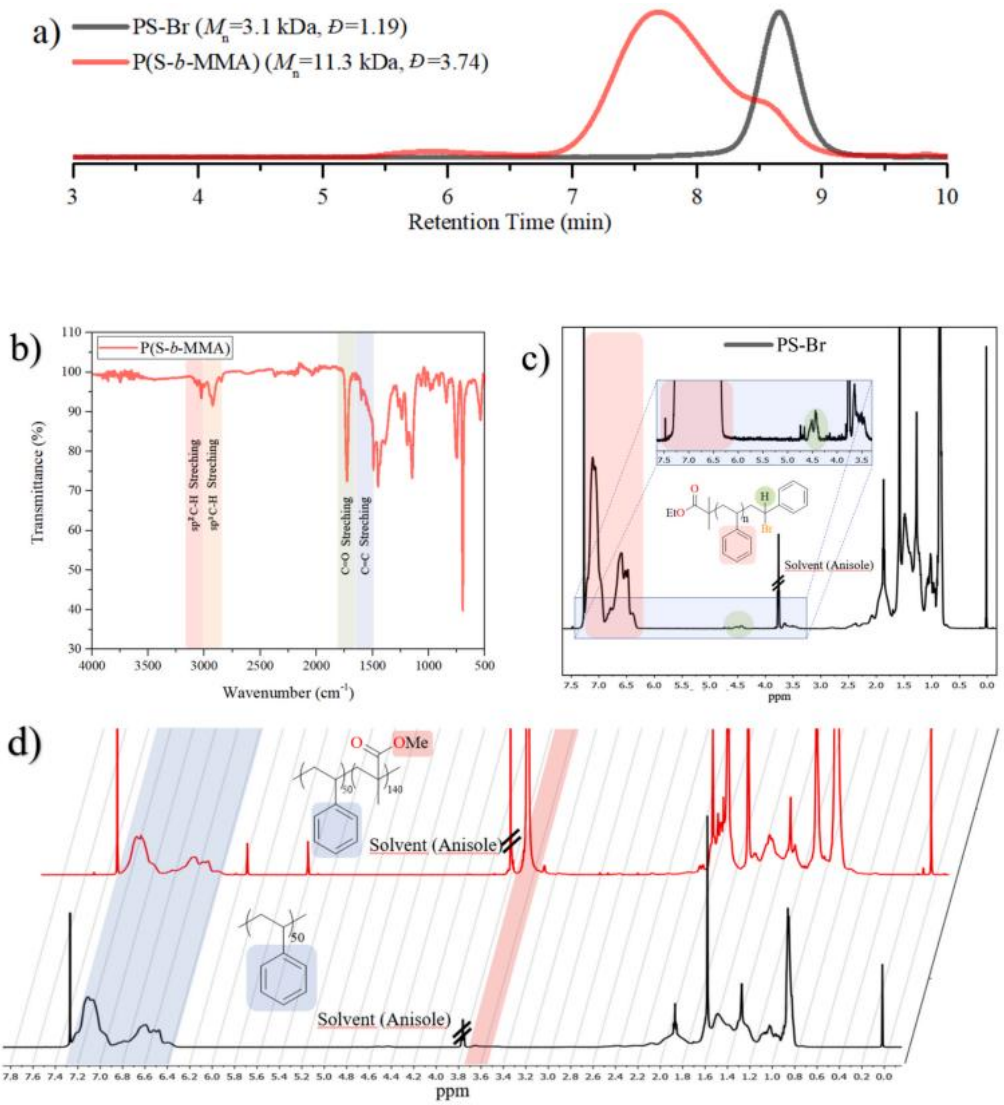

Figure 4.26 : a) Normalized GPC graphs b) FT-IR spectrum and c,d) Proton-NMR spectra of PS-Br and P(S-b-MMA) copolymer.

Gravimetric analysis of the precipitated copolymer showed an approximate 130 % increase in mass, consistent with the incorporation ratio calculated from both GPC and ^{1}H NMR measurements. Furthermore, FTIR analysis confirmed the successful incorporation of MMA units, showing characteristic absorptions for sp^3 C–H, carbonyl (C=O), alkene (C=C), and sp^2 C–H vibrations corresponding to the MMA and styrene segments (Figure 4.26. (b)). The molecular weight evolution determined from GPC and ^{1}H NMR analyses is summarized in Table 4.5.

Table 4.5 : Characteristics of the PS-Br prepolymer and P(S-b-MMA) block copolymer, analyzed by proton-NMR and GPC.

Polymer	***M*n[a] (kDa)**	***Đ*[a]**	***M*$_n$[b] (kDa)**	**Degree of Polymerization[b] (n PS: mPMMA)**
PS-Br	3.1	1.19	5	50:0
P(S-*b*-MA)	11.3	3.74	19.4	50: 140
a- Measured by GPC.				
b- Measured by proton-NMR.				

5. CONCLUSION AND RECOMMENDATIONS

In this dissertation, N-heterocyclic carbene based iron catalysts were synthesized, characterized, and comprehensively analyzed as catalysts in ICAR-ATRP systems. The intentional goal of this research was to configure environmentally compatible, low-toxicity, and highly efficient iron catalysts capable of precise control over radical polymerization. The study systematically investigated how modifications in the NHC ligand structure through changes in electronic density and steric environment affect catalytic behavior and overall polymerization performance. This approach clarified the structure–activity relationship that governs Fe–NHC catalysis.

Because the iron centers are paramagnetic, NMR experiments were carried out for the free NHC ligands. The ^{13}C NMR spectra showed characteristic carbene-carbon signals in the 220–224 ppm range, which are key indicators of ligand donor strength. Among the examined ligands, NHC–OMe exhibited the most downfield resonance at 223.8 ppm, indicating the strongest σ-donating ability toward the metal center. This trend aligns well with previously reported Cu– and Ni–NHC systems. In contrast, the upfield shifts observed for NHC–H and NHC–CN arise from geometric and N–C–N bond-angle variations that affect electron delocalization within the ligand backbone. These spectroscopic observations were further confirmed by electrochemical and computational studies.

Electrochemical characterization showed that all Fe–NHC catalysts exhibited quasi-reversible redox action, as indicated by ΔE_p values much bigger than the 59 mV known for an ideal reversible couple. This quasi-reversibility reflects moderate electron-transfer kinetics while preserving the dynamic Fe(II)/Fe(III) redox cycle required for ATRP activation–deactivation equilibrium. Among the series, FeNHC–OMe displayed the most positive anodic potential (E_{pa}), meaning that oxidation to Fe(III) is thermodynamically less favorable. As a result, it forms a stronger but less stable Fe(III) deactivator. This property enhances the deactivation of propagating radicals, producing polymers with narrow dispersity ($Đ < 1.2$). The superior performance of FeNHC–OMe compared with other complexes is attributed to its

electron-rich ligand environment and favorable redox balance, which together sustain reversible radical generation.

Density Functional Theory (DFT) calculations supported these observations. After coordination with Fe–Br, the initially planar NHC framework adopted a slightly distorted geometry. The computed complexation energies (–93.8, –91.8, –87.8, and –87.6 kcal mol^{-1} for methoxy-, hydrogen-, iodide-, and nitrile-substituted complexes, respectively) confirmed that the methoxy-substituted complex is the most thermodynamically stable. A small increase of about 0.3° in the N–C–N bond angle accompanied this stabilization, showing how electronic substitution influences both geometry and bonding. Thus, theoretical results demonstrated that the electron-donating strength of NHC ligands is the key factor governing the stability and reactivity of Fe–NHC complexes.

Polymerization experiments were performed using methyl methacrylate (MMA) and styrene as monomers. Incorporation of Fe–NHC catalysts greatly improved control compared with conventional free-radical polymerization experiment. At initial [Monomer]/[Catalyst] ratios taken from literature, GPC analysis showed clear reductions in dispersity—from 1.70 to 1.33 for PMMA and from 1.61 to 1.20 for PS. For styrene, increasing the catalyst concentration by 2.5- and 5-fold led to even tighter control, achieving $Đ < 1.20$. Since MMA polymerization proceeds faster and requires a more oxidizing catalyst to maintain equilibrium, reactions were conducted at 60 °C to slow chain growth. At higher catalyst loadings, stronger deactivation reduced the polymerization rate so that no solid polymer appeared within the first two hours. After six hours, however, well-defined polymers ($Đ \approx 1.4$) with high monomer conversion were obtained.

Kinetic studies using FeNHC–OMe showed a steady increase in number-average molecular weight (Mn) over time while maintaining low dispersity ($Đ \approx 1.15$), confirming controlled chain growth. The experimental Mn values were consistently lower than theoretical expectations, suggesting additional initiation events. This deviation was attributed to trace oxygen introduced during in-situ sampling. At 85 °C, oxygen can initiate a degenerative chain-transfer process, forming peroxyl radicals that terminate existing chains while generating new radicals capable of reinitiation. As a result, the total number of active chains increases, reducing Mn but leaving dispersity nearly unchanged. The system's ability to maintain narrow molecular-weight

distributions under these conditions highlights the robustness of the Fe–NHC-mediated ATRP equilibrium.

End-group fidelity and chain-extension ability were confirmed by ^{1}H NMR and photochemical chain-extension experiments. A broad signal near 4.5 ppm verified bromine-terminated PS chains, while integration of the benzylic proton indicated Mn ≈ 5000 Da, corresponding to about 50 styrene units. Subsequent chain extension of PS–Br with methyl methacrylate under 400 nm irradiation using $Mn_2(CO)_{10}$ as a halogen-atom-transfer photoinitiator produced PS-b-PMMA block copolymers. The GPC graphs shifted toward higher molecular weights with the expected broadening of Đ, and FTIR spectra showed carbonyl (C=O) bands from the PMMA block, confirming successful block formation. A gravimetric mass increase of roughly 130% matched well with the molecular-weight growth estimated from GPC and proton-NMR data.

Taken together, these results demonstrate that the FeNHC–OMe catalyst achieves the most effective balance between activity and control among the examined systems. Its strong σ-donating ability, favorable redox potential, and flexible geometry enable a well-regulated activation–deactivation process. This behavior ensures controlled chain propagation, preservation of end-group integrity, and consistently low dispersities. Overall, the findings emphasize that electronic tuning of NHC ligands bound to iron centers has a profound impact on ATRP performance and catalyst stability.

Given the low cost, minimal toxicity, and environmental compatibility of iron compared with copper or ruthenium systems, Fe–NHC catalysts stand out as promising candidates for next-generation sustainable ATRP processes. Future work should focus on developing functionalized or immobilized NHC ligands, exploring photo-ATRP and electrochemically mediated variants, and evaluating these systems under industrially relevant conditions to broaden their practical applicability.

In summary, this study demonstrates that precise electronic modulation through NHC ligation effectively optimizes the Fe(II)/Fe(III) redox cycle. This balance enables controlled radical polymerization with high fidelity and structural precision, marking a significant step toward eco-friendly, cost-effective, and industrially viable ATRP catalysis.

REFERENCES

[1] **Chinoporos, E.**, (1964). The Chemistry of Carbenes: Divalent Carbon. Jack Hine. Ronald, New York, 1964. vi 206 pp. *Science*, (*80*)144, 697–698.

[2] **Arduengo, AJ., Bertrand, G.,** (2009). Carbenes introduction. *Chem. Rev.*, *109*, 3209–3210

[3] **Hahn, FE.,** (2018). Introduction: Carbene Chemistry. *Chem. Rev.*, *118*, 9455–9456

[4] **Moss, R.A.,** (2017). Adventures in Reactive Intermediate Chemistry: A Perspective and Retrospective. *J Org Chem*, *82*, 2307–2318.

[5] **Hussain, Y., Empel, C., Koenigs, R.M., Chauhan, P.,** (2023). Carbene Formation or Reduction of the Diazo Functional Group? An Unexpected Solvent-Dependent Reactivity of Cyclic Diazo Imides. *Angew Chemie Int Ed* , *62*(40), e202309184.

[6] **Gerbig, D., Ley, D.,** (2013). Computational methods for contemporary carbene chemistry. Wiley Interdiscip. *Rev. Comput. Mol. Sci.*, *3*:242–272

[7] **Wanzlick, H.W., Schönherr, H.J.,** (1968). Direct Synthesis of a Mercury Salt-Carbene Complex. *Angew Chemie Int Ed English*, *7*, 141–142.

[8] **Igau, A., Grutzmacher, H., Baceiredo, A., Bertrand, G.,** (1988). Synthesis of a Stable Phosphinocarbene Phosphaacetylene. *Academic Press, 49*(1-4), 301-304.

[9] **Arduengo, A., Harlow, R. L., & Kline, M.,** (1991). a-stable-crystalline-carbene. *J Am Chem Soc, 113*, 361–363.

[10] **Arduengo, A.J.,** (1999). Looking for stable carbenes: The difficulty in starting anew. *Acc. Chem. Res.*, *32*, 913–921

[11] **Arduengo, A.J., Dixon, D.A., Kumashiro, K.K., Lee, C., et al.,** (1994). Chemical Shielding Tensor of a Carbene. *Acc. Chem. Res. 116*(14), 6361-6367.

[12] **Hirai, K., Itoh, T., Tomioka, H.,** (2009). Persistent triplet carbenes. *Chem. Rev.*, *109*, 3275–3332

[13] **Bourissou, D., Guerret, O., Gabbaï, F.P., Bertrand, G.,** (2000). Stable Carbenes. *Chem Rev.*, *100*, 39–91.

[14] **Arduengo, A.J., Goerlich, J.R., Marshall, W.J.,** (1995). A Stable Diaminocarbene, *J Am Chem Soc. 117*(44), 11027-11028.

[15] **Díez-González, S., Marion, N., Nolan, S.P.,** (2009). N-heterocyclic carbenes in late transition metal catalysis. *Chem Rev, 109*, 3612–3676.

[16] **Hahn, F.E., Jahnke, M.C.,** (2008). Heterocyclic carbenes: Synthesis and coordination chemistry. *Angew. Chemie - Int. Ed. 47*,3122–3172

[17] **Benhamou, L., Chardon, E., Lavigne, G., Bellemin, L.S.,** (2011). Synthetic routes to N-heterocyclic carbene precursors. *Chem. Rev, 111*, 2705–2733

[18] **Hopkinson, M.N., Richter, C., Schedler, M., Glorius, F.,** (2014). An overview of N-heterocyclic carbenes. *Nature, 510*, 485–496.

[19] **Nelson, D.J., Nolan, S.P.,** (2013). Quantifying and understanding the electronic properties of N-heterocyclic carbenes. *Chem Soc Rev*, *42*, 6723–6753.

[20] **Dorta, R., Scott, N.M., Costabile, C., Cavallo, L., Hoff, C.D., Nolan, S.P.,** (2005). Steric and electronic properties of N-heterocyclic carbenes (NHC): A detailed study on their interaction with $Ni(CO)_4$. *J Am Chem Soc, 127*, 2485–2495.

[21] **Huynh ,H.V.,** (2018). Electronic Properties of N-Heterocyclic Carbenes and Their Experimental Determination. *Chem Rev, 118*, 9457–9492.

[22] **Glorius, F., Bellemin, S.,** (2007). 21 Topics in Organometallic Chemistry. *Acedemic Press*

[23] **Bharti, R., Verma, M., Thakur, A., Sharma, R.,** (2022). N-Heterocyclic Carbenes (NHCs): An Introduction In Carbene. *IntechOpen*

[24] **Leow, M.Y., Ho, C.C., Gardiner, M.G., Bissember, A.C.,** (2018). Non-classical anionic naked n-heterocyclic carbenes: Fundamental properties and emerging applications in synthesis and catalysis. *Catalysts, 8*(12), 620.

[25] **Hopkinson, M.N., Glorius, F.,** (2019). An Overview of NHCs, *N-Heterocyclic Carbenes in Organocatalysis*, 1-35.

[26] **Jazzar, R., Soleilhavoup, M., Bertrand, G.,** (2020). Cyclic (Alkyl)- And (Aryl)-(amino)carbene Coinage Metal Complexes and Their Applications. *Chem. Rev., 120*,4141–4168

[27] **Crudden, C.M., Allen, D.P.,** (2004). Stability and reactivity of N-heterocyclic carbene complexes. *Coord. Chem. Rev. 248*, 2247–2273

[28] **Liang, Q., Song, D.,** (2020). Iron N-heterocyclic carbene complexes in homogeneous catalysis. *Chem. Soc. Rev. 49*,1209–1232

[29] **Riener, K., Haslinger, S., Raba, A., Högerl, M.P., Cokoja, M., Herrmann, W.A., Kühn, F.E.,** (2014). Chemistry of Iron N -heterocyclic carbene complexes: Syntheses, structures, reactivities, and catalytic applications. *Chem. Rev. 114*,5215–5272

[30] **Ingleson, M.J., Layfield, R.A.,** (2012). N-Heterocyclic carbene chemistry of iron: Fundamentals and applications. *Chem Commun, 48*, 3579–3589.

[31] **Nathajha, B., Singh, N., Raghuvanshi, A.,** (2020). Catalytic Activity of Iron N-Heterocyclic Carbene Complexes in Organic Synthesis. *IntechOpen*

[32] **Louie, J., Grubbs, R.H.,** (2000). Highly active iron imidazolylidene catalysts for atom transfer radical polymerization. *Chem Commun*, *85*, 1479–1480.

[33] **Yıldırım, M.S., Gencosman, E., Bozan, G., Gu, J., Elliott, G.I., Grotjahn, D., Kiliclar, H.C., Unlu, C.H.**, (2025). Synthesis of N-Heterocyclic carbene complexes with different substituents to tune the electron density of iron center and their catalytic performance in ICAR-ATRP. *Eur Polym J*, 238, 114233

[34] **Dadashi, S.S., Matyjaszewski, K.,** (2020). Iron catalysts in atom transfer radical polymerization. *Molecules, 25*(7), 1648.

[35] **Donner, A., Trepka, B., Theiss, S., Immler, F., Traber, J., Polarz, S.,** (2019). NHC-Metallosurfactants as Active Polymerization Catalysts. *Langmuir*, *35*, 16514–16520.

[36] **Liu, Y., Harlang, T., Canton, S.E., et al.** (2013). Towards longer-lived metal-to-ligand charge transfer states of iron(II) complexes: An N-heterocyclic carbene approach. *Chem Commun, 49*, 6412–6414.

[37] **Xue, Z., He, D., Xie, X.,** (2015). Iron-catalyzed atom transfer radical polymerization. *Polym Chem*, *6*, 1660–1687.

[38] **Corrigan, N., Jung, K., Moad, G., Hawker, C.J., Matyjaszewski, K., Boyer, C.,** (2020). Reversible-deactivation radical polymerization Controlled/living radical polymerization: From discovery to materials design and applications. *Prog. Polym. Sci.*, 111

[39] **Zetterlund, P.B., Kagawa, Y., Okubo, M.,** (2008). Controlled/living radical polymerization in dispersed systems. *Chem. Rev., 108*, 3747–3794

[40] **Otsu, T.,** (2000). Iniferter concept and living radical polymerization. *J Polym Sci Part A Polym Chem, 38*, 2121–2136

[41] **Wang, J.S., Matyjaszewski, K.,** (1995). Controlled/" living" radical polymerization. atom transfer radical polymerization in the presence of transition-metal complexes. *Journal of the American Chemical Society*, 117(20), 5614-5615.

[42] **Truong, N.P., Jones, G.R., Bradford, K.G.E., Konkolewicz, D., Anastasaki, A.,** (2021). A comparison of RAFT and ATRP methods for controlled radical polymerization. *Nat. Rev. Chem.*, *5*, 859–869

[43] **Bradford, K., Petit, L.M.,** (2021). Ubiquitous Nature of Rate Retardation in Reversible Addition–Fragmentation Chain Transfer Polymerization. *Journal of the American Chemical Society*, *143*, (42), 17769-17777.

[44] **Mastan, E., Li, X., Zhu, S.,** (2015). Modeling and theoretical development in controlled radical polymerization. *Prog Polym Sci*, *45*, 71–101.

[45] **Matyjaszewski, K.,** (2012). Atom Transfer Radical Polymerization (ATRP): Current Status and Future Perspectives. *Macromolecules*, *45*, 4015-4039.

[46] **Fang, C., Fantin, M., Pan, X., De Fiebre, K., Coote, M.L., Matyjaszewski, K., Liu, P.,** (2019). Mechanistically Guided Predictive Models for Ligand and Initiator Effects in Copper-Catalyzed Atom Transfer Radical Polymerization (Cu-ATRP). *J Am Chem Soc*, *141*, 7486–7497.

[47] **Kütahya, C., Schmitz, C., Strehmel, V., Yagci, Y., Strehmel, B.,** (2018). Near-Infrared Sensitized Photoinduced Atom-Transfer Radical Polymerization (ATRP) with a Copper(II) Catalyst Concentration in the ppm Range. *Angew Chemie Int Ed*, *57*, 7898–7902.

[48] **Matyjaszewski, K., Tsarevsky, N.V.,** (2014). Macromolecular engineering by atom transfer radical polymerization. *J. Am. Chem. Soc.*, *136*, 6513–6533

[49] **Coessens, V.M.C., Matyjaszewski, K.,** (2010). Fundamentals of atom transfer radical polymerization. *J Chem Educ*, *87*, 916–919.

[50] **Zhang, Y., Li, M., Li, B., Sheng, W.,** (2024). Surface Functionalization with Polymer Brushes via Surface-Initiated Atom Transfer Radical Polymerization: Synthesis, Applications, and Current Challenges. *Langmuir*, *40*, 5571–5589

[51] **Dworakowska, S., Lorandi, F., Gorczyński, A., Matyjaszewski, K.,** (2022). Toward Green Atom Transfer Radical Polymerization: Current Status and Future Challenges. *Adv. Sci.*, *9*(19), 2106076.

[52] **Ran, J., Wu, L., Zhang, Z., & Xu, T.** (2014). Atom transfer radical polymerization (ATRP): A versatile and forceful tool for functional membranes. *Progress in Polymer Science*, *39*(1), 124-144.

[53] **Wu, J., Jiang, X., Zhang, L., Cheng, Z., & Zhu, X.** (2016). Iron-mediated homogeneous ICAR ATRP of methyl methacrylate under ppm level organometallic catalyst iron (III) acetylacetonate. *Polymers*, *8*(2), 29.

[54] **Yuan, M., Cui, X., Zhu, W., Tang, H.,** (2020). Development of environmentally friendly atom transfer radical polymerization. *Polymers*, *12*, 1–32

[55] **Zhu, G., Zhang, L., Zhang, Z., Zhu, J., Tu, Y., Cheng, Z., Zhu, X.,** (2011). Iron-mediated ICAR ATRP of methyl methacrylate. *Macromolecules*, *44*, 3233–3239.

[56] **Faria, G.C.L., Lyra, E.P.,** (2022). Exploring solution ICAR ATRP of methyl acrylate with AIBN as azo initiator: a kinetic modeling and simulation study. *Results in Materials*, *15*, 100313.

[57] **Ribelli, T.G., Lorandi, F., Fantin, M., Matyjaszewski, K.,** (2019). Atom Transfer Radical Polymerization: Billion Times More Active Catalysts and New Initiation Systems. *Macromol. Rapid Commun*., *40*(1), 1800616.

[58] **Pan, X., Fantin, M., Yuan, F., Matyjaszewski, K.,** (2018). Externally controlled atom transfer radical polymerization. *Chem Soc Rev*, *47*, 5457–5490.

[59] **Szewczyk, M., Plichta, A., Dębowski, M., Kowalczyk, S., Iuliano, A., Florjańczyk, Z.,** (2023). Recent Advances in the Application of ATRP in the Synthesis of Drug Delivery Systems. *Polymers*,15

[60] **Di Lena, F., Matyjaszewski, K.,** (2010). Transition metal catalysts for controlled radical polymerization. *Prog Polym Sci*, *35*, 959–1021.

[61] **Louie, J., Grubbs, R.H.,** (2000). Highly active iron imidazolylidene catalysts for atom transfer radical polymerization. *Chem Commun*,1479–1480.

[62] **Okada, S., Park, S., Matyjaszewski, K.,** (2014). Initiators for continuous activator regeneration atom transfer radical polymerization of methyl methacrylate and styrene with N-heterocyclic carbene as ligands for Fe-based catalysts. *ACS Macro Lett*, 3, 944–947.

[63] **Kim, S., Kim, C., Chung, H.,** (2022). N-heterocyclic Carbene Containing Homogeneous Ru Catalyst for Aqueous Atom Transfer Radical Polymerization of Water-soluble Vinyl Monomers. *Polymer*, 241.

[64] **Idehara, A.H.S., Gois, P.D.S., Fernandez, H.,** (2018). Accessible ring opening metathesis and atom transfer radical polymerization catalysts based on dimethyl sulfoxide ruthenium(II) complexes bearing N-heterocyclic carbene ligands. *Mol Catal*, 448, 135–143.

[65] **Huynh, H.V., Han, Y., Jothibasu, R., Yang, J.A.,** (2009). ^{13}C NMR spectroscopic determination of ligand donor strengths using N-Heterocyclic carbene complexes of palladium(II). *Organometallics*, 28, 5395–5404.

[66] **Elgrishi, N., Rountree, K.J., McCarthy, B.D., Rountree, E.S., Eisenhart, T.T., Dempsey, J.L.,** (2018). A Practical Beginner's Guide to Cyclic

Voltammetry. *J Chem Educ*, 95, 197–206.

[67] **Qiu, J., Matyjaszewski, K., Thouin, L., Amatore, C., (**2000). Cyclic voltammetric studies of copper complexes catalyzing atom transfer radical polymerization. *Macromolecular Chemistry and Physics*, 201(14), 1625-1631.

[68] **Okada, S., Park, S., Matyjaszewski, K.,** (2014). Initiators for continuous activator regeneration atom transfer radical polymerization of methyl methacrylate and styrene with N-heterocyclic carbene as ligands for Fe-based catalysts. *ACS Macro Lett*, 3, 944–947.

[69] **Mukumoto, K., Wang, Y., Matyjaszewski, K.,** (2012). Iron-based ICAR ATRP of styrene with ppm amounts of FeIIIBr 3 and 1,1′-azobis (cyclohexanecarbonitrile). *ACS Macro Lett*, 1, 599–602.

[70] **Kiliclar, H.C., Altinkok, C., Yilmaz, G., Yagci, Y.,** (2021). Visible light induced step-growth polymerization by electrophilic aromatic substitution reactions. *Chem Commun*, 57, 5398–5401.

[71] **Bamford, C.H., Denyer, R.,** (1968). Initiation of free radical polymerization by manganese carbonyl and carbon tetrachloride. *Nature*, 217, 59–60.

CURRICULUM VITAE

Name Surname **:** Mustafa Semih Yıldırım

EDUCATION **:**

- **B.Sc.** **:** 2018, Istanbul Technical University, Science and Literature Faculty, Chemistry Department
- **M.Sc.** **:** 2020, Istanbul Technical University, Science and Literature Faculty, Chemistry Department

PROFESSIONAL EXPERIENCE AND REWARDS:

- Research Assistant at Istanbul Technical University – Chemistry Department 2019-2022
- Visiting Researcher- San Diego State University- Chemistry Department 2022-2024

PUBLICATIONS, PRESENTATIONS AND PATENTS ON THE THESIS:

- **Yıldırım, M. S.,** Gencosman, E., Bozan, G., Gu, J., Elliott, G. I., Grotjahn, D., & Unlu, C. H. (2025). Synthesis of N-Heterocyclic carbene complexes with different substituents to tune the electron density of iron center and their catalytic performance in ICAR-ATRP. *European Polymer Journal*, 114233.

- **Yildirim, M. S.,** Kiliclar, H. C., Gencosman, E., & Unlu, C. H. Development of iron based organometallic complexes for atom transfer radical polymerization. 12th Selçuk International Conference on Applied Sciences., May 23–25, 2025.ISBN:978-625-5962-73-7.

OTHER PUBLICATIONS, PRESENTATIONS AND PATENTS:

- **Kaplan M., Yavuz, O., Çetin D., Alcay, Y., Yildirim, M.S., Aribuga, H., Ozdemir, E., Ertugral, U., Yilmaz, I.** 2022. Cu^{2+} İyonunun Sulu Ortamda Seçici ve Hassas Tayini İçin Naftakinon Tabanlı Yeni Bir Kimyasal Probun Geliştirilmesi. 5th International Eurasian Conference on Biological and Chemical Sciences (EurasianBioChem 2022) November 23-25, 2022.
- Breloy, L., Brezová, V., Blacha-Grzechnik, A., Presset, M., **Yildirim, M. S.,** Yilmaz, I., & Versace, D. L. (2019). Visible light anthraquinone functional

phthalocyanine photoinitiator for free-radical and cationic polymerizations. *Macromolecules*, 53(1), 112-124.

- Alcay, Y., Ozdemir, E., **Yildirim, M. S.,** Ertugral, U., Yavuz, O., Aribuga, H., & Yilmaz, I. (2023). A methionine biomolecule-modified chromenylium-cyanine fluorescent probe for the analysis of Hg2+ in the environment and living cells. *Talanta*, 259, 124471.
- Aribuga, H., Ertugral, U., Alcay, Y., Yavuz, O., **Yildirim, M. S.,** Ozdemir, E., & Yilmaz, I. (2023). A new Fe3+-selective, sensitive, and dual-channel turn-on probe based on rhodamine carrying thiophenecarboxaldehyde: Smartphone application and imaging in living cells. *Spectrochimica Acta Part A: Molecular and Biomolecular Spectroscopy*, 287, 122060.
- Cetin, D., Yavuz, O., Alcay, Y., **Yildirim, M. S.,** Kaplan, M., Aribuga, H., & Yilmaz, I. (2023). Development of a new near-infrared, spectrophotometric, and colorimetric probe based on phthalocyanine containing mercaptoquinoline unit for discriminative and highly sensitive detection of Ag+, Cu2+, and Hg2+ ions. *Spectrochimica Acta Part A: Molecular and Biomolecular Spectroscopy*, 297, 122725.
- Ozdemir, E., Alcay, Y., Yavuz, O., **Yildirim, M. S.,** Aribuga, H., Ertugral, U., & Yilmaz, I. (2023). Colorimetric and near-infrared spectrophotometric monitoring of bisulfite using glyoxal modified chromenylium-cyanine chemosensor: Smartphone and paper strip applications for on-site food and beverages control. *Talanta*, 261, 124660.
- **Yildirim, M. S.,** Alcay, Y., Ozdemir, E., Ertugral, U., Yavuz, O., Aribuga, H., & Yilmaz, I. (2024). Molecular architecture of a novel indoline-fused chromenylium-cyanine probe carrying methionine biomolecule for ultrasensitive analyzing Hg2+ ion in real samples. *Journal of Environmental Chemical Engineering*, 12(6), 114388.
- Yavuz, O., Alcay, Y., Kaya, K., Sezen, M., Kirlangic Atasen, S., **Yildirim, M. S.,** & Yilmaz, I. (2018). Superior sensor for Be2+ ion recognition via the unprecedented octahedral crystal structure of a one-dimensional coordination polymer of crown fused zinc phthalocyanine. *Inorganic Chemistry*, 58(1), 909-923.
- Yavuz, O., Sezen, M., Alcay, Y., **Yildirim, M. S.,** Kaya, K., Ozkilic, Y., & Yilmaz, I. (2021). A new perspective on the beryllium sensor platform: Low symmetry phthalocyanine-based molecular design and ultra trace amount Be2+ ion recognition in aqueous media. *Sensors and Actuators B: Chemical*, 329, 129002.
- **Yildirim, M. S.,** Alcay, Y., Yavuz, O., Atasen, S. K., Mermer, Z., Aribuga, H., & Yilmaz, I. (2022). Construction of anthraquinone functional zinc phthalocyanine sensor platform for ultra-trace amount of water determination in tetrahydrofuran and N, N-Dimethylformamide. *Analytica Chimica Acta*, 1198, 339531.
- Yavuz, O., Sezen, M., Alcay, Y., **Yildirim, M. S.,** Aribuga, H., Ozdemir, E., & Yilmaz, I. (2023). A new highly Selective, sensitive and NIR spectrophotometric probe based on A2B2-Type of unsymmetrical phthalocyanine for hazardous Be2+ recognition. *Spectrochimica Acta Part A: Molecular and Biomolecular Spectroscopy*, 284, 121484.